FACULTY OF ELECTRICAL ENGINEERING
UNIVERSITY OF BANJA LUKA

ELECTRONICS

VOLUME 24, NUMBER 1, JUNE 2020

FACULTY OF ELECTRICAL ENGINEERING
UNIVERSITY OF BANJA LUKA

Address: Patre 5, 78000 Banja Luka, Bosnia and Herzegovina
Phone: +387 51 211824
Fax: +387 51 211408
Web: www.etf.unibl.org

E L E C T R O N I C S

Web: www.els-journal.etf.unibl.org
E-mail: els-journal@etf.unibl.org

Publisher:
Faculty of Electrical Engineering, University of Banja Luka, Bosnia and Herzegovina

Number of printed copies: 100

Editor's Column

Mladen Knezic

> Life is like a pen. It's getting shorter every day. Make sure you draw something nice while it's still there.
>
> *Nebojša Glogovac*

Editorial Letter
DOI: 10.7251/ELS2024001K

THE first issue of *Electronics* journal in June 2020 brings one review paper, which covers the application of swarm optimization algorithms in the field of photovoltaic systems control, and four regular papers reporting original research results in the field of analog and digital electronics, image processing, and electronics materials and technologies.

The first paper "A Comprehensive Review of Swarm Optimization Algorithms for MPPT Control of PV Systems under Partially Shaded Conditions," authored by D. Pilakkat, S. Kanthalakshmi, and S. Navaneethan, is a review paper that provides a survey on different Swarm Intelligence (SI) based maximum power point tracking (MPPT) algorithms for photovoltaic (PV) systems. As pointed out by the authors, the described algorithms are suitable for operation under partially shaded conditions.

The paper "Revisiting Analytical Models of N-Type Symmetric Double-Gate MOSFETs," by R. U. Ahmed and P. Saha, presents analytical models of n-type symmetric double-gate MOSFETs based on analyses of electrostatic potential distribution. The authors provided mathematical derivations of the device models and carried out numerical simulations to validate their repeatability.

The paper "On the Implementation of Multi-Bit Inexact Adder Cells and Application Towards Image De-Noising," by S. K. Beura, A. A. Jawale, B. P. Devi, and P. Saha proposes 2-bit inexact adder cell and its extension to 4-bit and 8-bit adder variants. The cell has been evaluated mathematically in terms of error metrics and verified through the Cadence Spectre with special focus on performance parameters such as delay and power consumption. Moreover, the authors applied proposed design to image de-noising application, where different image processing metrics (namely, Peak Signal to Noise Ratio, Normalized Correlation Coefficient and Structural Similarity Index) has been analyzed through MATLAB simulations.

The paper "Characteristics of $Zn_{1-x}Al_xO$ NR/ITO Composite Films Oriented Application for Optoelectronic Devices," authored by N. D. Lam, focuses a hydrothermal method for growing wurtzite type $Zn_{1-x}Al_xO$ NR structures on ITO substrate producing $Zn_{1-x}Al_xO$ NR/ITO composite film. The paper investigates influences of the Al doping concentration on surface morphology, structural and optical characteristics of the $Zn_{1-x}Al_xO$ NR/ITO composite film. Moreover, the author evaluates electrical property of the $Zn_{1-x}Al_xO$ NR/ITO composite film in order to find out optimized conditions for application in optoelectronic devices fabrication.

The paper "A Novel Dual Output Schmitt Trigger Using Second Generation Current Controlled Conveyor," by A. Srinivasulu, S. Zahiruddin, and M. Sarada, describes a novel configuration of the Schmitt trigger using a topology with the single second generation Current Controlled Conveyor (CCCII) and only two externally connected resistors. The proposed configuration is tested experimentally using current-feedback operational amplifier (CFOA) and operational transconductance amplifier (OTA) integrated circuits.

I thank the authors for their contribution to this issue of the journal and to all the reviewers who participated in the editorial process by providing valuable comments in timely manner to the editors and the authors.

A Comprehensive Review of Swarm Optimization Algorithms for MPPT Control of PV Systems under Partially Shaded Conditions

Deepthi Pilakkat, S. Kanthalakshmi, S. Navaneethan

***Abstract*—Nowadays many researchers have been investigating on different photovoltaic (PV) modeling methods, various configurations of arrays, numerous algorithms, converter topologies etc to improve the efficiency of solar system. Improving the efficiency of solar panel by utilizing the correct maximum power point tracking (MPPT) control has become more important for conceiving the solar power reasonably. For designing an efficient PV system, an appropriate literature review is necessary for all the researchers. In this paper, a compendious study of different Swarm Intelligence (SI) based MPPT algorithms for PV systems feasible under partially shaded conditions are presented. SI algorithms use motivation from the foraging nature of animals and insects. In the last few decades, SI has gained tremendous attention as it has been proven as an efficient control technique for global optimization problems.**

***Index Terms*—Bio-Inspired optimization algorithms, Maximum Power point tracking (MPPT), Solar PV systems, Swarm Intelligence (SI) algorithms.**

Review Paper
DOI: 10.7251/ELS2024003P

I. Introduction

DUE to the cost reduction and governmental aids, the PV technology has grown rapidly in each year at a rate of 30% [1]. About 1.8*1011 MW power from sun is intercepted by the earth which is ever greater than any other form of energy consumption [2]. Due to the partial shading on the PV panel the efficiency of the system will decrease, increase the cost and complexity [3]. Since the efficiency of the photovoltaic (PV) panel is approximately 20 % -30 %, the maximum power point tracking (MPPT) controllers in PV systems are very important. The performance of the PV system can be enhanced in combination with MPPT by means of electronic power controllers [4].

Manuscript received 14 June 2019. Received in revised form 23 January 2020 and 12 February 2020. Accepted for publication 18 February 2020.

Deepthi Pilakkat is with Department of Electrical and Electronics Engineering, PSG college of Technology, 641004, India (e-mail:deepthipilakkat@gmail.com, phone: +91-8075705353).

S. Kanthalakshmi is with Department of Electrical and Electronics Engineering, PSG college of Technology, 641004, India (e-mail: skl.eee@psgtech.ac.in)

S. Navaneethan is with Department of Instrumentation and Control Systems Engineering, PSG college of Technology, 641004, India (e-mail: snn.ice@psgtech.ac.in)

The efficiency of a PV system can be substantially increased beyond 95% by bringing the highest possible power out of a PV module. Numerous algorithms have been developed to track the maximum power point effectively. Most of the current MPPT algorithms vary in tracking speed, implementation expense, number of sensors used, implementation of hardware, ability to track true MPP during partial shading conditions (PSC) and other aspects. All the MPPT algorithms are essentially categorized under any of the two following: conventional and non-conventional MPPT algorithms.

The conventional MPPT techniques such as Perturb and Observe (P&O) [5]-[6], Incremental conductance (INC) [7]-[8], Fractional Open Circuit Voltage (FOV) [9], Short-Circuit Current Control (SCCC) [10] are the most widely used techniques due to its simplicity and ease of implementation. Other types of MPPT algorithms, including Artificial Intelligence (AI) [11], Fuzzy Logic (FL) [12]-[13], and Bio-Inspired (BI) [14] algorithms are also available in literature, which fall under the category of non-conventional MPPT algorithms. Biologically inspired algorithms have been used in recent years as the key techniques to get the best solutions to real engineering design optimization problems. They always offer an optimal solution for optimization problems while maintaining a perfect balance between the components. Most researchers have paid more attention to this field in the last few decades. The two most predominant and successful classes in bio-inspired algorithms are evolutionary algorithms and swarm intelligence based algorithms. These algorithms are derived from the study of the natural evolution of living things and their swarming behavior. Fig.1 shows the general classification of different MPPT algorithms used in for photovoltaic applications. Nature-inspired optimization algorithms are developed as powerful tools to solve the complicated problems. SI is a fairly new interdisciplinary research field, which has become popular these days [15]. It is possible to adapt and apply the characteristics and lifestyles of birds, animals and other living organisms to solve many real world problems. SI-based optimization algorithms have been developed to model animals' intelligent behavior. In these modeling systems, by sharing information, a group of organisms such as ants, bees, birds and fish communicate with each other and with their environment, resulting in the use of their environment and resources. Many SI based algorithms such as Artificial Bee Colony algorithms (ABC)[16], Particle Swarm Optimization (PSO) [17], Bat Algorithm (BA) [18]

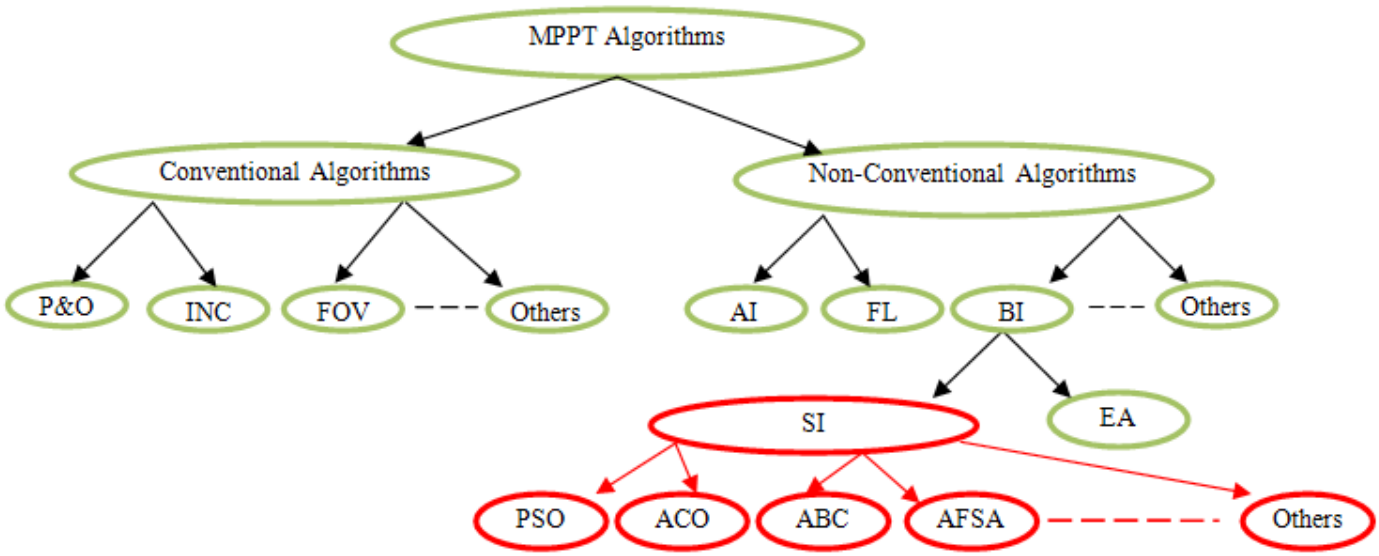

Fig. 1. Classification of MPPT algorithms used in PV system

etc. have been used for many real world optimization applications including MPPT tracking. Nevertheless, some difficulty remains, and new algorithms are still required for better optimization. While new algorithms, including chicken swarm optimization (CSO) [19], Krill herd algorithm (KHA) [20], Grey Wolf Optimization (GWO) [21] etc., are still imminent, the development of a better algorithm from nature's knowledge is an interesting research subject. This paper reviews the implementation of various MPPT algorithms (particularly on SI), which are influenced by nature and are used in partial shading conditions (PSC) for solar PV systems.

II. PV Systems Under Partial Shading Condition

A PV panel is the basic building block of a photovoltaic generation system (PGS). The PV panels consist of a large number of series or parallel solar cells to provide the necessary voltage and current. The change in temperature or irradiance will directly affect the output of PGS. When partial shading occurs, there exhibits multiple number of power peaks in power-voltage (P-V) curve. For better understanding of shading effects, Fig.2(a) shows a PV array with four modules connected in series (with bypass diodes connected in parallel with each module

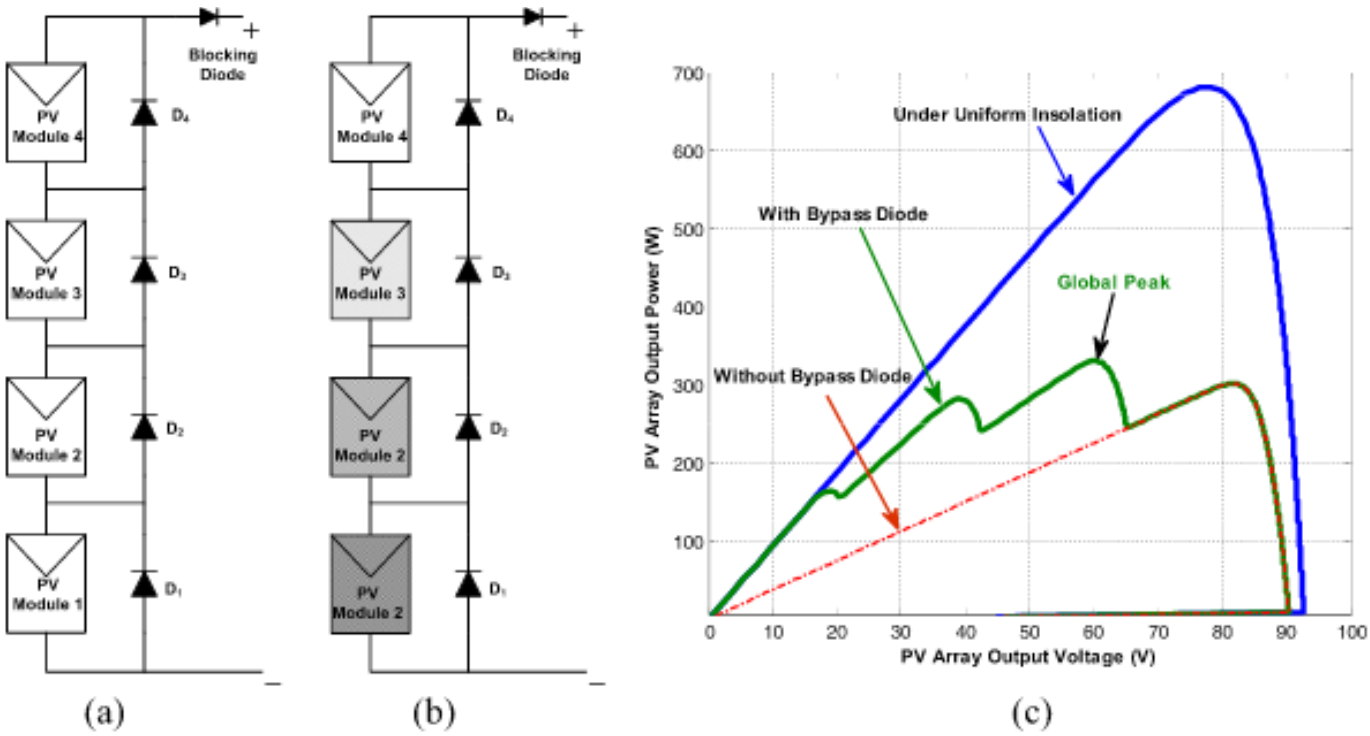

Fig. 2. Operation of solar PV array (a) under uniform insolation, (b) under shading condition, and (c) corresponding P-V curve [22]

and one blocking diode connected in series in the string) under uniform insolation condition. In Fig. 2(b) the PV modules are undergoing PSC and the corresponding P-V characteristics are shown in Fig. 2(c) with multiple power point (MPP) [22]. These complex P-V features would confuse local MPP (LMPP) monitoring, rather than global MPP (GMPP).To track GMPP, a global optimization algorithm is required, so that maximum power can be extracted from the PV panel.

III. Modeling Of A Pv System Under Partial Shading Conditions

The general mathematical model in equation (1) gives the output power from a PV panel.

$$I_{PV} = N_P.I_{ph} - N_P.I_S\left[exp\left\{\frac{q\left(V_{PV}+I_{PV}R_s\right)}{N_S.A.k.T_{op}}\right\} - 1\right] \tag{1}$$

where, N_P and N_s represents parallel and series connected cells. I_{ph} denotes the photo current of the module, I_s represents saturation current, q is electron charge, k is Boltzman constant, A is ideality factor and T_{op} is module operating temperature in Kelvin. The equation (1) is no longer applicable in the case of PSC because dissimilar levels of irradiance are dispersed between the PV arrays as shown in figure number 2 (Fig. 2). The characterization of PV systems under PSC therefore requires a new mathematical model. Alajmi et al. undertook a comprehensive study in 2013 on various irradiation conditions for various PV module connections [23]. The authors derived a general numerical model for n series connected PV modules under partial shading conditions which is given in equation:

$$V_{PV} = \begin{cases} \sum \frac{AKTn_s^{us}}{q}\ln\left(\frac{I_{sc}\lambda^{un}-I_{PV}}{I_o}\right), & I_{PV} > I_{Nstep} \\ \vdots & \vdots \\ \sum \frac{AKTn_s^{us}}{q}\ln\left(\frac{I_{sc}\lambda^{un}-I_{PV}}{I_o}\right)+\frac{AKTn_s^{us1}}{q}\ln\left(\frac{I_{sc}\lambda^{s}-I_{PV}}{I_o}\right), & I_{1step} < I_{PV} < I_{2step} \\ \sum \frac{AKTn_s^{us}}{q}\ln\left(\frac{I_{sc}\lambda-I_{PV}}{I_o}\right)+\frac{AKTn_s^{s1}}{q}\ln\left(\frac{I_{sc}\lambda^{s1}-I_{PV}}{I_o}\right)+\ldots+\frac{AKTn_s^{sN}}{q}\ln\left(\frac{I_{sc}\lambda^{sN}-I_{PV}}{I_o}\right), & I_{PV} < I_{1step} \end{cases} \tag{2}$$

where n_s^{us} is the number of unshaded PV modules and λ^{un} is the unshaded radiation. n_s^{sN} is the number of partially shaded PV modules with the highest radiation level and λ^{sN} is the highest radiation level. N is the number of distributed radiation levels. I_{sc} is the short-circuit current of the unshaded PV modules. I_{1step} is the short-circuit current of the shaded PV module. I_{2step} is the short-circuit current of the shaded PV modules with the highest radiation level.

IV. Swarm Intelligence Based MPPT Algorithm for PV Systems

The following sections address various SI-based MPPT optimization algorithms used in PV systems.

A. Particle Swarm Optimization Algorithm (PSO)

It is an optimization algorithm based on swarm intelligence developed by Eberhart and Kennedy in 1995 [24]. This algorithm is inspired from the swarm behavior of social animals like fishes and birds. In this, a large number of particles (agents) travel around in the search space in search for the best solution. Each particle in the problem space represents a potential solution vector P_i (Position). These particles adjust its velocity according to its own flying experience and experience of its companions. The velocity of each particle is represented by a velocity vector V_i. A fitness function *'f'* shall be calculated using P_i as a quality measurement input. Each particle retains the best fitness it has achieved so far and sets it to P_{best} as its individual best position. In addition, the best solution is taken as G_{best} between all particles that have been achieved so far in the swarm. All of this information is made available for all particles to converge to the best global solution [25].

For finding an optimal solution for a problem, PSO adjusts the personal best position (P_{best}) and global best position (G_{best}) using the following equations:

$$V_{i(j+1)} = wV_{i(j)} + C_1r_1\left(P_{best} - P_{i(j)}\right) + C_2r_2\left(G_{best} - P_{i(j)}\right) \tag{3}$$

$$P_{i(j+1)} = P_{i(j)} + V_{i(j+1)} \tag{4}$$

where P_i presents the position of particle and is the velocity, ω is the inertia weight which is used to represent the impact of previous particle velocity on its current one. r_1 and r_2 are random variables uniformly distributed within [0, 1]. C_1 and C_2 are the coefficients of acceleration. The flowchart of conventional particle swarm optimization is shown in Fig. 3.

PSO has been widely extended for various applications such as complex and multi-dimensional optimization problems. The major advantages of PSO includes simple computation, reliable and robust, guaranteed global convergence, and simple application with less expensive controller. Recently, PSO algorithm has been considered as one of the promising algorithm for solution of global optimization problems.

i. Application of PSO in MPPT

Miyatake et al. revised the standard PSO approach in 2007 to be extended to regulate the MPPT [26] . The fitness function *f* often changes with regard to atmospheric or electric load variations in real-time applications. The algorithm must be restarted to track the real MPP in these instances. The particles are reinitialized if the above conditions change and the following two equations are used to identify them:

$$|v_{i+1}| < \Delta v \tag{5}$$

where v_{i+1} represents the velocity of the next particle and Δv represents change in velocity, and:

$$\frac{P_{i+1} - P_i}{P_i} < -\Delta P \tag{6}$$

where P_i is the power output of the solar panel.

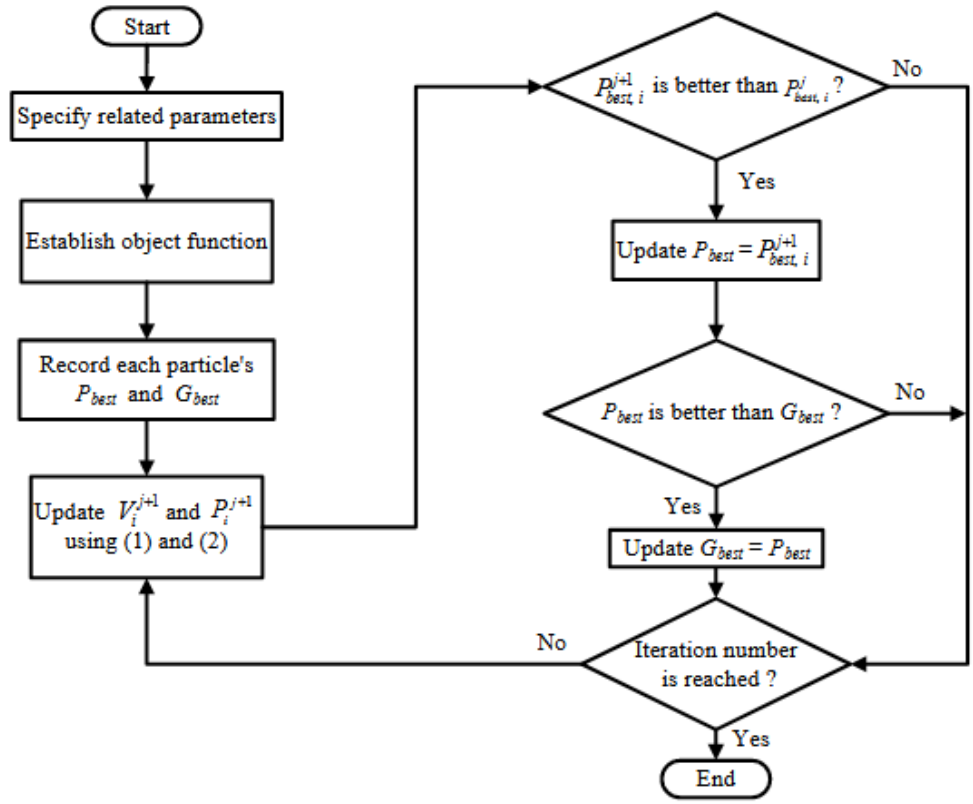

Fig. 3. Flowchart of conventional PSO algorithm [26]

The equations (5) and (6) correspond to agent's convergence detection and sudden change of insolation, respectively.

For practical application of PSO for MPPT controllers in PV system, the position of particle, P_i is considered as the duty cycle d_i. Thus, the velocity, acts as a perturbation in the current duty cycle and the equation changed as shown below.

$$d_{i(j+1)} = d_{i(j)} + V_{i(j+1)} \tag{7}$$

To reduce the difficulty in finding MPP, Phimmasone *et al.* in 2009 [27] modified the conventional PSO technique by adding a repulsive term to the PSO equation. This modification simplifies the PSO and enhances their response to monitor the MPP under different atmospheric conditions. It leads to greater productivity and lower costs. The enhanced PSO-MPPT algorithm by means of overall energy production is superior to traditional PSO-MPPT methods.

In 2012, Ishaque and Salam, successfully modified the conventional PSO algorithm by eliminating the random variables and introduced a new Deterministic PSO (DPSO) algorithm [28]. Moreover, only one parameter needs to be tuned in the proposed method; which is the inertia weight. For implementing the DPSO algorithm they used TMS320F240 DSP on the Dspace DS1104. The authors claim that the proposed method has good accuracy and better speed compared to the conventional hill climbing method.

In the same year, Liu *et al.* proposed a modified PSO algorithm for PV generation systems under partial shading conditions [29]. In conventional PSO method equation (3) and (4) are used to update the particle, in which w, C1 and C2 are constants. In this paper, authors modified these constants as variables and updated equation (3) as shown below.

$$V_{i(j+1)} = w_j V_{i(j)} + C_{1(j)} r_1 \left(P_{best} - P_{i(j)}\right) + C_{2(j)} r_2 \left(G_{best} - P_{i(j)}\right) \tag{8}$$

To speed up the convergence the inertia weight, ω is set as maximum in the initial condition and is linearly decreased using equation (9):

$$w_j = w_{max} - \frac{k}{k_{max}}\left(w_{max} - w_{min}\right) \tag{9}$$

where, w_{max} and w_{min} are the maximum and minimum values of w, and k_{max} is the maximum allowed number of iterations.

The direction of particles will also be biased by modifying $C_1$and C_2. If C_1>C_2, it will move towards the direction of p_{best}, whereas if, C_1<C_2, it will move in the direction of g_{best}. In this paper, C_1 and C_2 are interpreted as linearly decreasing and linearly increasing functions, respectively with the help of the following equations:

$$C_{1(j)} = C_{1,\,max} - \frac{k}{k_{max}}\left(C_{1,max} - C_{1,min}\right) \tag{10}$$

$$C_{2(j)} = C_{2,\,min} \frac{k}{k_{max}}\left(C_{2,max} - C_{2,min}\right) \tag{11}$$

In equation (10) and (11), $C_{1,min}$, $C_{1,max}$ and $C_{2,min}$, $C_{2,max}$ are the minimum and maximum values of C_1 and C_2, respectively.

The authors claim the suggested approach has the following benefits. (1) Very high tracking efficiency of over 99.5%. (2) Easy to implement. (3) Guaranteed convergence in a reasonable time to the optimal solution. (4) Furthermore, only knowing the number of series cells is necessary for the proposed method; therefore, the system is independent.

A hybrid PSO algorithm which combines the conventional P&O and PSO algorithm is introduced by Lian et al. in 2014 [30]. The P&O algorithm first tracks the LMPP with the proposed method, and then the PSO actively seeks the GMPP in the second stage. This results in less search space in the second stage and quickly converges to GMPP. In 2016, Chaieb and Sakly introduced one of the other hybrid methods combining the Simplified Accelerated Particle Swarm Optimization (SAPSO) with the conventional Hill Climbing (HC) algorithm [31]. The author's aim was to develop an MPPT controller with high efficiency, quick response and less hardware and software requirements. For the validation of the proposed method under PSC it has been simulated and implemented for practical application. It shows that under PSC the HSAPSO system can track GMPP in the same exactness and efficiency with less hardware complexity and cost than the traditional PSO.

B. Artificial Bee Colony Algorithm (ABC)

ABC is a reasonably new swarm intelligence based algorithm for global optimization.It is introduced by Dervis Karaboga in the year 2005 [32], based on the foraging behavior of honey bees. The artificial bee colony consists of three fundamental groups. They are employed bees, onlooker bees and scout bees. Fifty percent of the bee colony comprised of employed bees and other fifty percent made up of onlooker bees. The food source selection, evaluation, memorization and exchange of information between the bees are the fundamental idea of artificial bee colony. Initially an employed bee goes to a food location to collect nectar and then it conveys the information about the location and quantity of the nectar to the employed bees with the help of waggle dance movements. The onlooker bees at the hive thus move towards the food location with the highest nectar and begin exploitation. The employed bee with abandoned food source will become a scout and go for searching of new locations.

i. Application of Artificial Bee Colony algorithm in MPPT

The flowchart of ABC algorithm used for MPPT in PV system under PSC is shown in Fig.4. Total size of the bee colony is equally divided as employed bees and onlooker bees. All employed bees are randomly chosen different duty cycles using equation (12)and then this duty cycle are updated with the help of equation (13) based on the output power quantity.

$$x_i = d_{min} + rand\left[0,1\right]\left(d_{max} - d_{min}\right) \tag{12}$$

$$x_{i\text{-}new} = x_i + \phi_i\left[\, x_i - x_k \,\right] \tag{13}$$

where, ϕ_i is an arbitrary variable selected between [-1,1]. The duty cycle with maximum power is optimized by comparing the probability factor associated with each duty cycle. The probability is calculated with the help of the following equation:

$$p_i = \frac{f_i}{\sum_{N=1}^{N_P} f_N} \tag{14}$$

where, f_i is the fitness factor of ith location and is calculated by equation (15):

$$f_i = \begin{cases} \dfrac{1}{1+Objval_i}; if\, Objval \geq 0 \\ 1+abs(Objval_i); Otherwise \end{cases} \tag{15}$$

where, *Objval* is the objective value at i[th] location. The process will reinitialize whenever there are changes in solar irradiation. The following condition of inequality characterizes this change in insolation.

$$\left|\frac{P_{pv} - P_{pv\_old}}{P_{pv\_old}}\right| \geq \Delta P_{pv}\% \tag{16}$$

This condition makes sure that, even if the solar irradiance changes, ABC algorithm is always able to track the GMPP [33].

Several researchers have conducted MPPT control in PV systems based on this algorithm. In 2015, A soufyane Benyoucef *et. al* [34] proposed ABC algorithm to be used in MPPT in PV systems. The authors examined this algorithm under different partial shading conditions and compared it to the PSO algorithm. For each shading pattern they executed this algorithm 200 times and concluded from the result that the ABC algorithm is performing better, specifically in terms of the number of successful convergences.

In 2013, the artificial bee colony MPPT algorithm was used by Bilal for photovoltaic plants [35]. The ABC algorithm to minimize the objective function is used here. For MPPT problems it is important to trace the maximum point at which power is maximum. To this end he proposed a transformation of the y axis to minimize objective function. The transformed power value is determined by the equation:

$$P' = 250 - P \tag{17}$$

where P is the instantaneous value of power. The maximum output power for the selected panel is 200W. So a transformation value of 250 is chosen for an efficient and non-interfering transformation. This transformation results in a mirror image of the PV curve. The author also compared the results of the ABC algorithm with those obtained by P&O for different shading patterns. Finally he concluded that at high irradiance levels ABC algorithm gives better results compared to P&O.

ABC MPPT was studied by Babar and Craciunescu in 2014 for use with PV systems and compared with other algorithms such as P&O, Fuzzy Logic Controllers (FLC), and Genetic Algorithm (GA) etc [19]. They used objective function maximization for maximum power extraction with certain functional modifications. The power is chosen as the objective function for MPPT problems. They noticed that the ABC algorithm was

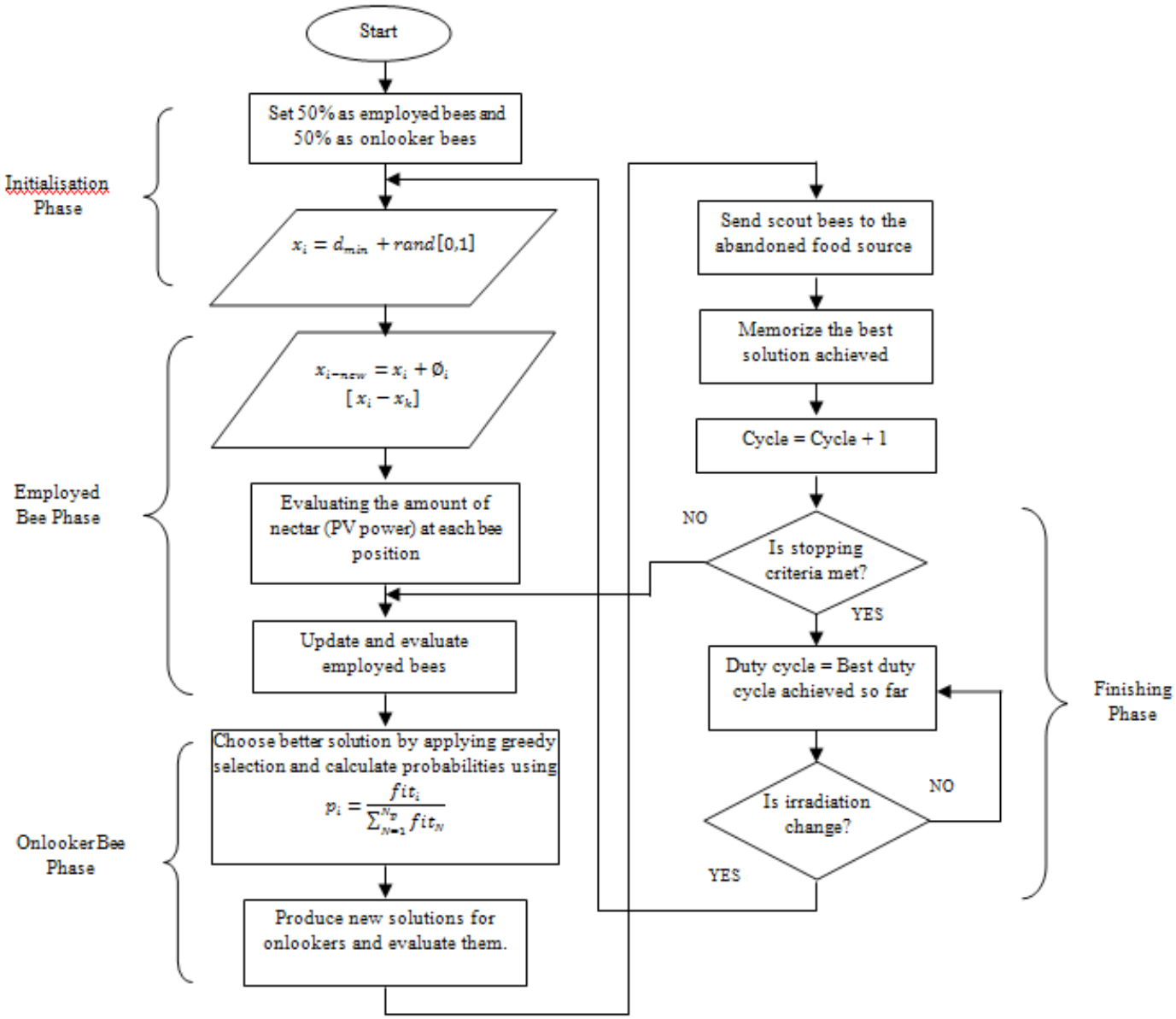

Fig. 4. Flowchart of ABC algorithm used for MPPT [36]

tracking MPP and extracting maximum power very quickly. These are; however, subject only to uniform insolation conditions.

The problem of MPPT under in-homogeneous insolation condition has been solved by Kinattingal Sundareswaran et. al in 2015 [37]. They developed an enhanced ABC algorithm in which the scout bee phase presented in the general ABC algorithm has been eliminated and included a new reinitiating search phase. In this phase, if the solar insolation changes (it will have an impact on change in the power output) the algorithm will get reinitiated. Any power output shift has been sensed and sampled in each 0.1s. They concluded that ABC has faster tracking characteristics and less oscillating power output. Based on the experimental validation of the developed approach, they conclude that the ABC algorithm shows better energy savings and revenue generation compared to other MPPT methods.

C. Ant Colony Optimization Algorithm (ACO)

Another prominent SI algorithm is ACO, proposed by Marco Dorigo in early nineties and effectively applied for several combinatorial optimization issues [38]. Later on, these algorithm has been used for many continuous optimization problems [39]-[40]. This is a probabilistic algorithm inspired by the social behavior of ants based on how they find an optimal path for searching of their food.

These ants randomly move along the search space to explore food source, while depositing pheromone on the ground in order to attract more members of the colony [41]. The quantity of pheromone on the moving path is directly proportional to the amount of food. Thus, the trail with largest amount of pheromone becomes the target path [42].

ACO_R is one of the main ACO based algorithm proposed by Socha and Dorigo in 2008 for continuous optimization problem [43]. Initially there are k arbitrary solution vectors are

chosen. The vectors $S_i(i=1,2..k)$ and its fitness function $f(s_i)$ in the archive are shown in Fig.5 [44]. The optimum solution is attained by updating all possible solutions in the archive until the stopping condition is met. The general procedure for generating solution for ACO_R based optimization problem includes the following three steps. They are initialization, generation of new solutions, and ranking and updating solution [45].

S_1	S_1^1	S_1^2	…	S_1^i	…	S_1^n	ω_1	$f(s_1)$
S_2	S_2^1	S_2^2	…	S_2^i	…	S_2^n	ω_2	$f(s_2)$
.	.	.	.	.	.	.	.	.
.	.	.	.	.	.	.	.	.
.	.	.	.	.	.	.	.	.
S_j	S_j^1	S_j^2		S_j^i		S_j^n	ω_i	$f(s_i)$
.	.	.	.	.	.	.	.	.
.	.	.	.	.	.	.	.	.
.	.	.	.	.	.	.	.	.
S_k	S_k^1	S_k^2	…	S_k^j	…	S_k^n	ω_k	$f(s_k)$
G^1	G^1	G^1	…	G^i	…	G^n		

Fig. 5. Solution generation process in ACOR [44]

Step 1: Initialization

In this step, initial values for all the parameters like, number of ants *(N)*, size of archive *(K)*, maximum number of iterations etc are selected. Then, *k* arbitrary solutions are generated and stored in the solution archive, with $k \geq N$, and further, based on the fitness value, all these solutions are ranked as: $f(s_1) \leq f(s_2) \leq \ldots \leq f(s_l) \leq \ldots \leq f(s_K)$[44].

Step 2: Generation of new solutions

For each dimension, new solutions are generated by sampling the probability density function which is represented by the following Gaussian kernel.

$$G_i(x) = \sum_{(l=1)}^{k} w_l g_l^i(x) = \sum_{l=1}^{k} w_l \frac{1}{\sigma_l^i \sqrt{2\pi}} exp\left(-\frac{(x-\mu_l^i)^2}{2\sigma_l^{i\,2}} \right) \tag{18}$$

where $G_i(x)$ is the Gaussian kernel for the ith solution and $g_l^i(x)$ is the lth sub-Gaussian function for the ith solution. The mean, and standard deviation is calculated by the following equations, respectively:

$$\mu^i = (\mu^i{}_1, \ldots, \mu^i{}_l, \ldots, \mu^i{}_\kappa,) = (s_1^i, \ldots, s_l^i, \ldots, s_\kappa^i) \tag{19}$$

$$\sigma_l^i = \xi \sum_{j=l}^{k} \frac{\left| s_j^i - s_l^i \right|}{K-1} \tag{20}$$

where ξ is the speed of convergence (as ξ increases, convergence time also increases) and S_l is the chosen solution.

Weight ω_l is given by the following equation:

$$w_l = \frac{1}{QK\sqrt{2\pi}} exp\left(-\frac{(l-1)^2}{2Q^2k^2} \right), \left(w_K \leq \ldots w_l \ldots \leq w_2 \leq w_1 \right) \tag{21}$$

where Q is a parameter representing the importance of the best ranked solution. More discussion about the parameters of Q and ξ can be found in paper[43]. The probability of choosing the Gaussian sub-function is based on the following equation (22):

$$p_l = \frac{w_l}{\sum_{r=1}^{r=k} w_r} \tag{22}$$

Step 3: Ranking and archive updating

The above process is repeated for every sample and generates *M* new solutions. Add the newly generated solutions to the original solutions and rank all these $M + K$ solutions. Then keep only the *K* best solutions in the archive. The whole procedure is repeated until the maximum iteration is reached or the termination conditions are satisfied.

i. Application of Ant Colony Optimization algorithm in MPPT

In order to apply ACO to find MPP in solar PV systems, ant's behavior in searching of food is mimicked by many researchers. The pheromone deposition at each location is considered as the output power at that location and the position of ant is considered as duty cycle. The following steps involved in the process of ACO for MPPT.

Step 1: In this step the number of ants and step size of ant's movement is fixed. Let the step size is labeled as 'ϑ_l', which decreases exponentially as the iteration proceeds. ϑ_l for k^{th} iteration is given by,

$$\vartheta_l(k) = \vartheta_0 e^{-k} \tag{23}$$

where ϑ_0 is initial step size.

Step 2: Locate these ants at different positions in the solution space. The minimum and maximum duty ratio is considered to be 10% to 90%. Thus the equal distribution of ants between 10% to 90% of duty ratio will guarantee to track the GMPP. (In the traditional ACO, random distribution of ants is deployed).

Step 3: The power output of the PV system is calculated for each ant position. The amount of pheromone at each location shall be considered to be the power at that location.

Step 4: The ant with maximum pheromone will continue to stay at its current position, and all other ants will update its position using the following equation [46]:

$$d_i^{k+1} = d_i + \vartheta_l \vec{a} \text{ Subjected to}$$

$$d_{imin} \leq d_i^{(k+1)} \leq d_{imax} \tag{24}$$

where is a unit vector. Iteration is said to be done if all the ants complete their action.

Step 5: Repeat steps 3 and 4 until all the ants converge to MPP.

L.L Jiang *et al.* in 2013 proposed ACO for MPPT under partial shading conditions [47]. In this paper, the authors successfully analyzed the relationship between convergence speed and tracking accuracy. As the number of ants increases, possibility to converge at the accurate duty cycle also increases. But it will take more time to converge all ants into the MPP. Smaller number of ants will give speedy convergence; conversely, they can simply happen to trapped on one of the LMPP. The viability

of this projected scheme is confirmed with the irradiance of different shading patterns by simulation. The correlation between the dimension of the archive and the proportion of the derived power for all the cases is examined in the paper.

In 2016, Sundareswaran *et al.* used 5s PV configuration with two different non uniform irradiance profiles in order to analyze the performance of ACO MPPT [46]. They have compared the conventional P&O with ACO and found that P&O method is a smoothly varying one with low ripple content in the output power but failed to track GMPP, whereas ACO is a promising method for tracking GMPP under PSC. Thus the authors have proposed a new MPPT method called ACO-PO, which combines the global search ability of ACO in the formative stages and local search ability of P&O in the later stages. This method possessed good static and dynamic tracking characteristics with lower CPU usage. Experimental analysis is also presented to validate the novelty of the proposed algorithm.

S. Titri et *al. in* 2017 [48], proposed a modified ACO MPPT algorithm called ACO-NPU-MPPT. They included a modification in the Pheromone updating strategy so as to reduce the computational time with high accuracy, less oscillations and increased robustness. Various tests are conducted for differently varying weather conditions and for different partial shading conditions. Validation of this algorithm has been performed by comparing it with some conventional, soft computing and biological methods.

D. Artificial Fish Swarm Algorithm (AFSA)

In 2002, Li *et al* proposed a new evolutionary swarm-based algorithm called Artificial fish swarm algorithm (AFSA) [49]. This algorithm is motivated by the intelligent behavior of fish swarms such as foraging, collision behavior and communication between fish individuals so as to reach the global optimum.

Artificial fish (AF) is an imaginary creature of real fish, which is used for carrying out the analysis and justification of a problem, and can be realized by means of animal ecology theory. The solution space for an AF is mainly the environment where it lives and the states of other AFs. The current state and the states of the nearby fish determine the next behavior of an AF [50]while the receiver has no knowledge of the transmitter spreading sequence, only knows the length of spreading sequence. The presented estimation method by Artificial Fish Swarm Algorithm (AFSA. Unlike in PSO algorithm, each AF keeps the current position and the companion's position to obtain the global best position, whereas in PSO past experiences are noted.

As shown in Fig. 6, AF observes external perception with its visual awareness. Current state of AF is denoted by vector X. The visual is equal to the visual distance, and X_V is the future place in visual where the AF determines to shift towards. If X_V has an improved food quantity than the current location, AF moves from X to X_{next}. Or else, continues in the current position and selects another spot in its vision.

Food density in location X is considered as the fitness value in that position, and denoted as *f(X)*. The maximum length of each step is denoted as 'step'. The distance between two AFs placed in X_i and X_j are determined by (Euclidean distance) [51].

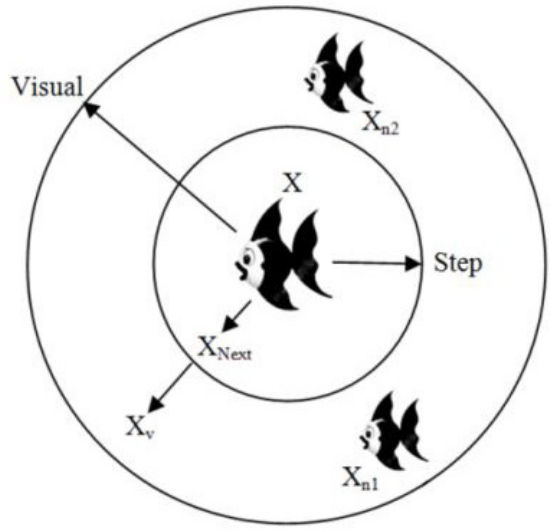

Fig. 6. Artificial Fish and the Environment [51]

This algorithm has been applied for many optimization problems and the different behaviors of fish are modeled mathematically as follows: [52]-[53].

(1) AF_Random Behavior:

The AF will move randomly in its area of vision. Let the current position be X_i. When it chooses another location, X_j, randomly it will move to that position. It is given by equation (25):

$$X_j = X_i + Visual \bullet rand() \tag{25}$$

where *rand()* is the random number between [-1,1].

(2) AF_Preying Behavior:

Let *F(X)* is the quantity of food at each location (objective function). If *F(Xi)>F(Xj)* in a minimization problem, it continues in the current direction using equation (26):

$$X_{i(t+1)} = X_{i(t)} + \frac{X_j - X_{i(t)}}{\left\| X_j - X_{i(t)} \right\|} \bullet Step \bullet rand() \tag{26}$$

Otherwise, again select another random state X_j and check whether it satisfies the condition. If it cannot satisfy after some limit number, it moves a step randomly using equation:

$$X_{i(t+1)} = X_{i(t)} + Visual * rand() \tag{27}$$

(3) AF_Swarming Behaviour:

AF searches its companion AF, denoted as X_c, in its neighborhood. If X_c has more food quantity than X_i, and the crowd factor of X_c is less than X_i, AF move towards X_c using the equation (28):

$$X_{i(t+1)} = X_{i(t)} + \frac{X_c - X_{i(t)}}{\left\| X_c - X_{i(t)} \right\|} * Step * rand() \tag{28}$$

Otherwise it will follow the preying behavior.

(4) AF_Following Behaviour:

An AF at position X_i find X_{max} with $F(X_{max})$ is the maximum value in the near fields, and position of X_{max} is not too crowded, then follows equation .

$$X_{i(t+1)} = X_{i(t)} + \frac{X_{max} - X_{i(t)}}{\left\| X_{max} - X_{i(t)} \right\|} * Step * rand() \tag{29}$$

(5) AF_LeapingBehaviour:

In order to avoid setting up on local minima, AF will leap out of the current state, if there is no big difference in the food concentration, after some iteration and is determined by equation (30):

$$If\left(F\left(X_i\right) - F\left(X_j\right)\right) < eps \tag{30}$$

The new location is given by

$$X_{(t+1)} = \delta X_{(t)} + \quad * Visual * () rand \tag{31}$$

where is a parameter which will allow the AF to have some other abnormal behavior, and *eps* is a constant.

(6) AF_BulletinBehaviour:

This behavior is used to memorize the food concentration at current location and the optimal AF's state. Each time the bulletin is updated and the optimal value is the final value of the bulletin. The algorithm will get terminated after completing the given number of iteration or a steady state of error range is achieved in the bulletin.

The process of AFSA is shown as follows:

(a) Initialize the AFSA parameters: Population of AF, Iteration time, Step, Visual, Crowd factor (δ), try_number.

(b) Randomly generate position of AF using equation .

(c) Update the position of each AF using the four behaviors: Preying, Swarming, Following, Leaping, and Bulletin.

(d) Evaluation and fitness value of each AF is calculated. If better food location is not found after try_number, AF moves randomly.

(e) Repeat step c until termination criteria is satisfied.

i. Application of AFSA in MPPT

The position of AF is represented as the optimal duty ratio of the converter for MPPT control in PV systems. The objective function to be optimized is given as

$$\textit{Maximize Ppv (d)}$$
$$\textit{Subject to the constraint: } d_{min} \le d \le d_{max}.$$

where d is the duty cycle, d_{min} and d_{max} represents minimum and maximum duty cycle values.

Being attracted by the prospective of the AFSA, many improvements for the ordinary AFSA have been developed recently. M. Mao *et al.* [54] proposed a modified AFSA based MPPT for grid connected PV system in 2017. The authors introduced some characteristics of PSO algorithm to the ordinary AFSA in order to improve its performance.

Initially they introduced the speed parameter of particle to each of the artificial fishes. The equation for speed of particle is updated as follows:

$$V_{i(t+1)} = wV_{i(t)} + \frac{X_c - X_{i(t)}}{\left\| X_c - X_{i(t)} \right\|} * Step * rand() \tag{32}$$

Secondly, memory is introduced and this makes the AF to swim around its optimal position. Thus the updated speed equation is:

$$\mathrm{V}_{\mathrm{i(t+1)}} = \omega \mathrm{V}_{\mathrm{i(t)}} + \frac{X_{pbest} - X_{i(t)}}{\left\| X_{pbest} - X_{i(t)} \right\|} * step * rand\ () \tag{33}$$

Thirdly, the communication behavior is introduced and updated the equation as shown in equation (34):

$$V_{i(t+1)} = wV_{i(t)} + \frac{X_{gbest} - X_{i(t)}}{\left\| X_{gbest} - X_{i(t)} \right\|} * Step * rand() \tag{34}$$

where X_{gbest} is the global optimum position of AF.

In this paper, the objective function to be maximized is formulated as the P-I characteristics of the series connected panels as shown in equation (35):

$$fit = I * \sum_{k=1}^{n_s} PV_{prog}\left(I_k, Sun_k, T_k\right), ns \tag{35}$$

where, PV_{prog} *(I, Sun, T)* is the characteristic function of output power versus current. *I* is the current, and *Sun* and *T* represent irradiance and temperature respectively.

In paper [56]to maximize the performance of photovoltaic devices, Maximum Power Point Tracking (MPPT the authors implemented the AFSA for MPPT control of a single-stage PV grid-connected system. The optimal power output is extracted by tuning the parameters of AFSA by simulation. The authors considered three different schemes for obtaining the optimum values for iteration number and fish scale. It is also concluded that as the iteration count increases there is an improvement in output but the convergence time increases. Maximum power output with minimum time has been obtained in third scheme, by simultaneously changes the number of AF and number of iterations. The output is compared with traditional P&O MPPT control method. The authors proved the effectiveness and reliability of the proposed AFSA method with both simulation and experimental analysis.

The advantages of AFSA include high accuracy, flexibility, global search ability, fast convergence and fault tolerance. Whereas it has some disadvantages such as high time complexity, lack of stability among global and local search.

V. Other SI based Algorithms

More over to the above discussed algorithms, some of the recently developed SI algorithms are reviewed in this paper based on the inspiration and advantages. Table 1 shows the comparison of newly introduced SI optimization algorithms used for MPPT control under PSC.

Table I.
Comparison of Different Si Based Algorithms Used in Solar PV Systems under Partial Shading Conditions

SL NO	MPPT	Introduced by	Introduced on	Inspiration	Advantages
1	Ant Colony Optimization (ACO) [38] [55]	Marco Dorigo	1999	Foraging behavior of ant colony	Convergence does not depend upon the first location of the sample, low cost, easy control, robust to different shading conditions.
2	Particle Swarm Optimization (PSO) [24] [30]	Kennedy and Eberhart	1995	Bird Flock trying to reach an unknown destination	Simplicity of implementation, scalability in dimension, and good empirical performance.
3	Artificial fish Swarm Algorithm (AFSA) [56] [49]	Li Xiaole et al.	2002	Foraging, cluster and collision behavior and mutual assistance between fish swarm	Convergence does not depend upon the initial location of the artificial fish, flexible and fault tolerance.
4	Artificial Bee Colony (ABC) [32] [37] [57]	Dervis Karaboga	2005	Foraging behavior of honey bees	Convergence is independent of initial conditions, Simple, uses less control parameters
5	Cat Swarm Optimization (CSO) [58] [59]	Shu-Chuan Chuet al.	2007	Natural behavior of cats	System independent, High tracking accuracy and fast convergence, No oscillations around MPP, Efficient to track GMPP
6	Firefly Algorithm (FA) [60]	Xin She Yang	2007	Flashing patterns of the firefly	Automatic subdivision of the whole population into subgroups, multimodal optimization, high ergodicity and diversity in the solutions
7	Cuckoo Search Algorithm (CSA) [61]	Yang and Deb	2009	Breeding behavior of cuckoos	High efficiency, Fast convergence, efficient randomization, less tuning parameters required and Robust technique
8	Bat Algorithm (BA) [62]	Yang and Gandomi	2010	Echolocation behavior of Microbats	Simple and flexible, easy to implement quick convergence to GMPP
9	Grey Wolf Optimization (GWO) [63]	Mirjalili et al.	2014	Leadership hierarchy and hunting mechanism of Grey wolve	Robust, High efficiency, few parameters required for tuning, Transient and steady state oscillations are zero.
10	Chicken Swarm Optimization (CSO) [19]	XianbingMeng et al.	2014	The behaviors of the chicken swarm.	Robust, better convergence, high efficiency.
11	Spider Monkey Optimization algorithm (SMO) [64]	Jagdish Chand Bansal et al.	2014	Fission-fusion social behavior of spider monkeys	Fast and accurate convergence
12	Ant Lion Optimizer (ALO) [65]	SeyedaliMirjalili	2015	Hunting mechanism of ant-lions in nature	Tracking true power point under PSC.
13	Dragonfly Algorithm (DA) [66]	SeyedaliMirjalili	2015	Hunting and migration swarming behaviors of dragon flies	Good exploration and exploitation characteristic, fast tracking, less energy loss and system independent
14	Whale Optimization Algorithm (WOA) [67]	Mirjalili et al.	2016	Behaviors of humpback whale	High accuracy, Fast tracking

VI. Conclusion

As far as the photovoltaic system concerned, the maximum power point differs with respect to the atmospheric conditions. Consequently the MPPT control techniques also gained importance to crop maximum power from PV systems. During partial shading conditions the chances of falling into local power peaks is high because of the presence of multiple power peaks in the P-V curve. In such cases, the tracking of global power peak is essential. In this article, a comprehensive review of swarm intelligence optimization control algorithms to track global power for photovoltaic systems under partial shading condition is presented. The review presented the recently emerging optimization algorithms and its application in PV system for tracking global maximum power point. The methods are compared in terms of their swarm intelligence and advantages.

References

[1] F. Lamnabhi-Lagarrigue *et al.*, "Systems & Control for the future of humanity, research agenda: Current and future roles, impact and grand challenges," *Annu. Rev. Control*, vol. 43, pp. 1–64, 2017, doi: 10.1016/j.arcontrol.2017.04.001.

[2] B. Parida, S. Iniyan, and R. Goic, "A review of solar photovoltaic technologies," *Renew. Sustain. Energy Rev.*, vol. 15, no. 3, pp. 1625–1636, 2011, doi: 10.1016/j.rser.2010.11.032.

[3] M. Premkumar, T.R.Sumithira, and R.Sowmya, "Implementation of Solar PV Based Microconverter With Optimal Mppt Control," *J. Electr. Eng.*, vol. 18, no. 2, pp. 1–12, 2018.

[4] B. Pakkiraiah and G. D. Sukumar, "Research Survey on Various MPPT

Performance Issues to Improve the Solar PV System Efficiency," *J. Sol. Energy*, vol. 2016, pp. 1–20, 2016, doi: 10.1155/2016/8012432.

[5] D. Pilakkat and S. Kanthalakshmi, "Drift Free Variable Step Size Perturb and Observe MPPT Algorithm for Photovoltaic Systems Under Rapidly Increasing Insolation," *Electron. J.*, vol. 22, no. 1, pp. 19–26, 2018, doi: 10.7251/ELS1822019P.

[6] M. Killi and S. Samanta, "Modified perturb and observe MPPT algorithm for drift avoidance in photovoltaic systems," *IEEE Trans. Ind. Electron.*, vol. 62, no. 9, pp. 5549–5559, 2015, doi: 10.1109/TIE.2015.2407854.

[7] R. I. Putri, S. Wibowo, and M. Rifa'i, "Maximum power point tracking for photovoltaic using incremental conductance method," in *Energy Procedia*, 2015, vol. 68, pp. 22–30, doi: 10.1016/j.egypro.2015.03.228.

[8] M. A. Elgendy, B. Zahawi, and D. J. Atkinson, "Assessment of the Incremental Conductance Maximum Power Point Tracking Algorithm," *Sustain. Energy, IEEE Trans.*, vol. 4, no. 1, pp. 108–117, 2013, doi: 10.1109/TSTE.2012.2202698.

[9] J. Ahmad, "A fractional open circuit voltage based maximum power point tracker for photovoltaic arrays," *IEEE Int. Conf. Softw. Technol. Eng.*, vol. 1, pp. 247–250, 2010, doi: 10.1109/ICSTE.2010.5608868.

[10] T. Kato, T. Miyake, D. Tashima, T. Sakoda, M. Otsubo, and M. Hombu, "Maximum output power control using short-circuit current and open-circuit voltage of a solar panel," *Jpn. J. Appl. Phys.*, vol. 51, no. 10 PART 2, 2012, doi: 10.1143/JJAP.51.10NF08.

[11] M. Kermadi and E. M. Berkouk, "Artificial intelligence-based maximum power point tracking controllers for Photovoltaic systems: Comparative study," *Renewable and Sustainable Energy Reviews*, vol. 69. pp. 369–386, 2017, doi: 10.1016/j.rser.2016.11.125.

[12] A. M. Palaniswamy and K. Srinivasan, "Takagi-Sugeno fuzzy approach for power optimization in standalone photovoltaic systems," *Sol. Energy*, vol. 139, pp. 213–220, 2016, doi: 10.1016/j.solener.2016.09.027.

[13] M. M. Algazar, H. AL-monier, H. A. EL-halim, and M. E. E. K. Salem, "Maximum power point tracking using fuzzy logic control," *Int. J. Electr. Power Energy Syst.*, vol. 39, no. 1, pp. 21–28, 2012, doi: 10.1016/j.ijepes.2011.12.006.

[14] J. K. Patra, S. B. Mohanty, H. M. Tania, D. Elangovan, and G. Arunkumar, "Application of bio-inspired MPPT techniques for photovoltaic system," in *Lecture Notes in Electrical Engineering*, 2017, vol. 394, pp. 345–352, doi: 10.1007/978-981-10-1540-3_36.

[15] S. Yang and Y. Sato, "Swarm Intelligence Algorithm Based on Competitive Predators with Dynamic Virtual Teams," *J. Artif. Intell. Soft Comput. Res.*, vol. 7, no. 2, pp. 87–101, 2017, doi: 10.1515/jaiscr-2017-0006.

[16] B. Babar and A. Crăciunescu, "Comparison of Artificial Bee Colony Algorithm with other Algorithms used for Tracking of Maximum Power Point of Photovoltaic Arrays," *Int. Conf. Renew. Energies Power Qual.*, vol. 1, no. 12, pp. 1005–1008, 2014.

[17] M. Abdullah, A. Yatim, C. W. Tan, and A. S. Samosir, "Particle swarm optimization-based maximum power point tracking algorithm for wind energy conversion system," *2012 IEEE Int. Conf. Power Energy*, no. December, pp. 65–70, 2012, doi: 10.1109/PECon.2012.6450296.

[18] A. S. Oshaba, E. S. Ali, and S. M. Abd Elazim, "BAT algorithm: A novel approach for MPPT control design of PV generator supplied SRM," *J. Electr. Eng.*, vol. 15, no. 1, pp. 293–302, 2015.

[19] Z. Wu, D. Yu, and X. Kang, "Application of improved chicken swarm optimization for MPPT in photovoltaic system," *Optim. Control Appl. Methods*, vol. 39, no. 2, pp. 1029–1042, 2018, doi: 10.1002/oca.2394.

[20] B. Zolghadr-Asli, O. Bozorg-Haddad, and X. Chu, "Krill herd algorithm (KHA)," in *Studies in Computational Intelligence*, vol. 720, 2018, pp. 69–79.

[21] S. Mohanty, B. Subudhi, and P. K. Ray, "A new MPPT design using grey Wolf optimization technique for photovoltaic system under partial shading conditions," *IEEE Trans. Sustain. Energy*, vol. 7, no. 1, pp. 181–188, 2016, doi: 10.1109/TSTE.2015.2482120.

[22] S. Kumar Dash, S. Nema, R. K. Nema, and D. Verma, "A comprehensive assessment of maximum power point tracking techniques under uniform and non-uniform irradiance and its impact on photovoltaic systems: A review," *J. Renew. Sustain. Energy*, vol. 7, pp. 1–28, 2015, doi: 10.1063/1.4936572.

[23] B. N. Alajmi, K. H. Ahmed, S. J. Finney, and B. W. Williams, "A maximum power point tracking technique for partially shaded photovoltaic systems in microgrids," *IEEE Trans. Ind. Electron.*, vol. 60, no. 4, pp. 1596–1606, 2013, doi: 10.1109/TIE.2011.2168796.

[24] J. K. and R. Eberhart, "Particle swarm optimization," in *Proceedings of the IEEE International Conference on Neural Networks*, 1995, pp. 1942–1948, doi: 10.1109/ICNN.1995.488968.

[25] W. Qiao, G. K. Venayagamoorthy, and R. G. Harley, "Design of Optimal PI Controllers for Doubly Fed Induction Generators Driven by Wind Turbines Using Particle Swarm Optimization," *Int. Jt. Conf. Neural Networks, 2006. IJCNN '06*, pp. 1982–1987, 2006.

[26] M. Miyatake, F. Toriumi, T. Endo, and N. Fujii, "A Novel maximum power point tracker controlling several converters connected to photovoltaic arrays with particle swarm optimization technique," in *Power Electronics and Applications, 2007 European Conference on*, 2007, pp. 1–10, doi: 10.1109/EPE.2007.4417640.

[27] V. Phimmasone, T. Endo, Y. Kondo, and M. Miyatake, "Improvement of the maximum power point tracker for photovoltaic generators with particle swarm optimization technique by adding repulsive force among agents," *2009 Int. Conf. Electr. Mach. Syst. Tokyo*, pp. 1–6, 2009, doi: 10.1109/ICEMS.2009.5382713.

[28] K. Ishaque and Z. Salam, "A Deterministic Particle Swarm Optimization Maximum Power Point Tracker for Photovoltaic System under Partial Shading Condition," *IEEE Trans. Ind. Electron.*, vol. 60, no. 8, pp. 3195–3206, 2012, doi: 10.1109/TIE.2012.2200223.

[29] Y. H. Liu, S. C. Huang, J. W. Huang, and W. C. Liang, "A particle swarm optimization-based maximum power point tracking algorithm for PV systems operating under partially shaded conditions," *IEEE Trans. Energy Convers.*, vol. 27, no. 4, pp. 1027–1035, 2012, doi: 10.1109/TEC.2012.2219533.

[30] K. L. Lian, J. H. Jhang, and I. S. Tian, "A maximum power point tracking method based on perturb-and-observe combined with particle swarm optimization," *IEEE J. Photovoltaics*, vol. 4, no. 2, pp. 626–633, 2014, doi: 10.1109/JPHOTOV.2013.2297513.

[31] H. Chaieb and A. Sakly, "A novel MPPT method for photovoltaic application under partial shaded conditions," *Sol. Energy*, vol. 159, pp. 291–299, 2018, doi: 10.1016/j.solener.2017.11.001.

[32] D. Karaboga, "An idea based on Honey Bee Swarm for Numerical Optimization," *Tech. Rep. TR06, Erciyes Univ.*, no. TR06, p. 10, 2005, doi: citeulike-article-id:6592152.

[33] D. Pilakkat and S. Kanthalakshmi, "Artificial Bee Colony Algorithm for Peak Power Point Tracking of a Photovoltaic System under Partial Shading Condition," *2018 Int. Conf. Curr. Trends Towar. Converging Technol.*, pp. 1–7, 2018.

[34] A. soufyane Benyoucef, A. Chouder, K. Kara, S. Silvestre, and O. A. Sahed, "Artificial bee colony based algorithm for maximum power point tracking (MPPT) for PV systems operating under partial shaded conditions," *Appl. Soft Comput. J.*, vol. 32, pp. 38–48, 2015, doi: 10.1016/j.asoc.2015.03.047.

[35] B. Bilal, "Implementation of Artificial Bee Colony algorithm on Maximum Power Point Tracking for PV modules," *8th Int. Symp. Adv. Top. Electr. Eng.*, pp. 1–4, 2013, doi: 10.1109/ATEE.2013.6563495.

[36] D. Pilakkat and S. Kanthalakshmi, "An improved P&O algorithm integrated with artificial bee colony for photovoltaic systems under partial shading conditions," *Sol. Energy*, vol. 178, pp. 37–47, 2019, doi: 10.1016/j.solener.2018.12.008.

[37] K. Sundareswaran, P. Sankar, P. S. R. Nayak, S. P. Simon, and S. Palani, "Enhanced Energy Output From a PV System Under Partial Shaded Conditions Through Artificial Bee Colony," *Ieee Trans. Sustain. Energy*, vol. 6, no. 1, pp. 198–209, 2015, doi: 10.1109/TSTE.2014.2363521.

[38] M. Dorigo and G. Di Caro, "The Ant Colony Optimization Meta-Heuristic," in *New Ideas in Optimization*, 1999.

[39] G. Bilchev and I. C. Parmee, "The ant colony metaphor for searching continuous design spaces," *Lect. Notes Comput. Sci. (including Subser. Lect. Notes Artif. Intell. Lect. Notes Bioinformatics)*, vol. 993, pp. 25–39, 1995, doi: 10.1007/3-540-60469-3_22.

[40] W. Tfaili and P. Siarry, "A new charged ant colony algorithm for continuous dynamic optimization," *Appl. Math. Comput.*, vol. 197, no. 2, pp. 604–613, 2008, doi: 10.1016/j.amc.2007.08.087.

[41] M. Dorigo, M. Birattari, and T. Stutzle, "Ant colony optimization," *IEEE Comput. Intell. Mag.*, vol. 1, no. 4, pp. 28–39, 2006, doi: 10.1109/MCI.2006.329691.

[42] S.-J. Huang, "Enhancement of hydroelectric generation scheduling using ant colony system based optimization approaches," *IEEE Trans. Energy Convers.*, vol. 16, no. 3, pp. 296–301, 2001, doi: 10.1109/60.937211.

[43] K. Socha and M. Dorigo, "Ant colony optimization for continuous domains," *Eur. J. Oper. Res.*, vol. 185, no. 3, pp. 1155–1173, 2008, doi: 10.1016/j.ejor.2006.06.046.

[44] L. L. Jiang, D. L. Maskell, and J. C. Patra, "A novel ant colony optimization-based maximum power point tracking for photovoltaic systems under partially shaded conditions," *Energy Build.*, vol. 58, pp. 227–236, 2013, doi: 10.1016/j.enbuild.2012.12.001.

[45] L. L. Jiang and D. L. Maskell, "A uniform implementation scheme for evolutionary optimization algorithms and the experimental implementation of an ACO based MPPT for PV systems under partial shading," in *IEEE Symposium on Computational Intelligence Applications in Smart Grid, CIASG*, 2015, vol. 2015-Janua, no. January, doi: 10.1109/CIASG.2014.7011560.

[46] K. Sundareswaran, V. Vigneshkumar, P. Sankar, S. P. Simon, P. Srinivasa Rao Nayak, and S. Palani, "Development of an Improved P&O Algorithm Assisted Through a Colony of Foraging Ants for MPPT in PV System," *IEEE Trans. Ind. Informatics*, vol. 12, no. 1, pp. 187–200, 2016, doi: 10.1109/TII.2015.2502428.

[47] L. L. Jiang, D. L. Maskell, and J. C. Patra, "A novel ant colony optimization-based maximum power point tracking for photovoltaic systems under partially shaded conditions," *Energy Build.*, vol. 58, pp. 227–236, 2013, doi: 10.1016/j.enbuild.2012.12.001.

[48] S. Titri, C. Larbes, K. Y. Toumi, and K. Benatchba, "A new MPPT controller based on the Ant colony optimization algorithm for Photovoltaic systems under partial shading conditions," *Appl. Soft Comput. J.*, vol. 58, pp. 465–479, 2017, doi: 10.1016/j.asoc.2017.05.017.

[49] X. X. Li, Z. Shao, and J. Qian, "An optimizing method based on autonomous animals: fish-swarm algorithm," *Syst Eng Theory Prat.*, vol. 22, no. 11, pp. 32–38, 2002.

[50] M. Jiang, Y. Wang, F. Rubio, and D. Yuan, "Spread spectrum code estimation by artificial fish swarm algorithm," in *2007 IEEE International Symposium on Intelligent Signal Processing, WISP*, 2007, doi: 10.1109/WISP.2007.4447587.

[51] R. Azizi, "Empirical Study of Artificial Fish Swarm Algorithm," *Int. J. Comput. Commun. Netw.*, vol. 3, no. 1, pp. 1–7, 2014, doi: 10.7763/IJCCE.2014.V3.281.

[52] M. Neshat, G. Sepidnam, M. Sargolzaei, and A. N. Toosi, "Artificial fish swarm algorithm: a survey of the state-of-the-art, hybridization, combinatorial and indicative applications," *Artif. Intell. Rev.*, vol. 42, no. 4, pp. 965–997, 2014, doi: 10.1007/s10462-012-9342-2.

[53] M. S. R. Nalluri, T. SaiSujana, K. Harshini Reddy, and V. Swaminathan, "An efficient feature selection using artificial fish swarm optimization and SVM classifier," in *2017 International Conference on Networks and Advances in Computational Technologies, NetACT 2017*, 2017, doi: 10.1109/NETACT.2017.8076805.

[54] M. Mao, Q. Duan, P. Duan, and B. Hu, "Comprehensive improvement of artificial fish swarm algorithm for global MPPT in PV system under partial shading conditions," *Trans. Inst. Meas. Control*, vol. 40, no. 7, pp. 2178–2199, 2018, doi: 10.1177/0142331217697374.

[55] G. Li, Y. Jin, M. W. Akram, X. Chen, and J. Ji, "Application of bio-inspired algorithms in maximum power point tracking for PV systems under partial shading conditions – A review," *Renew. Sustain. Energy Rev.*, vol. 81, no. August 2017, pp. 840–873, 2018, doi: 10.1016/j.rser.2017.08.034.

[56] S. Q. Li, B. Zhang, T. J. Xu, and J. Yang, "A new MPPT control method of photovoltaic grid-connected inverter system," *26th Chinese Control Decis. Conf. CCDC 2014*, pp. 2753–2757, 2014, doi: 10.1109/CCDC.2014.6852640.

[57] D. Pilakkat and S. Kanthalakshmi, "Artificial Bee Colony Integrated P&O Algorithm for Single Phase Grid Connected Photovoltaic Application," *Int. J. Instrum. Meas.*, vol. 4, pp. 45–52, 2019.

[58] S. C. Chu and P. W. Tsai, "Computational intelligence based on the behavior of cats," *Int. J. Innov. Comput. Inf. Control*, vol. 3, no. 1, pp. 163–173, 2007.

[59] G. U. O. Xiu-cai and X. U. Dan, "Application of Improved Cat Swarm Optimization in MPPT Control of Photovoltaic Arrays," *IOP Conf. Ser. Earth Environ. Sci.*, vol. 153, no. 3, pp. 20–24, 2018.

[60] K. Sundareswaran, S. Peddapati, and S. Palani, "MPPT of PV systems under partial shaded conditions through a colony of flashing fireflies," *IEEE Trans. Energy Convers.*, vol. 29, no. 2, pp. 463–472, 2014, doi: 10.1109/TEC.2014.2298237.

[61] J. Ahmed and Z. Salam, "A soft computing MPPT for PV system based on Cuckoo Search algorithm," *Int. Conf. Power Eng. Energy Electr. Drives*, no. May, pp. 558–562, 2013, doi: 10.1109/PowerEng.2013.6635669.

[62] M. K. Karagöz and H. Demİrel, "A Novel MPPT Method for PV Arrays Based on Modified Bat Algorithm with Partial Shading Capability," *IJCSNS Int. J. Comput. Sci. Netw. Secur.*, vol. 17, no. 2, pp. 61–66, 2017.

[63] S. Mohanty, B. Subudhi, S. Member, and P. K. Ray, "A New MPPT Design Using Grey Wolf Optimization Technique for Photovoltaic System Under Partial Shading Conditions," *IEEE Trans. Sustain. Energy*, vol. 7, no. 1, pp. 181–188, 2016.

[64] T. K. Behera, M. K. Behera, and N. Nayak, "Spider monkey based improve P&O MPPT controller for photovoltaic generation system," *2018 Technol. Smart-City Energy Secur. Power (ICSESP), Bhubaneswar*, pp. 1–6, 2018, doi: 10.1109/ICSESP.2018.8376735.

[65] E. A. Engel and I. V. Kovalev, "MPPT of a partially shaded photovoltaic module by ant lion optimizer," in *Lecture Notes in Computer Science (including subseries Lecture Notes in Artificial Intelligence and Lecture Notes in Bioinformatics)*, 2016, pp. 451–457.

[66] G. Raman, G. Raman, C. Manickam, and S. I. Ganesan, "Dragonfly Algorithm Based Global Maximum Power Point Tracker for Photovoltaic Systems," in *Tan Y., Shi Y., Niu B. (eds) Advances in Swarm Intelligence. ICSI 2016. Lecture Notes in Computer Science*, 2016, vol. 9712, no. 1, pp. 211–219, doi: 10.1007/978-3-642-38703-6.

[67] S. K. Cherukuri and S. R. Rayapudi, "A Novel Global MPP Tracking of Photovoltaic System based on Whale Optimization Algorithm," *Int. J. Renew. Energy Dev.*, vol. 5, no. 3, p. 225, 2016, doi: 10.14710/ijred.5.3.225-232.

Revisiting Analytical Models of N-Type Symmetric Double-Gate MOSFETs

Rekib Uddin Ahmed and Prabir Saha

***Abstract*—Nowadays, the endlessly increasing demand for faster and complex integrated circuits (IC) has been fuelled by the scaling of metal-oxide-semiconductor field-effect-transistors (MOSFET) to smaller dimensions. The continued scaling of MOSFETs approaches its physical limits due to short-channel effects (SCE). Double-gate (DG) MOSFET is one of the promising alternatives as it offers better immunity towards SCEs and can be scaled to the shortest channel length. In future, ICs can be designed using DG-CMOS technology for which mathematical models depicting the electrical characteristics of the DG MOSFETs are foremost needed. In this paper, a review on n-type symmetric DG MOSFETs models has been presented based on the analyses of electrostatic potential distribution, threshold voltage, and drain-current models. Mathematical derivations of the device models are described elaborately, and numerical simulations are also carried out to validate the replicability of models.**

***Index Terms*—Analytical modeling, drain-current, n-type DG MOSFETs, potential distribution, review, threshold voltage.**

Original Research Paper
DOI: 10.7251/ELS2024015A

I. Introduction

For more than five decades, the semiconductor industries have been successful in providing continuous system performance improvement because of the invention of MOSFETs. Prior to this, bulky vacuum tubes were used for systems, but reliability and heat dissipations were major issues [1]. Therefore, researchers tried to realize the vacuum tube in solid-state for which the surface of semiconductors was studied thoroughly. Lilienfeld first reported the idea of enhancing the surface conductance of a semiconductor by application of electric field in 1930, but it was not successful because of the presence of large densities of surface states [2]-[3]. The first MOSFET was fabricated in 1960 by Kahng and Atalla [4] on a silicon substrate using an oxide layer (SiO_2) as the gate insulator. Circuits based on single polarity MOSFETs (either p- or n-type) suffered from large static power dissipation, thereby limited the level of integration in a chip. The breakthrough in the level of integration came in 1963 with the invention of complementary metal-oxide-semiconductor (CMOS) [5]. In CMOS technology, both the n- and p-type MOSFETs were constructed side by side on the same substrate, and are connected in series between the supply terminals, so that there is negligible static power dissipation.

The prediction proclaimed by Moore's law has been achieved through scaling of MOSFETs. One of the most important parameters of a MOSFET is its channel length (L), defined as the distance between the source and drain. For a given technology, there is a minimum value of L below which the gate starts to lose control of the drain current (I_{ds}). This is because of the physical limits imposed by non-scalability of silicon energy band-gap (E_g), built-in potential (V_{bi}), short-channel effects (SCEs), and thermal voltage (V_T) [6]. Conventionally, MOSFETs were scaled with a scaling factor s, ($s \approx 0.7$). Scaling by this factor reduces L to $L \times s$, oxide thickness (t_{ox}) to $t_{ox} \times s$, while it increases doping concentration (N_{si}) to N_{si}/s [7]. But this technique cannot be continued in the sub-micron regime, because increasing N_{si} gives rise to mobility degradation of carriers and random dopant fluctuation (RDF) [7,8]. Mobility degradation occurs due to large vertical fields induced by high doping [9]. RDF is a form of process variation due to variation in the implanted dopants which alters the transistor's properties, especially threshold voltage (V_{th}) [10]. So it is utmost important to restore the gate control of the channel without increasing doping concentration of the body. This requirement has led to creating multi-gate (MG) MOSFETs in which body of the device is undoped (or lightly doped). Fig.1 shows some examples of MG MOSFETs where the gate is wrapped around the body from either two or three or four sides.

On decreasing the L, depletion region created by the source and drain encroaches horizontally in the channel, thereby reduces the effective channel length [11]. As the drain-to-source voltage (V_{ds}) increases the depletion region becomes wider. As a result, the channel electrostatics is not only controlled by the gate but also influenced by L and V_{ds}. The observable effects arising due to loss of channel electrostatics controlled by the gate are termed as SCEs. The SCEs include the V_{th} roll-off due to the L reduction, and the drain-induced

Manuscript received 4 October 2019. Received in revised form 18 February 2020. Accepted for publication 5 March 2020.

This work was supported in part by the National Institute of Technology Meghalaya and in part by Visvesvaraya PhD Scheme, Government of India.

Rekib Uddin Ahmed is with the Department of Electronics and Communication Engineering, National Institute of Technology Meghalaya, Shillong 793003, India (e-mail: rekib@nitm.ac.in; phone: +919436594902; fax: +91364-2501113).

Prabir Saha is with the Department of Electronics and Communication Engineering, National Institute of Technology Meghalaya, Shillong 793003, India (e-mail: sahaprabir1@gmail.com; phone: +919485177005; fax: +91364-2501113).

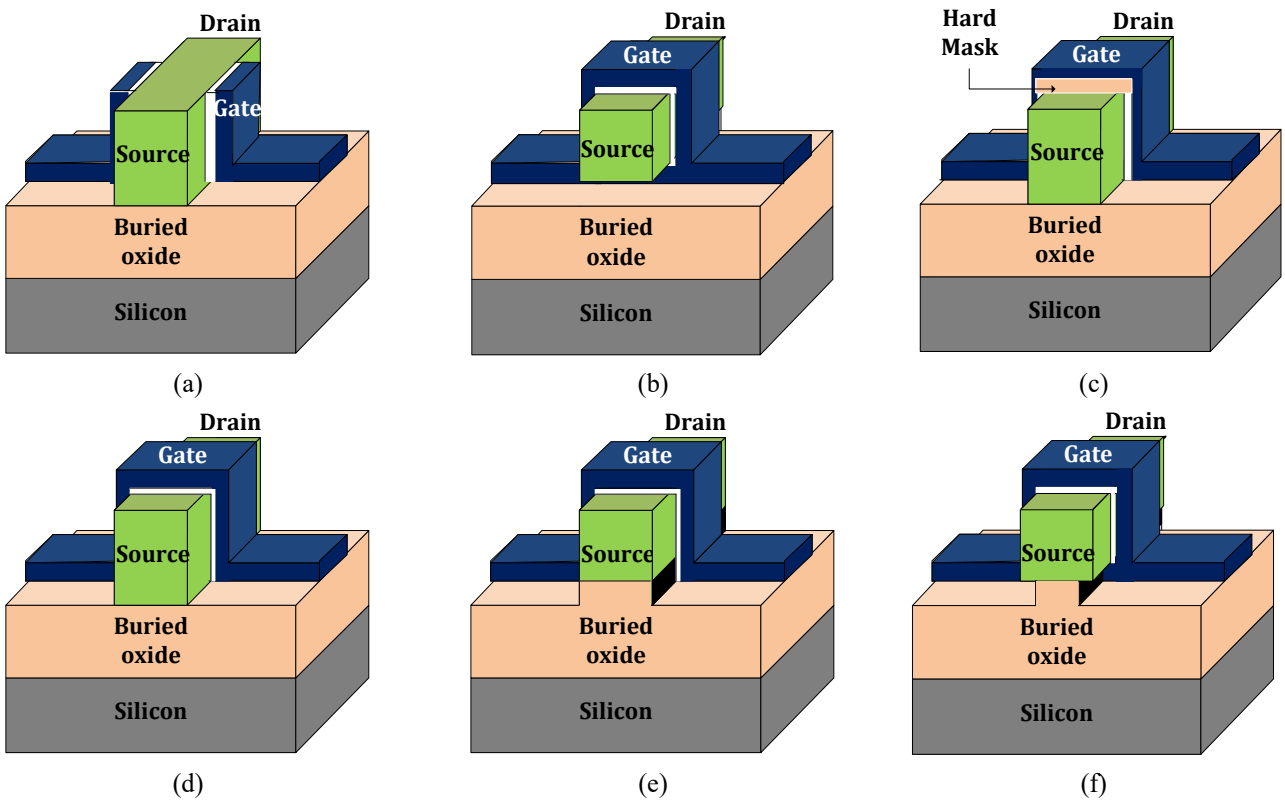

Fig. 1. Different types of MG MOSFETs (a) DG MOSFET, (b) gate-all-around MOSFET, (c) finFET, (d) tri-gate MOSFET, (e) Π-gate MOSFET, (f) Ω-gate MOSFET

barrier lowering (DIBL). These effects cause the V_{th} to decrease upon increasing V_{ds} and also degrades subthreshold slope (SS). Improvement of SCEs by using double-gate architecture was predicted in 1984, which put forward the concept of double-gate (DG) MOSFET [12]. The DG MOSFET is being studied as a key component for future ICs due to its numerous advantages such as excellent gate controllability and improvements in V_{th} roll-off, off-state leakage current and channel length modulation (CLM) effects. The undoped body makes the device immune to RDF, leading to a consistency in the V_{th} from device to device [8]. Due to the undoped body, depletion charge is negligible, which enhances the carrier mobility [13]. The channel inversion takes place throughout the thickness of the body and consequently increases the minority carriers due to which higher current is found [14]. Junction capacitance and mobility degradation are reduced due to which switching speed of the device is improved [13]. Surface roughness scattering due to lower surface electric field is also reduced because of the undoped body [13,14].

All IC designs, digital or analog or mixed-signal, are verified through the use of circuit simulators before being reproduced in real silicon. For any circuit simulator to predict the performance of the ICs based on DG-CMOS technology, it should have accurate models to describe the behaviour of the constituting DG MOSFETs. The device model is a representation of characteristics or conditions in the device in the form of (a) an equation, (b) an equivalent circuit, and (c) a table, together with the proper reasoning and assumptions. Primary requirements to use a device in the simulators are electrostatic potential distribution (ϕ) model, V_{th} model, and I_{ds} model. Several such models have been reported so far regarding the modeling of n-type DG MOSFETs [15−45]. A brief review on modeling of DG MOSFETs has been presented in [46,47] but the models for short-channel (nanoscale) regimes have not been considered.

Taur [15] developed a ϕ model for long-channel undoped DG MOSFETs where two transcendental equations had to be solved in order to describe the potential distribution in the channel. The need for solving the two equations was removed in the model given by Lu and Taur [16], and thus provided only one equation for potential distribution which in turns required numerical iteration method to get the solution. Hong *et al.* [17] had proposed the ϕ model for a long-channel lightly doped DG MOSFETs by considering the effects of fixed as well as mobile charge carriers. Taur [15] had also given a V_{th} criterion for long-channel DG MOSFETs in which iterative method was used to calculate the V_{th} which was later improved by Chen *et al.* [18] by proposing a new definition for V_{th}. Based on the models [15, 16], Taur *et al.* [19] had given a I_{ds} model for long-channel DG MOSFETs which had three different equations for subthreshold, linear, and saturation regions. Tsormpatzoglou *et al.* [20] presented the ϕ model for short-channel DG MOSFETs based on the parabolic potential approximation method [48] and also presented a semi-analytical model for subthreshold drain

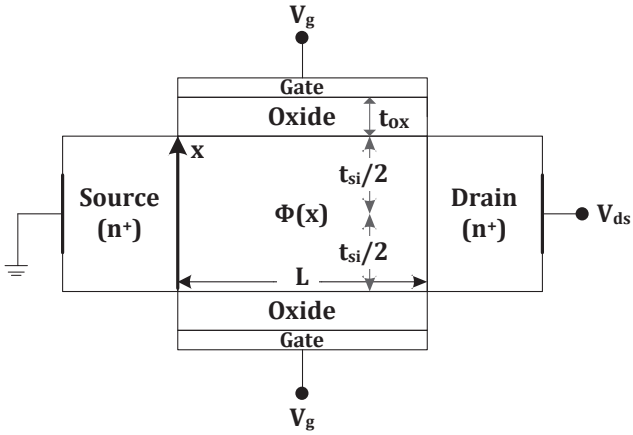

Fig. 2. The cross-sectional view of a long-channel n-type symmetric DG MOSFET along with the geometrical coordinates.

current. Later, the ϕ model [20] was adopted to model the V_{th} in [21] and I_{ds} in [22, 23] for short-channel DG MOSFETs. Recently, Taur and Lin [24] have modified the model [19] by proposing the I_{ds} model for short-channel DG MOSFETs.

In this paper, symmetric n-type DG MOSFET models [15−24] have been reviewed along with their detailed derivations for long and short-channel based on available parameters like ϕ, V_{th}, and I_{ds}. MATLAB code has been presented to demonstrate the semi-analytical modeling given in [20]. At the end, the models [20−23] are adopted to implement n-type DG MOSFET in 30-nm using Verilog-A code [49]. The remaining part of the paper is organized as follows. Section 2 describes the models for long-channel DG MOSFETs in three categories: 1) ϕ models, 2) V_{th} models, and 3) I_{ds} models. Section 3 presents the models for short-channel DG MOSFETs along with MATLAB and Spectre simulations. Section 4 concludes the paper.

II. Models for Long Channel DG MOSFETs

A. Electrostatic Potential Models

The electrostatic potential of a long-channel DG MOSFET $\phi(x)$ is one-dimensional (1-D), which is obtained by solving the 1-D Poisson's equation governing the relationship between electric fields and charges. As shown in Fig. 2, $\phi(x)$ is a function of the distance (x) from the gate towards the channel. The $\phi(x)$ models including Taur's [15], and Lu and Taur's [16] for $L =$ 1μm have been considered for the derivation and analysis of V_{th} and I_{ds} models necessary for designing the complete device model for DG MOSFETs.

1) Taur's Model [15]:

The $\phi(x)$ model for an undoped n-type DG MOSFET is derived by considering only the mobile charge density. This is a core model for $L =$1 μm regime obtained by solving the 1-D Poisson's equation under gradual channel approximation (GCA) [50] assuming Boltzmann statistics for mobile charges. The GCA assumes that variation in lateral electric field much less than the variation in the vertical electric field (along x) so that the 2-D Poisson's equation reduces to 1-D [51]. Finally, the $\phi(x)$ model is expressed as:

$$\phi(x) = \phi_0 - 2V_T \ln\left[\cos\left(\sqrt{\frac{qn_i}{2\epsilon_{si}V_T}}\, e^{\frac{\phi_0}{2V_T}} x\right)\right] \tag{1}$$

where $\phi_0 \equiv \phi(x=0)$, V_T is the thermal voltage, n_i is the intrinsic charge density, and ε_{si} is the dielectric permittivity of silicon. $\phi(x)$ is also defined as the amount of band bending or position of intrinsic potential at x [51]. A similar form of solution (1) was earlier given by Hauser and Littlejohn [52]. Derivation of the model (1) is as follows.

The 1-D Poisson's equation for the silicon region considering only mobile charge density is expressed as:

$$\frac{d^2\phi(x)}{dx^2} = \frac{q}{\varepsilon_{si}} n_i e^{\frac{q\phi(x)}{k_bT}}, \tag{2}$$

where q is the elementary charge, k_b is the Boltzmann constant, and T is the temperature. By interpreting in terms of $d\phi$ and integrating both sides, (2) can be rewritten as:

$$\int_0^{\frac{d\phi}{dx}} \left(\frac{d\phi}{dx}\right) d\left(\frac{d\phi}{dx}\right) = \int_{\phi_0}^{\phi(x)} \frac{q}{\varepsilon_{si}} n_i e^{\frac{q\phi}{k_bT}} d\phi\,. \tag{3}$$

On solving (3):

$$\left(\frac{d\phi}{dx}\right) = \sqrt{\frac{2k_bTn_i}{\varepsilon_{si}}\left(e^{\frac{q\phi(x)}{k_bT}} - e^{\frac{q\phi_0}{k_bT}}\right)}\,. \tag{4}$$

Integrating both sides of (4):

$$\int_{\phi_0}^{\phi(x)} \frac{d\phi}{\sqrt{e^{\frac{q\phi(x)}{k_bT}} - e^{\frac{q\phi_0}{k_bT}}}} = \sqrt{\frac{2k_bTn_i}{\varepsilon_{si}}} \int_0^x dx\,. \tag{5}$$

Considering $e^{\frac{q\phi(x)}{k_bT}} - e^{\frac{q\phi_0}{k_bT}} = t$ will imply:

$$e^{\frac{q\phi(x)}{k_bT}} = t + e^{\frac{q\phi_0}{k_bT}}\,. \tag{6}$$

Differentiaing (6) with respect to ϕ:

$$\frac{d}{d\phi} e^{\frac{q\phi}{k_bT}} = \frac{dt}{d\phi} = \frac{q}{k_bT} e^{\frac{q\phi}{k_bT}}\,. \tag{7}$$

Rearranging the terms of (7):

$$d\phi = \frac{k_bT}{q} e^{\frac{-q\phi}{k_bT}} dt = \frac{k_bT}{q} \frac{dt}{\left(t + e^{\frac{q\phi_0}{k_bT}}\right)}. \tag{8}$$

Substituiting (8) and (6) in (5) will yield:

$$\int_0^t \frac{dt}{\sqrt{t}\left(t + e^{\frac{q\phi_0}{k_bT}}\right)} = \sqrt{\frac{2q^2n_i}{\varepsilon_{si}k_bT}} \int_0^x dx. \tag{9}$$

Considering $\sqrt{t} = z$ in (9) and substituting $dt = 2zdz$ in (9) will imply:

$$\int \frac{2dz}{\left(z^2+e^{\frac{q\phi_0}{k_bT}}\right)} = \sqrt{\frac{2q^2n_i}{\varepsilon_{si}k_bT}}x. \tag{10}$$

$$\frac{2}{e^{\frac{q\phi_0}{2k_bT}}}\tan^{-1}\left(\frac{z}{e^{\frac{q\phi_0}{2k_bT}}}\right) = \sqrt{\frac{2q^2n_i}{\varepsilon_{si}k_bT}}x. \tag{11}$$

$$z = e^{\frac{q\phi_0}{2k_bT}}\tan\left(\sqrt{\frac{q^2n_i}{2\varepsilon_{si}k_bT}}e^{\frac{q\phi_0}{2k_bT}}x\right). \tag{12}$$

$$t = e^{\frac{q\phi_0}{k_bT}}\tan^2\left(\sqrt{\frac{q^2n_i}{2\varepsilon_{si}k_bT}}e^{\frac{q\phi_0}{2k_bT}}x\right). \tag{13}$$

$$e^{\frac{q\phi(x)}{k_bT}} - e^{\frac{q\phi_0}{k_bT}} = e^{\frac{q\phi_0}{k_bT}}\tan^2\left(\sqrt{\frac{q^2n_i}{2\varepsilon_{si}k_bT}}e^{\frac{q\phi_0}{2k_bT}}x\right). \tag{14}$$

$$e^{\frac{q\phi(x)}{k_bT}} = e^{\frac{q\phi_0}{k_bT}}\left[1+\tan^2\left(\sqrt{\frac{q^2n_i}{2\varepsilon_{si}k_bT}}e^{\frac{q\phi_0}{2k_bT}}x\right)\right]. \tag{15}$$

Rearranging terms of (15) :

$$e^{\frac{q(\phi(x)-\phi_0)}{k_bT}} = \sec^2\left(\sqrt{\frac{q^2n_i}{2\varepsilon_{si}k_bT}}e^{\frac{q\phi_0}{2k_bT}}x\right). \tag{16}$$

$$\frac{q(\phi(x)-\phi_0)}{k_bT} = 2\ln\left(\sec\left[\sqrt{\frac{q^2n_i}{2\varepsilon_{si}k_bT}}e^{\frac{q\phi_0}{2k_bT}}x\right]\right). \tag{17}$$

$$\phi(x) = \phi_0 - \frac{2k_bT}{q}\ln\left[\cos\left(\sqrt{\frac{q^2n_i}{2\varepsilon_{si}k_bT}}e^{\frac{q\phi_0}{2k_bT}}x\right)\right]. \tag{18}$$

Since, $\frac{k_bT}{q} = V_T$ so substituting V_T will finally give the $\phi(x)$ model (1).

2) Lu and Taur Model [16]:

This model extended the model [15] by considering quasi-Fermi potential (ϕ_F) in (1). ϕ_F is the potential difference between electron and hole quasi-Fermi levels along the channel $\phi_F = \varphi_{Fn} - \varphi_{Fp}$. In short, ϕ_F is the voltage drop in the channel whose value ranges from $\phi_F = 0$ at source to V_{ds} at the drain. Considering this ϕ_F in equation (2), the 1-D Poisson's equation is expressed as:

$$\frac{d^2\phi(x)}{dx^2} = \frac{q}{\varepsilon_{si}}n_i e^{\frac{q(\phi(x)-\phi_F)}{k_bT}}. \tag{19}$$

Inclusion of the ϕ_F will transform the model (18) as:

$$\phi(x) - \phi_F = \phi_0 - \phi_F - \frac{2k_bT}{q}\ln\left[\cos\left(\sqrt{\frac{q^2n_i}{2\varepsilon_{si}k_bT}}e^{\frac{q(\phi_0-\phi_F)}{2k_bT}}x\right)\right]. \tag{20}$$

A parameter β has been introduced, which is a function of ϕ_F but independent of x [53].

$$\beta = \frac{t_{si}}{2}\sqrt{\frac{q^2n_i}{2\varepsilon_{si}k_bT}}e^{\frac{q(\phi_0-\phi_F)}{2k_bT}}. \tag{21}$$

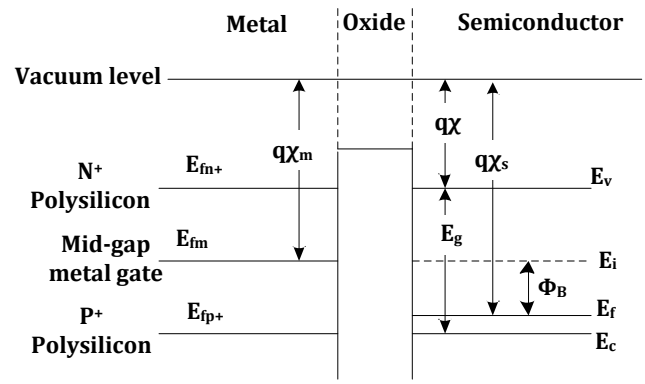

Fig. 3. Fermi-energy levels (E_{fn+}, E_{fp+}, and E_{fm}) of n^+, p^+ polysilicon, and mid-gap metal gate. E_g is the energy band-gap of semiconductor. χ is the electron-affinity of the semiconductor. χ_m and χ_s are the work-functions of mid-gap metal gate and semiconductor, respectively.

Rearranging the terms in (21):

$$\phi_0 - \phi_F = \frac{2k_bT}{q}\ln\left[\frac{2\beta}{t_{si}}\sqrt{\frac{2\varepsilon_{si}k_bT}{q^2n_i}}\right]. \tag{22}$$

On substituting (22) in (20) will yield:

$$\phi(x) = \phi_F - \frac{2k_bT}{q}\ln\left[\frac{t_{si}}{2\beta}\sqrt{\frac{q^2n_i}{2\varepsilon_{si}k_bT}}\cos\left(\frac{2\beta}{t_{si}}x\right)\right]. \tag{23}$$

The surface potential at $x = t_{si}/2$ [Fig. 2] is expressed as:

$$\phi_s \equiv \phi\left(x = \frac{t_{si}}{2}\right) = \phi_F - \frac{2k_bT}{q}\ln\left[\frac{t_{si}}{2\beta}\sqrt{\frac{q^2n_i}{2\varepsilon_{si}k_bT}}\cos\left(\frac{2\beta}{t_{si}}x\right)\right]. \tag{24}$$

Equation (23) is the $\phi(x)$ model given by Lu and Taur which has been taken by many research groups [22−23], [33−34] to model the short-channel DG MOSFET characteristics. Applying boundary condition at silicon-oxide interface:

$$\varepsilon_{ox}\frac{V_g-\Delta\chi_{ms}-\phi_s}{t_{ox}} = \varepsilon_{si}\left.\frac{d\phi}{dx}\right|_{x=\frac{t_{si}}{2}}, \tag{25}$$

where V_g is the applied gate voltage and $\Delta\chi_{ms}$ is the work-function difference between the gates and the silicon as shown in Fig. 3. In case of undoped body $\Delta\chi_{ms} = 0$ for mid-gap metal gate, $-E_g/2q$ for n^+ polysilicon, and $E_g/2q$ for p^+ polysilicon. Differentiating (23) with respect to x:

$$\frac{d\phi}{dx} = \frac{-2V_T\frac{t_{si}}{2\beta}\sqrt{\frac{q^2n_i}{2\varepsilon_{si}k_bT}}\left[-\sin\frac{2\beta}{t_{si}}x\right]\frac{2\beta}{t_{si}}}{\frac{t_{si}}{2\beta}\sqrt{\frac{q^2n_i}{2\varepsilon_{si}k_bT}}\cos\frac{2\beta}{t_{si}}x} = 2V_T\frac{2\beta}{t_{si}}\tan\left(\frac{2\beta}{t_{si}}x\right).$$

$$\left.\frac{d\phi}{dx}\right|_{x=\frac{t_{si}}{2}} = 2V_T\frac{2\beta}{t_{si}}\tan\beta. \tag{26}$$

Substituting (24) and (26) in (25):

$$\frac{V_g-\Delta\chi_{ms}-\phi_F}{2V_T}-\ln\left[\frac{2}{t_{si}}\sqrt{\frac{2\varepsilon_{si}k_bT}{q^2n_i}}\right]= \ln\beta-\ln\cos\beta+2r\beta\tan\beta, \quad (27)$$

with $r=\frac{\varepsilon_{si}t_{ox}}{\varepsilon_{ox}t_{si}}$. The value of β has to be calculated from (27) using numerical iterations like Newton-Raphson method [54]. Numerical iteration and algorithms increase the computation time. Fast and efficient method has to be adopted to make the model suitable for circuit simulation. Yu *et al*. [25] developed a computation method which eliminated the need for numerical iterations.

3) Hong et al. [17]:

The $\phi(x)$ models of DG MOSFETs developed in [15, 16] are valid for the undoped silicon body. The work has been extended by Hong *et al.* [17] by proposed the $\phi(x)$ model for the lightly doped silicon body with spatially varying doping profiles. The $\phi(x)$ model derived through solving the 1-D Poisson's equation considering both the fixed and mobile charge density.

$$\frac{d^2\phi(x)}{dx^2}=\frac{qn_i^2}{\varepsilon_{si}N_{si}}e^{\frac{q(\phi(x)-\phi_F)}{k_bT}}+\frac{qN_{si}(x)}{\varepsilon_{si}}, \quad (28)$$

where $N_{si}(x)$ is the spatially varying doping distribution in the silicon body (can be continuous or discrete). Consideration of fixed and mobile charge density in a lightly-doped silicon body is required from the accuracy point of view [31,32]. Because, the effect of mobile charge density cannot neglected in the above subthreshold regime [33] and its inclusion in Poisson's equation enhances the model accuracy [55]. Substituting $\frac{qN_{si}(x)}{\varepsilon_{si}}=\frac{d^2g(x)}{dx^2}$, (28) can be written as:

$$\phi(x)=\frac{k_bT}{q}Z(x)+\phi_F+g(x). \quad (29)$$

Differentiating (29) twice with respect to x:

$$\frac{d^2\phi(x)}{dx^2}=\frac{k_bT}{q}\frac{d^2Z(x)}{dx^2}+\frac{d^2g(x)}{dx^2}. \quad (30)$$

Substituting (30) in (28) will yield:

$$\frac{k_bT}{q}\frac{d^2Z(x)}{dx^2}+\frac{d^2g(x)}{dx^2}=\frac{qn_i^2}{\varepsilon_{si}N_{si}}e^{\frac{q}{k_bT}\left(\frac{k_bT}{q}Z(x)+g(x)\right)}+\frac{qN_{si}(x)}{\varepsilon_{si}},$$

which on solving will yield:

$$\frac{d^2Z(x)}{dx^2}=\frac{q^2n_i^2}{k_bT\varepsilon_{si}}e^{Z(x)}\frac{e^{\frac{q}{k_bT}g(x)}}{N_{si}}. \quad (31)$$

Substituting $Exp\left[\frac{q}{k_bT}g(x)\right]/N_{si}=f(x)$ and $\frac{q^2n_i^2}{k_bT\varepsilon_{si}}=\xi$, (31) is re-written as:

$$\frac{d^2Z(x)}{dx^2}=\xi e^{Z(x)}f(x). \quad (32)$$

The terms ξ and $f(x)$ in (32) contain the effect of nonlinear coupling between the mobile and fixed charge densities. Presence of the $f(x)$ makes this modeling scheme unique from the exiting $\phi(x)$ model [56] for the DG MOSFET. In order to derive the analytical solution for $\phi(x)$, the (32) (in Cartesian coordinate) is transformed into the cylindrical coordinate.

$$\frac{d^2Z_C(\tau)}{d\tau^2}+\frac{1}{\tau}\frac{dZ_c(\tau)}{d\tau}=\xi e^{Z_c(\tau)}F(\tau), \quad (33)$$

where $Z_c(\tau)=Z(x)-2$, $\ln\tau=x$, and $F(\tau)=f(ln\,\tau)$. In order to solve (32), two new variables are introduced: $\beta=\tau\frac{dZ_C}{d\tau}$ and $\eta=\tau^2F(\tau)e^{Z_c(\tau)}$. Differentiating β with respect to τ will yield:

$$\frac{d\beta}{d\tau}=\frac{dZ_C(\tau)}{d\tau}+\tau\frac{d^2Z_C(\tau)}{d\tau^2}. \quad (34)$$

Substituting $\frac{d^2Z_C(\tau)}{d\tau^2}$ from (34) in (33):

$$\frac{d\beta}{d\tau}=\tau\xi e^{Z_c(\tau)}F(\tau). \quad (35)$$

Differentiating η with respect to τ will yield:

$$\frac{d\eta}{d\tau}=2\tau F(\tau)e^{Z_C(\tau)}+\tau^2F'(\tau)e^{Z_C(\tau)}+\tau^2F(\tau)e^{Z_C(\tau)}\frac{dZ_C}{d\tau}. \quad (36)$$

Substituting $\beta=\tau\frac{dZ_C}{d\tau}$ and rearranging the terms of (36):

$$\tau e^{Z_c(\tau)}F(\tau)=\frac{d\eta}{d\tau}\frac{1}{\left[2+\tau\frac{F'(\tau)}{F(\tau)}+\beta\right]}. \quad (37)$$

On substituting (37) in (35) will further transform the (33) to:

$$d\beta[\beta+p(\tau)]=\xi d\eta, \quad (38)$$

where $p(\tau)=2+\tau\frac{F'(\tau)}{F(\tau)}$ is the spatial function related to the doping profile, i.e. whether continuous or discrete doping. Equation (38) is integrated to obtain:

$$\frac{\beta^2}{2}+p(\tau)\beta-h=\xi\eta, \quad (39)$$

where $h=-\xi\eta_0-2p+2$ is an integration constant to be determined from boundary conditions. Substituting $\beta=\tau\frac{dZ_C}{d\tau}$ and $\eta=\tau^2F(\tau)e^{Z_c(\tau)}$ in (39) and using (32) will yield :

$$\frac{d^2Z_C(\tau)}{d\tau^2}-\frac{[p(\tau)-1]}{\tau}\frac{dZ_c(\tau)}{d\tau}-\frac{1}{2}\left(\frac{dZ_c(\tau)}{d\tau}\right)^2+\frac{h}{\tau^2}=0. \quad (40)$$

On solving (40), the general solution of 1-D Poisson's equation can be readily obtained as:

$$Z_C=-p\ln\tau+A-2\ln\left|\cos\left(\frac{1}{2}\sqrt{-(p-2)^2-2h}\ln\tau-B\sqrt{-(p-2)^2-2h}\right)\right|, \quad (41)$$

where A and B are the integration constants. Here the $\beta(\tau)$ is approximated as:

$$\beta(\tau)=-p+\sqrt{-(p-2)^2-2h} \quad (42)$$

$$\tan\left\{\frac{1}{2}\sqrt{-(p-2)^2-2h}\left(\ln\tau-\frac{t_{si}}{2}\right)+\tan^{-1}\left[\frac{\beta_s+p}{\sqrt{-(p-2)^2-2h}}\right]\right\},$$

where β_s is value of $\beta(\tau)$ at the surface $\left(\tau=e^{\frac{t_{si}}{2}}\right)$ and can be approximated from the relation:

$$\frac{\beta_s^2}{2}-\frac{\beta_0^2}{2}+M=\xi(\eta_s-\eta_0)\,, \tag{43}$$

where β_0 is value of $\beta(\tau)$ at the center of the silicon body $(\tau=1)$. For the symmetric DG MOSFETs, $\beta_0=dZ_C/d\tau|_{\tau=1}=-2$ is considered. $M=\int_1^{e^{\frac{t_{si}}{2}}}\left[p(\tau)\frac{d\beta}{d\tau}\right]d\tau$ is an integral to be solved. η_0 is calculated from the relation:

$$\eta_0=\frac{c(\beta_s+2)}{\xi\left[1+\left(\frac{\beta_s+2}{\beta_c+2}\right)\right]}\,, \tag{44}$$

where β_c is the value of β_s when η_0 reaches its saturation value η_{0sat} whose value is given by: $\beta_c=\frac{\xi\eta_{0sat}}{c-2}$. The parameters c, η_{0sat} are expressed as:

$$c=\frac{\xi\varepsilon_{si}k_bTF(1)}{q\theta_s}\text{, with }\theta_s=\int_0^{\frac{t_{si}}{2}}\frac{qn_i^2}{N_{si}}e^{\frac{q\left(\frac{qN_{si}x^2}{\varepsilon_{si}\ 2}\right)}{k_bT}}dx, \tag{45}$$
$$\eta_{0sat}=1\times F(1)\times e^{Z_{Csat}}$$
$$\text{with } Z_{Csat}\approx 2\ln\left(\frac{N_{si}}{n_i}\right)-\ln[1-e^{-2\alpha}]-\alpha+1.6$$
$$\text{where } \alpha=\frac{q^2N_{si}t_{si}^2}{8\varepsilon_{si}k_bT}.$$

The potential distribution characteristics obtained from the model (41) is able show the variation of electrostatic potential with respect to the V_g from weak to strong inversion regime.

B. Threshold Voltage Models

The V_{th} of conventional bulk MOSFET is defined as the V_g at which the minimum surface potential value $\phi_{s,min}$ reaches twice the bulk potential ϕ_B [51]. ϕ_B is the potential difference between the Fermi-level (E_f) and the intrinsic level (E_i) of the semiconductor [Fig. 3]. The ϕ_B definition of V_{th} does not work for DG MOSFETs, where the doping concentration is $N_{si}\leq 10^{16}$ cm^{-3}[18,33].

1) Taur's Model [15]:

The threshold criterion for long-channel DG MOSFETs given by Taur [15] used iterative method to calculate the V_{th} by extrapolating the linear dependency of inversion charge sheet density Q_{inv} with V_g using the relation: $Q_{inv}=2C_{ox}(V_g-\Delta\chi_{ms}-\phi_s)$. Where $\phi_s\equiv\phi(x=t_{si}/2)$ is the surface potential. The threshold condition is given by: $V_{th}=\Delta\chi_{ms}-\phi_s$. The detailed derivation of the model is as follows.

The effective gate voltage at the silicon-oxide interface is expressed as:

$$V_{gt}=V_g-\Delta\chi_{ms}-\phi_s\,. \tag{46}$$

Applying boundary condition at the silicon-oxide interface:

$$\varepsilon_{ox}\frac{V_g-\Delta\chi_{ms}-\phi_s}{t_{ox}}=\varepsilon_{si}\left.\frac{d\phi}{dx}\right|_{x=t_{si}/2}\,. \tag{47}$$

Substituting $\left.\frac{d\phi}{dx}\right|_{x=t_{si}/2}$ from (4) in (47):

$$\varepsilon_{ox}\frac{V_g-\Delta\chi_{ms}-\phi_s}{t_{ox}}=\sqrt{2\varepsilon_{si}k_bTn_i\left(e^{\frac{q\phi_s}{k_bT}}-e^{\frac{q\phi_0}{k_bT}}\right)}\,. \tag{48}$$

ϕ_s is increased with increase in V_g, whereas the center potential ϕ_0 attains a constant value. For greater value of V_g (more than threshold), the term ϕ_0 in (48) can be neglected which will imply:

$$\varepsilon_{ox}\frac{V_g-\Delta\chi_{ms}-\phi_s}{t_{ox}}=\sqrt{2\varepsilon_{si}k_bTn_i}e^{\frac{q\phi_s}{2k_bT}}\,. \tag{49}$$

Since $\frac{\varepsilon_{ox}}{t_{ox}}=C_{ox}$, so (49) can be re-written as:

$$C_{ox}(V_g-\Delta\chi_{ms}-\phi_s)=\sqrt{2\varepsilon_{si}k_bTn_i}e^{\frac{q\phi_s}{2k_bT}}\,. \tag{50}$$

Substituting $V_g-\Delta\chi_{ms}-\phi_s=V_{gt}$ in (50) and on solving:

$$\phi_s=\frac{2k_bT}{q}\ln\left[\frac{C_{ox}V_{gt}}{\sqrt{2\varepsilon_{si}k_bTn_i}}\right] \tag{51}$$

Since the threshold condition is given by:

$$V_{th}=\Delta\chi_{ms}+\phi_s \tag{52}$$

Substituting ϕ_s from (51):

$$V_{th}=\Delta\chi_{ms}+\frac{2k_bT}{q}\ln\left[\frac{C_{ox}V_{gt}}{\sqrt{2\varepsilon_{si}k_bTn_i}}\right]. \tag{53}$$

The V_{th} model (53) is a transcendental equation which needs to be solved numerically. The ϕ_s increases with the increase in V_g, and the ϕ_0 asymptotically approach a constant value: $\phi_{0,max}=(k_bT/q)\ln[2\pi^2\varepsilon_{si}k_bT/q^2n_it_{si}]$ with slope $=2C_{ox}$. Volume inversion takes place in the subthreshold region and volume inversion, no band bending occurs.

2) Chen et al. [18]:

Chen *et al.* [18] defined the V_{th} as the required V_g at which the inversion charge sheet density Q_{inv} at minimum potential position (virtual cathode) reaches a value Q_{th} which is sufficient enough to turn on the device [33]. Fig. 4 shows the threshold condition defined for DG MOSFETs. The effective conductive path is located at $x=t_{si}/4$ from the top and bottom surfaces. The V_{th} model for the long-channel DG MOSFET is:

$$V_{th}=\Delta\chi_{ms}+V_T\ln\left(\frac{Q_{th}}{n_it_{si}}\right). \tag{54}$$

The value of Q_{th} is determined as 3.2×10^{10} cm^{-2}. Similar expression (54) has been deduced by Hamid *et al.* [33].

C. Drain-Current Models

The I_{ds} models can be broadly classified into potential based and charge based models. In the potential based models, the I_{ds} is expressed through indirect function of applied V_g and V_{ds}. Whereas, in charge based models, the I_{ds} is expressed in terms of terminal charges, as an implicit function of V_g and V_{ds}.

1) Taur et al. [19]:

The model [19] is a surface potential based model in which I_{ds} is expressed in terms of applied bias. The pre-requisite for the model is electrostatic potential models [15,16]. The drain current expression is:

$$I_{ds} = \mu \frac{W}{L} \frac{4\varepsilon_{si}}{t_{si}} \left(\frac{2k_bT}{q}\right)^2 [g_r(\beta_s) - g_r(\beta_d)] \tag{55}$$

where $g_r(\beta) = \left[\beta \tan\beta - \frac{\beta^2}{2} + 2r\beta^2 \tan^2\beta\right]$ with β_s and β_d are the values of β at the source and drain ends respectively. Three different equations have been used for subthreshold, linear, and saturation regions by approximating the values of β. The I_{ds} model is based on Pau-Sah's double integral, which is based on GCA [50]. The GCA is valid for most regions of MOSFET operation except beyond the pinch-off point. Charge-sheet model [57] is then introduced to obtain the implicit equations for I_{ds} model. The detailed derivation is as follows.

For the long channel devices, the total electron current density is the sum of the drift and diffusion current density [51,58]:

$$J_n(x,y) = qn(x,y)\mu_n E_x + qD_n \frac{dn(x,y)}{dx}, \tag{56}$$

where $E_x = -d\phi(x)/dx$ is the vertical electric field in the silicon body and $D_n = \mu_n V_T$ is the electron diffusion coefficient [51]. Substituting E_x and D_n in (56):

$$J_n(x,y) = -qn(x,y)\mu_n \left[\frac{d\phi(x)}{dx} - \frac{k_bT}{qn(x,y)} \frac{dn(x,y)}{dx}\right], \tag{57}$$

where $n(x,y) = n_i e^{\frac{q(\phi(x)-\phi_F)}{k_bT}}$ is the electron density. On rearranging the terms of $n(x,y)$:

$\frac{n(x,y)}{n_i} = e^{\frac{q(\phi(x)-\phi_F)}{k_bT}}$, which on solving will yield:

$$\phi(x) - \frac{k_bT}{q} \ln\left[\frac{n(x,y)}{n_i}\right] = \phi_F . \tag{58}$$

Differentiating (58) with respect to x

$$\frac{d\phi(x)}{dx} - \frac{k_bT}{qn(x,y)} \frac{dn(x,y)}{dx} = \frac{d\phi_F}{dx} . \tag{59}$$

Substituting (59) in (57):

$$J_n(x,y) = -q\mu_n n(x,y) \frac{d\phi_F}{dy} . \tag{60}$$

The I_{ds} is expressed in terms of $J_n(x,y)$ [51] as:

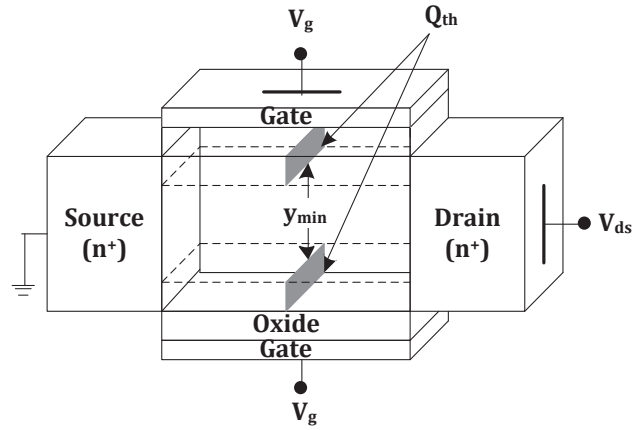

Fig. 4. Schematic showing the inversion charge sheet density at threshold condition. (Dashed lines represent the effective conductive path).

$$I_{ds}(y) = 2W \int_0^{\frac{t_{si}}{2}} -q\mu_n n(x,y) \frac{d\phi_F}{dy} dx . \tag{61}$$

Equation (61) can be written as:

$$I_{ds}(y) = 2W\mu_n(-Q_{inv}(y)) \frac{d\phi_F}{dy}, \tag{62}$$

where $-Q_{inv}(y) = \int_0^{\frac{t_{si}}{2}} qn(x,y)dx$ is the inversion charge sheet density. Integrating the both sides of (62) :

$$\int_0^L I_{ds}(y)dy = \mu_n 2W \int_0^{V_{ds}} (-Q_{inv}(y))d\phi_F ,$$

$$I_{ds} = \mu_n \left(\frac{2W}{L}\right) \int_0^{V_{ds}} (-Q_{inv}(y))d\phi_F . \tag{63}$$

Rearranging the terms of (1) will yield:

$$e^{\frac{\phi(x)-\phi_F}{V_T}} = \left(\frac{2\beta}{t_{si}}\right)^2 \left(\frac{2\varepsilon_{si}k_bT}{q^2 n_i}\right) \sec^2\left(\frac{2\beta}{t_{si}}x\right) . \tag{64}$$

On substituting $n(x,y) = n_i e^{\frac{q(\phi(x)-\phi_F)}{k_bT}}$ in the expression $-Q_{inv}(y) = \int_0^{\frac{t_{si}}{2}} qn(x,y)dx$ will yield:

$$-Q_{inv}(y) = q \int_0^{\frac{t_{si}}{2}} n_i e^{\frac{\phi(x)-\phi_F}{V_T}} dx . \tag{65}$$

Substituting (64) in (65):

$$-Q_{inv}(y) = q \int_0^{\frac{t_{si}}{2}} n_i \left(\frac{2\beta}{t_{si}}\right)^2 \left(\frac{2\varepsilon_{si}k_bT}{q^2 n_i}\right) \sec^2\left(\frac{2\beta}{t_{si}}x\right) dx . \tag{66}$$

On solving (66):

$$\begin{aligned} -Q_{inv}(y) &= qn_i \left(\frac{2\beta}{t_{si}}\right)^2 \left(\frac{2\varepsilon_{si}k_bT}{q^2 n_i}\right) \left(\frac{t_{si}}{2\beta}\right) \tan\left(\frac{2\beta}{t_{si}}x\right)\Bigg|_{x=0}^{\frac{t_{si}}{2}} \\ &= qn_i \left(\frac{2\beta}{t_{si}}\right) \left(\frac{2\varepsilon_{si}k_bT}{q^2 n_i}\right) \tan(\beta) \\ &= \frac{4\varepsilon_{si}k_bT}{qt_{si}} \beta \tan\beta . \end{aligned} \tag{67}$$

$$I_{ds} = \mu_n \left(\frac{2W}{L}\right) \int_0^{V_{ds}} \frac{4\varepsilon_{si}k_bT}{qt_{si}} \beta \tan\beta \left[-2V_T \left\{\frac{1}{\beta} + (2r+1)\tan\beta + 2r\beta \sec^2\beta\right\}\right] d\beta. \tag{70}$$

Referring to the expression (27):

$$\frac{V_g-\Delta\chi_{ms}-\phi_F}{2V_T} - ln\left[\frac{2}{t_{si}}\sqrt{\frac{2\varepsilon_{si}k_bT}{q^2n_i}}\right] = \ln\beta - \ln\cos\beta + 2r\beta\tan\beta. \quad (68)$$

Differentiating (68) with respect to β :

$$d\phi_F = -2V_T\left[\frac{1}{\beta} + (2r+1)\tan\beta \ \ +2r\beta\sec^2\beta\right]. \quad (69)$$

Substituting (67) and (69) in (63) will yield (shown at the bottom of the previous page):

Changing the integral limit of (70) from $\int_0^{V_{ds}} d\beta$ to $\int_{\beta_s}^{\beta_d} d\beta$:

$$I_{ds} = -\mu_n\left(\frac{2W}{L}\right)\left(\frac{2\varepsilon_{si}}{t_{si}}\right)\left(\frac{2k_bT}{q}\right)^2$$

$$\int_{\beta_s}^{\beta_d}[\tan\beta + (2r+1)\beta\tan^2\beta + 2r\beta^2\tan\beta\sec^2\beta]d\beta$$

$$= \mu_n\left(\frac{2W}{L}\right)\left(\frac{2\varepsilon_{si}}{t_{si}}\right)\left(\frac{2k_bT}{q}\right)^2\left[\int_{\beta_d}^{\beta_s}\tan\beta d\beta + (2r+1)\int_{\beta_d}^{\beta_s}\beta\tan^2\beta d\beta + 2r\int_{\beta_d}^{\beta_s}\beta^2\tan\beta\sec^2\beta\, d\beta\right]. \quad (71)$$

There are three integrals to be solved in (71) which are: $\int\tan\beta d\beta$, $\int\beta\tan^2\beta\, d\beta$, and $\beta^2\tan\beta\sec^2\beta\, d\beta$. Solution of the integrals are expressed as:

$$\int\tan\beta d\beta = \ln\sec\beta\ . \quad (72)$$

$$\int\beta\tan^2\beta\, d\beta = \int\beta(\sec^2\beta - 1)d\beta\ , = \int\beta\sec^2\beta\, d\beta - \int\beta d\beta = \beta\tan\beta - \ln\sec\beta - \frac{\beta^2}{2}. \quad (73)$$

$$\int\beta^2\tan\beta\sec^2\beta\, d\beta = \beta^2\tan\beta\int\sec^2\beta\, d\beta - \int\left\{\frac{d}{d\beta}\beta^2\tan\beta\int\sec^2\beta\, d\beta\right\}d\beta = \frac{1}{2}\beta^2\tan^2\beta - \beta\tan\beta + \ln\sec\beta + \frac{\beta^2}{2}. \quad (74)$$

Substituting (72−74) in (71) will yield:

$$I_{ds} = \mu_n\left(\frac{2W}{L}\right)\left(\frac{2\varepsilon_{si}}{t_{si}}\right)\left(\frac{2k_bT}{q}\right)^2\left[\beta\tan\beta - \frac{\beta^2}{2} + r\beta^2\tan^2\beta\right]\Big|_{\beta=\beta_d}^{\beta_s}. \quad (75)$$

Equating the terms: $\ln\beta - \ln\cos\beta + 2r\beta\tan\beta = f_r(\beta)$ [from (68)] and $\beta\tan\beta - \frac{\beta^2}{2} + r\beta^2\tan^2\beta = g_r(\beta)$ [from (55) and (75)]. At source end $\beta = \beta_s$ and $\phi_F = 0$ V. So,

$$f_r(\beta_s) = \frac{V_g-\Delta\chi_{ms}}{2V_T} - \ln\left[\frac{2}{t_{si}}\sqrt{\frac{2\varepsilon_{si}k_bT}{q^2n_i}}\right] = \frac{V_g-\left(\Delta\chi_{ms}+2V_T\ln\left[\frac{2}{t_{si}}\sqrt{\frac{2\varepsilon_{si}k_bT}{q^2n_i}}\right]\right)}{2V_T} = \frac{V_g-V_0}{2V_T}. \quad (76)$$

where $V_0 = \Delta\chi_{ms} + 2V_T\ln\left[\frac{2}{t_{si}}\sqrt{\frac{2\varepsilon_{si}k_bT}{q^2n_i}}\right]$. At drain end, $\beta = \beta_d$ and $\phi_F = V_{ds}$. So,

$$f_r(\beta_d) = \frac{V_g-V_0-V_{ds}}{2V_T}. \quad (77)$$

In the linear region of operation, $f_r(\beta_s) = f_r(\beta_d) \gg 1$ which implies $\beta_s, \beta_d > \frac{\pi}{2}$. So, the term $f_r(\beta)$ in (76) and $g_r(\beta)$ in (77) are reduced to $2r\beta\tan\beta$ and $r\beta^2\tan^2\beta$ respectively. Therefore,

$$f_r(\beta_s) \equiv \beta_s\tan\beta_s = \left(\frac{V_g-V_o}{2V_T}\right)\frac{1}{2r}. \quad (78)$$

Similarly, $f_r(\beta_d) \equiv \beta_d\tan\beta_d = \left(\frac{V_g-V_o-V_{ds}}{2V_T}\right)\frac{1}{2r}$, (79)

and the expression (75) reduces to:

$$I_{ds,LIN} = \mu_n\frac{2W}{L}\frac{2\varepsilon_{si}}{t_{si}}(2V_T)^2[r\beta^2\tan^2\beta]_{\beta_d}^{\beta_s}. \quad (80)$$

On substituting (78) and (79) in (80) :

$$I_{ds,LIN} = \mu_n\frac{2W}{L}\frac{2\varepsilon_{si}}{t_{si}}(2V_T)^2\frac{1}{4r}\left[\left(\frac{V_g-V_o}{2V_T}\right)^2 - \left(\frac{V_g-V_o-V_{ds}}{2V_T}\right)^2\right]$$

$$= \mu_n\frac{W}{L}C_{ox}\left[(V_g-V_o)^2 - (V_g-V_o)^2 - V_{ds}^2 + 2(V_g-V_o)V_{ds}\right]$$

$$= 2\mu_n\frac{W}{L}C_{ox}\left[(V_g-V_{th}) - \frac{V_{ds}}{2}\right]V_{ds}\ , \quad (81)$$

where $V_{th} = V_o + \delta$, δ is the second-order effects. The $I_{ds,LIN}$ (81) is the drain current expression for the linear region. The δ is derived as follows.

Considering $\phi_F = 0$ in (25), the ϕ_s at the source region is expressed as: $\phi_s = -\frac{2k_bT}{q}\ln\left[\frac{t_{si}}{2\beta}\sqrt{\frac{q^2n_i}{2\varepsilon_{si}k_bT}}\cos(\beta)\right]$. Since the threshold condition is given by: $V_{th} = \Delta\chi_{ms} + \phi_s$ [15], the expression of the V_{th} in (81) is written as:

$$V_{th} = \Delta\chi_{ms} - \frac{2k_bT}{q}\ln\left[\frac{t_{si}}{2}\sqrt{\frac{q^2n_i}{2\varepsilon_{si}k_bT}}\right] - \frac{2k_bT}{q}\ln\frac{\cos\beta}{\beta}$$

$$= V_o + \frac{2k_bT}{q}\ln\frac{\beta}{\cos\beta}$$

$$= V_o + \frac{2k_bT}{q}\ln\frac{\beta\sin\beta}{\cos\beta\sin\beta}$$

$$= V_o + \frac{2k_bT}{q}\ln\beta\tan\beta - \frac{2k_bT}{q}\ln\sin\beta\ . \quad (82)$$

In the strong inversion condition, the $\beta \to \frac{\pi}{2}$ which implies the term "$\ln\sin\beta$" in (82) is ≈0. So,

$$V_{th} = V_o + \frac{2k_bT}{q}\ln\beta\tan\beta = V_o + \delta\ , \quad (83)$$

with $\delta = (2k_BT/q)\ln\beta\tan\beta$. Substituting (78) in (83) will yield:

$$\delta = \frac{2k_bT}{q}ln\left[\left(\frac{V_g-V_o}{2V_T}\right)\frac{1}{2r}\right]. \quad (84)$$

Equation (84) is the second-order effect ≈0.05V.

In the saturation region of operation, $\beta_s \approx \pi/2$ and $\beta_d \ll 1$. So, the terms $f_r(\beta_s)$ and $f_r(\beta_d)$ are reduced to $2r\beta_s\tan\beta_s$ and

$\ln \beta_d$ respectively. Therefore,

$$f_r(\beta_s) \equiv r\beta_s \tan \beta_s = \left(\frac{V_g - V_o}{4V_T}\right) \tag{85}$$

and $f_r(\beta_d) \equiv \beta_d = e^{\left(\frac{V_g - V_o - V_{ds}}{2V_T}\right)}$. (86)

The expression (75) reduces to :

$$I_{ds,SAT} = \mu_n \frac{2W}{L}\frac{2\varepsilon_{si}}{t_{si}}(2V_T)^2\left[r\beta_s^2 \tan^2 \beta_s - \frac{\beta_d^2}{2}\right]. \tag{87}$$

Substituting (85) and (86) in (87) will yield:

$$I_{ds,SAT} = \mu_n \frac{2W}{L}\frac{2\varepsilon_{si}}{t_{si}}(2V_T)^2\left[r\left(\frac{V_g - V_o}{4V_T}\right)^2 - \frac{1}{2}e^{\left(\frac{V_g - V_o - V_{ds}}{V_T}\right)}\right]$$

$$= \mu_n \frac{W}{L} C_{ox}\left[\left(V_g - V_o\right)^2 - \frac{8rk_b^2T^2}{q^2}e^{\left(\frac{V_g - V_o - V_{ds}}{V_T}\right)}\right]. \tag{88}$$

Equation (88) is the drain current expression for the saturation region ($I_{ds,SAT}$).

In subthreshold region of operation, $\beta_s, \beta_d \ll 1$. So the terms $f_r(\beta)$ and $g_r(\beta)$ are reduced to $\ln \beta$ and $(\beta/2)$ respectively. On solving (76) for $f_r(\beta) = \ln \beta$ will yield:

$$\ln \beta_s = \frac{V_g - V_o}{2V_T} \equiv \frac{V_g - \Delta\chi_{ms}}{2V_T} - \ln\left[\frac{2}{t_{si}}\sqrt{\frac{2\varepsilon_{si}k_bT}{q^2 n_i}}\right],$$

which implies:

$$\beta_s = \frac{2}{t_{si}}\sqrt{\frac{2\varepsilon_{si}k_bT}{q^2 n_i}}\, e^{\frac{V_g - \Delta\chi_{ms}}{2V_T}}. \tag{89}$$

Similarly,

$$\beta_d = \frac{2}{t_{si}}\sqrt{\frac{2\varepsilon_{si}k_bT}{q^2 n_i}}\, e^{\frac{V_g - \Delta\chi_{ms} - V_{ds}}{2V_T}} \tag{90}$$

Since $g_r(\beta) = \frac{\beta}{2}$, the (75) reduces to:

$$I_{ds,SUB} = \mu_n \frac{2W}{L}\frac{2\varepsilon_{si}}{t_{si}}(2V_T)^2\left[\frac{\beta_s^2}{2} - \frac{\beta_d^2}{2}\right] \tag{91}$$

On substituting (89) and (90) in (91) will finally yield the $I_{ds,SUB}$ model for the subthreshold region.

$$I_{ds,SUB} = \mu_n \frac{W}{L} k_b T n_i t_{si} e^{\frac{V_g - \Delta\chi_{ms}}{V_T}}\left(1 - e^{\frac{-V_{ds}}{V_T}}\right) \tag{92}$$

Combining the $I_{ds,LIN}$ (81), $I_{ds,SAT}$ (88), and $I_{ds,SUB}$ (92) for the different regions namely linear, saturation, and subthreshold, respectively, the complete I_{ds} model is written as:

$$I_{ds} = \begin{cases} \mu \dfrac{W}{L} V_T q n_i t_{si} e^{\frac{V_{gs} - \Delta\chi_{ms}}{V_T}}\left(1 - e^{-\frac{V_{ds}}{V_T}}\right) \\ 2\mu C_{ox}\dfrac{W}{L}\left(V_{gs} - V_{th} - \dfrac{V_{ds}}{2}\right)V_{ds} \\ \mu C_{ox}\dfrac{W}{L}\left[\left(V_{gs} - V_{th}\right) - 8rV_T^2 e^{\frac{V_{gs} - V_0 - V_{ds}}{V_T}}\right] \end{cases} \tag{93}$$

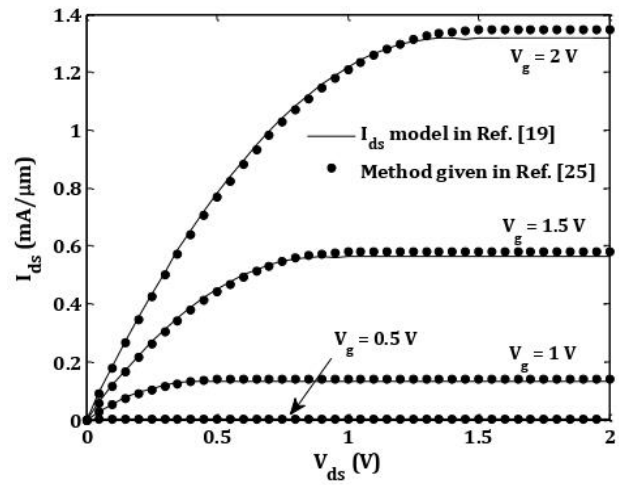

(a)

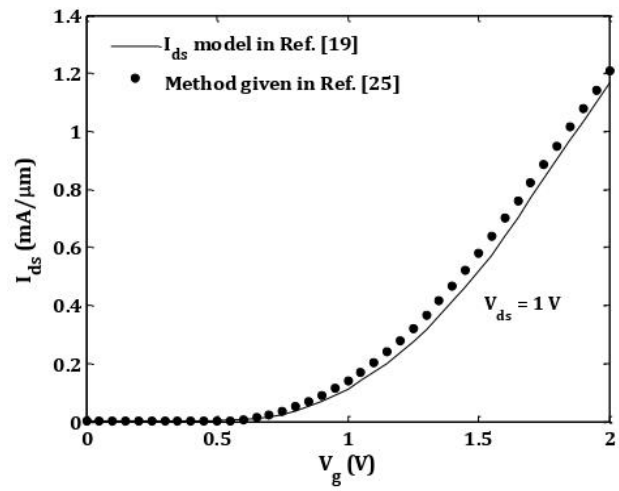

(b)

Fig. 5. Characteristics of a long-channel DG MOSFET with $L = 1$ μm, $W = 1$ μm, $t_{si} = 5$ nm, and $t_{ox} = 1.5$ nm obtained from model (93) in comparison with the results obt ained through using the method given by Yu e*t al.* [25] (a) output characteristics, (b) transfer characteristics.

Equation (93) is the long channel core I_{ds} model for DG MOSFETs which has been subsequently augmented with various physical effects like SCE, quantum mechanical effect, and low and high field transport in order to develop I_{ds} models [22, 23] for short-channel DG MOSFETs. Fig. 5 shows the I_{ds} characteristics obtained from (93) for an undoped DG MOSFET with a mid-gap metal gate, in comparison with the characteristics obtained through solving the β from (27) by the method given by Yu *et al.* [25]. A constant mobility μ_n =300 cm^2/(Vs) [19,25,26] has been considered in numerical simulation. The I_{ds} models in [19, 22−27] are based on assumptions of constant electron mobility in order to validate the results with the simulated data. Constant mobility in the I_{ds} model is a strong assumption [59] since the mobility gets affected by the vertical and horizontal electric field due to the V_g and V_{ds} respectively. The I_{ds} models [28, 29] considered the Caughey-Thomas mobility model [60] while the models in [30,

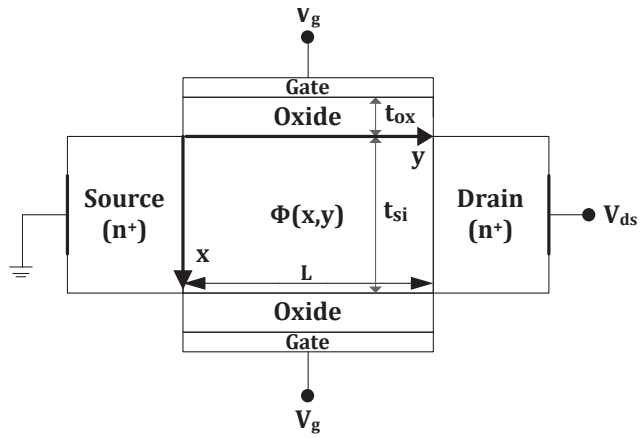

Fig. 6. The cross-sectional view of a short-channel n-type symmetric DG MOSFET along with the geometrical coordinates.

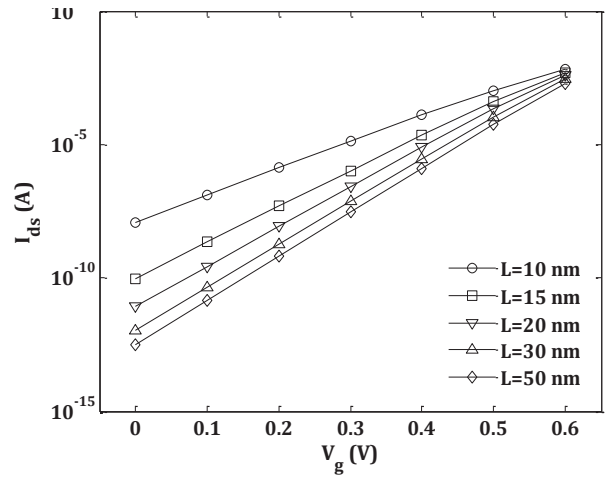

Fig. 7. Transfer characteristics (in semi-logarithmic scale) in the subthreshold region of short-channel DG MOSFET obtained from solving (97) through the numerical method.

31] took into account the Lombardi CVT mobility model [61] to depict the drain current characteristics.

III. Models for Short Channel DG MOSFETs

A. Electrostatic Potential Models

In the short-channel devices, due to SCEs the electric fields from the source and drain encroach horizontally into the channel and thus introduce a second dimension (y) [Fig. 6] to the channel electrostatics $\phi(x,y)$ [11]. The modeling for nanoscale (short-channel) DG MOSFETs solves 2-D Poisson's equation in order to derive the analytical $\phi(x,y)$ model. The approach adopted in [33−35], derived the $\phi(x,y)$ using superposition method where the 2-D Poisson's equation split into 1-D Poisson and 2-D Laplace equation. The reported papers [20],[32],[36−38] adopted parabolic potential approximation, where $\phi(x,y)$ is obtained using a parabolic function in terms of x and y. This section describes the $\phi(x,y)$ model given by Tsormpatzoglou *et al.* [20] in order to address the modeling scheme for short-channel ($L = 30$ nm) DG MOSFET.

1) Tsormpatzoglou et al. [20]:

Tsormpatzoglou *et al.* [20] presented an analytical expression (94) of the $\phi(x,y)$ along the channel of lightly-doped symmetrical DG MOSFET in weak inversion:

$$\phi(x,y) = \frac{1}{e^{\frac{2L}{\lambda_x}}-1}\left[(V_{bi}+V_{ds}-A_x)\left(e^{\frac{L+y}{\lambda_x}}-e^{\frac{L-y}{\lambda_x}}\right)+ (V_{bi}-A_x)\left(e^{\frac{2L-y}{\lambda_x}}-e^{\frac{y}{\lambda_x}}\right)+A_x\left(e^{\frac{2L}{\lambda_x}}-1\right)\right], \quad (94)$$

with $A_x = V_g - \Delta\chi_{ms} - qN_{si}\frac{\varepsilon_{si}t_{ox}t_{si}+\varepsilon_{ox}(t_{si}-x)x}{2\varepsilon_{ox}\varepsilon_{si}}$. In case of a lightly-doped body, $\Delta\chi_{ms} = -V_T\ln(N_{si}/n_i)$ for mid-gap metal gates [Fig. 3], $V_{bi} = V_T\ln(N_{si}N_{sd}/n_i^2)$ is the built-in potential, and N_{sd} is the doping concentration of source and drain. $\lambda_x = \sqrt{\frac{\varepsilon_{si}t_{ox}t_{si}}{2\varepsilon_{ox}}\left(1+\frac{\varepsilon_{ox}x}{\varepsilon_{si}t_{ox}}-\frac{\varepsilon_{ox}x^2}{\varepsilon_{si}t_{ox}t_{si}}\right)}$ is the natural channel length proposed by Yan *et al.* [9] which is described more accurately as a function channel depth in short-channel devices. The 2-D extra potential $\Delta\phi(x,y)$ induced in the channel due to SCEs is described by:

$$\Delta\phi(x,y) = \frac{1}{e^{\frac{2L}{\lambda_x}}-1}\left[(V_{bi}+V_{ds}-A_x)\left(e^{\frac{L+y}{\lambda_x}}-e^{\frac{L-y}{\lambda_x}}\right)+(V_{bi}-A_x)\left(e^{\frac{2L-y}{\lambda_x}}-e^{\frac{y}{\lambda_x}}\right)\right]. \quad (95)$$

Based on the 2-D extra potential induced in the channel due to SCEs, a semi-analytical expression for the subthreshold drain current is derived. In the subthreshold condition, the diffusion current dominates due to weak inversion [62]. For weak inversion, the drain current in the subthreshold condition of a long channel device can be expressed as:

$$I_{ds,long} = \frac{W}{L}V_T\mu_n Q_{is}\left(1-e^{-\frac{V_{ds}}{V_T}}\right), \quad (96)$$

where $Q_{is} = \frac{qn_i^2}{N_{si}}t_{si}e^{\frac{\phi_s}{V_T}}$ is the inversion charge sheet density at the source end, and $\phi_s = A_{x=0}$ is the surface potential for long channel device. The drain current expression for a short-channel device is obtained by dividing the long channel case by correction factor (CF).

$$I_{ds,short} = \frac{W}{L}V_T\mu_n Q_{is}\frac{1}{CF}\left(1-e^{-\frac{V_{ds}}{V_T}}\right), \quad (97)$$

where $CF = \frac{1}{L}\int_0^L\frac{1}{t_{si}}\int_0^{t_{si}}e^{-\frac{\Delta\phi(x,y)}{V_T}}dxdy$. Here, the CF has to be calculated numerically and hence the model is not applicable in developing a compact model for DG MOSFETs. However, the same can be used to properly design new DG MOSFETS

because it is rather a semi-analytical model of SCE. Also, equation (97) allows extrapolation of various DG device specifications. The subthreshold drain current characteristics of DG MOSFET shown in Fig. 7 with $W = 1\mu$m, $t_{si} = 5$ nm, $t_{ox} = 1$ nm, and μ_n =500 cm^2/Vs for different values of L at $V_{ds} = 0.02$ V have been implemented using MATLAB. In addition, Simpson's one-third method [54] has been employed to evaluate the CF.

```
The MATLAB code to obtain the subthreshold drain
current characteristics [Fig. 7]

W=1000*10^(-9);                    % Channel width
tsi=5*10^(-9);                    % Body thickness
tox=1*10^(-9);             % Gate oxide thickness
Eo=8.85*10^(-12);     %Permittivity of free space
Eox=3.9*Eo;     %Dielectric permittivity of oxide
Esi=11.68*Eo;        %_________________ of silicon
Nsi=10^(21);                % Body doping density
Nsd=5*(10^25);                %S/D doping density
ni=1.45*10^(16);            %Intrinsic    charge
concentration
L=[10 15 20 30 50]*10^(-9);         % Different//
                      %      channel      lengths
considered
u=500*10^(-4);            % Mobility of electrons
K=1.38*10^(-23);             % Boltzmann constant
T=300;                         % Room temperature
q=1.6*10^(-19);               % Elementary charge
VT=(K*T)/q;              % Thermal voltage = 26mV
Vbi=VT*log(Nsi*Nsd/(ni^2));          %   Built-in
% potential
Vfb=-VT*log(Nsi/ni);          % Flat band voltage
Vds=0.02;               % Drain to source voltage
Vg=0:0.1:0.6;                % Gate voltage sweep
Cox=Eox/tox;                  % Oxide capacitance
%------- Simpson's 1/3rd method begins--------- %
h1=((tsi-0)/10);
x=[0 h1 2*h1 3*h1 4*h1 5*h1 6*h1 7*h1 8*h1 9*h1
10*h1];
for l=1:length(L)
h2=(L(l)-0)/10;
y=[0 h2 2*h2 3*h2 4*h2 5*h2 6*h2 7*h2 8*h2 9*h2
10*h2];

for k=1:length(Vgs)
Vg(k)=Vgs(k)-Vfb;
for j=1:length(y)
for i=1:length(x)
xterm(i)=(1+((Eox*x(i))/(Esi*tox))-
((Eox*(x(i)^2))/(Esi*tox*tsi)));
lambda(i)=sqrt(((Esi*tox*tsi)/(2*Eox))*xterm(i))
;
delphi(i)=(1/(exp((2*L(l))/lambda(i))-
1))*((Vbi+Vd-Vg(k))*(exp((L(l)+y(j))/lambda(i))
-exp((L(l)-y(j))/lambda(i)))+(Vbi-
      Vg(k))*(exp((2*L(l)-y(j))/lambda(i))-
exp(y(j)/lambda(i))));

f(i)=exp(-(delphi(i)/VT));
end
```

```
I1(j)=(h1/3)*((f(1)+f(11))+4*(f(2)+f(4)+f(6)+f(8
)+f(10))+2*(f(3)+f(5)+f(7)+f(9)));
End

I2(k)=(h2/3)*((I1(1)+I1(11))+4*(I1(2)+I1(4)+I1(6
)+I1(8))+2*(I1(3)+I1(5)+I1(7)+I1(9)));
    CF(k)=(1/(tsi*L(l)))*I2(k);
    phis(k)=(Vgs(k)-Vfb)-((q*Nsi*tsi)/(2*Cox));

Qis(k)=(q*(ni^2)/Nsi)*tsi*exp((q*phis(k))/(K*T))
;
Id(l,k)=(W/L(l))*(K*T/q)*u*Qis(k)*(1/CF(k))*(1-
exp((-q*Vd)/(K*T)));
end
end
plot(Vg,log10(Id(1,:)),Vg,log10(Id(2,:)),Vg,log1
0(Id(3,:)),Vg,log10(Id(4,:)),Vg,log10(Id(5,:)));
xlabel('V_{g} (V)');
ylabel('I_{ds} (A)')
```

The ϕ model (94) is derived based on the solution of 2-D Poisson's equation under the consideration of fixed charge density only; hence the model is not valid in strong inversion regime. Notable ϕ models [33−35] are derived using the superposition method to validate the same in strong inversion regime. Validity of any ϕ model in the strong inversion regime signifies that the model can depict the variation in electrostatic potential characteristics with respect to the change in V_g. Hamid *et al.* [33] derived the ϕ model considering only the effect of mobile charge density in the 2-D Poisson's equation. The concept of cross-over point [63], which was not put into emphasis in [33], has been discussed later in the ϕ model given Ray and Mahapatra [34]. The ϕ models given by Oh *et al*. [35] and Liang *et al*. [39] did not consider both fixed as well as mobile charge densities, however, Liang *et al*. [39] derived the ϕ model by the scale length method [64]. The ϕ modeling scheme including the fixed charge density in the 2-D Poisson's equation has been further extended by Pandey *et al.* [40] and the same was solved through the Green's function method [65]. Despite differences in mathematical equations, the potential distribution characteristics generated by the ϕ models in [39] and [40] are found to be consistent with each other.

B. Threshold Voltage Models

1) Tsormpatzoglou et al. [21]:

A V_{th} model in [21] of an undoped symmetrical DG MOSFET developed based on the $\phi(x, y)$ model (94) given by Tsormpatzoglou *et al.* [20]. This short-channel V_{th} model was derived by considering only the fixed charge density in Poisson's equation subjected to the condition L/t_{si} >2. The channel position at which the potential along the effective conductive path reaches to its minimum value is called virtual cathode (y_{min}), which plays an important role in deriving the threshold voltage expression. The explicit expression for V_{th} is given as:

$$V_{th} = \Delta\chi_{ms} + AV_T \ln\left(\frac{Q_{th}}{n_i t_{si}}\right) \tag{98}$$

$$-B\left[V_{bi}-V_T\ln\left(\frac{Q_{th}}{n_i t_{si}}\right)\right]^{\frac{1}{2}}\left[V_{bi}+V_{ds}-V_T\ln\left(\frac{Q_{th}}{n_i t_{si}}\right)\right]^{\frac{1}{2}}-C(2V_{bi}+V_{ds}),$$

where $A=\frac{\left(e^{\frac{4L}{\lambda}}-2e^{\frac{2L}{\lambda}}+1\right)}{\left(e^{\frac{2L}{\lambda}}-1\right)^4}$, $B=\frac{2e^{\frac{L}{2\lambda}}\left(e^{\frac{L}{\lambda}}+1\right)}{\left(e^{\frac{2L}{\lambda}}-1\right)^2}$, $C=\frac{2\left(e^{\frac{3L}{\lambda}}-2e^{\frac{2L}{\lambda}}+e^{\frac{L}{\lambda}}\right)}{\left(e^{\frac{2L}{\lambda}}-1\right)^4}$. λ is the natural channel length along the effective conductive path $=\sqrt{\frac{\varepsilon_{si}t_{ox}t_{si}}{2\varepsilon_{ox}}\left(1+\frac{\varepsilon_{ox}t_{si}}{4\varepsilon_{si}t_{ox}}-\frac{\varepsilon_{ox}t_{si}}{16\varepsilon_{si}t_{ox}}\right)}$. For long channel device, $A=1$, and the parameter B and C tend to zero and thus, the V_{th} expression reduces to that of a long-channel DG MOSFET: $V_{th}=\Delta\chi_{ms}+V_T\ln\left(\frac{Q_{th}}{n_i t_{si}}\right)$ as given by Chen *et al.* [18]. The Q_{th} for long channel DG MOSFET has been determined to be about $=3.2\times10^{10}$cm^{-2}. Whereas, for a short-channel device, the Q_{th} is dependent upon the L, t_{ox}, t_{si}, and V_{ds} by the relationship:

$$Q_{th}=10^{11}\left[1-(5+V_{ds})\frac{\lambda}{2L}\right]^2 \text{ cm}^{-2}. \tag{99}$$

C. Drain-Current Models

1) Tsormpatzoglou et al. [22]:

In this model, instead of the numerical approach, an analytical approach is adopted. Various effects like SCEs, series resistance, and CLM are included. Two different equations for subthreshold $I_{ds,SUB}$ and strong inversion $I_{ds,SI}$ have been combined through interpolation method. The detailed derivation of $I_{ds,SI}$ is as follows.

The ϕ model in [16] has been utilized to model the $I_{ds,SI}$, and the model derivation starts from the expression (27), which will imply:

$$\ln\frac{\beta}{\cos\beta}+2r\beta\tan\beta=\frac{V_g-\Delta\chi_{ms}-\phi_F}{2V_T}-ln\left[\frac{2}{t_{si}}\sqrt{\frac{2\varepsilon_{si}k_bT}{q^2n_i}}\right], \tag{100}$$

$$\ln\frac{\beta\sin\beta}{\cos\beta\sin\beta}+2r\beta\tan\beta=\frac{V_g-\Delta\chi_{ms}-\phi_F}{2V_T}-\ln\left[\frac{2}{t_{si}}\sqrt{\frac{2\varepsilon_{si}k_bT}{q^2n_i}}\right], \tag{101}$$

$$\ln\beta\tan\beta-\ln\sin\beta+2r\beta\tan\beta=\frac{V_g-\Delta\chi_{ms}-\phi_F}{2V_T}-\ln\left[\frac{2}{t_{si}}\sqrt{\frac{2\varepsilon_{si}k_bT}{q^2n_i}}\right], \tag{102}$$

Replacing the term "$\beta\tan\beta$" in the $Q_{inv}(y)$ expression (67) by q_i (normalized charge density) and substituting in (63) will yield the $I_{ds,SI}$ expression as:

$$I_{ds,SI}=\mu_n\left(\frac{2W}{L}\right)\int_0^{V_{ds}}\frac{4\varepsilon_{si}k_bT}{qt_{si}}q_i d\phi_F\ . \tag{103}$$

In strong inversion, $\beta\to(\pi/2)$, implies that (102) reduces to:

$$\ln\beta\tan\beta+2r\beta\tan\beta=\frac{V_g-\Delta\chi_{ms}-\phi_F}{2V_T}-\ln\left[\frac{2}{t_{si}}\sqrt{\frac{2\varepsilon_{si}k_bT}{q^2n_i}}\right]. \tag{104}$$

Substituting q_i in (104):

$$\ln q_i+2rq_i=\frac{V_g-\Delta\chi_{ms}-\phi_F}{2V_T}-\ln\left[\frac{2}{t_{si}}\sqrt{\frac{2\varepsilon_{si}k_bT}{q^2n_i}}\right]. \tag{105}$$

Differentiating (105) with respect to q_i will yield: $d\phi_F=-2V_T[2r+(1/q_i)]dq_i$. On substituting the $d\phi_F$ in (103):

$$\begin{aligned}I_{ds,SI}&=-\mu_n\left(\frac{2W}{L}\right)\int_{q_{is}}^{q_{id}}\frac{4\varepsilon_{si}k_bT}{qt_{si}}q_i2V_T\left(2r+\frac{1}{q_i}\right)dq_i\\&=\mu_n\left(\frac{2W}{L}\right)\left(\frac{2\varepsilon_{si}}{t_{si}}\right)\left(\frac{2k_bT}{q}\right)^2\left[2r\frac{q_i^2}{2}+q_i\right]_{q_{id}}^{q_{is}}\\&=\mu_n\left(\frac{2W}{L}\right)\left(\frac{2\varepsilon_{si}}{t_{si}}\right)\left(\frac{2k_bT}{q}\right)^2\left[(q_{is}-q_{id})+\frac{\varepsilon_{si}t_{ox}}{\varepsilon_{ox}t_{si}}(q_{is}^2-q_{id}^2)\right],\end{aligned} \tag{106}$$

where q_{is}, q_{id} are the values of q_i at source ($\phi_F=0$) and drain ($\phi_F=V_{ds}$) ends respectively. The expression for q_i can be derived from (105) as:

$$\ln\left[\frac{2q_i}{t_{si}}\sqrt{\frac{2\varepsilon_{si}k_bT}{q^2n_i}}\right]=\frac{q(V_g-\Delta\chi_{ms}-\phi_F)}{2k_bT}-\frac{2\varepsilon_{si}t_{ox}}{\varepsilon_{ox}t_{si}}q_i. \tag{107}$$

On rearranging the terms of (107):

$$q_ie^{\frac{2\varepsilon_{si}t_{ox}}{\varepsilon_{ox}t_{si}}q_i}=\frac{t_{si}}{2}\sqrt{\frac{q^2n_i}{2\varepsilon_{si}k_bT}}e^{\frac{q(V_g-\Delta\chi_{ms}-\phi_F)}{2k_bT}}. \tag{108}$$

Multiplying on both sides of (108) by $(2\varepsilon_{si}t_{ox}/\varepsilon_{ox}t_{si})$:

$$\frac{2\varepsilon_{si}t_{ox}}{\varepsilon_{ox}t_{si}}q_ie^{\frac{2\varepsilon_{si}t_{ox}}{\varepsilon_{ox}t_{si}}q_i}=\frac{qt_{ox}}{\varepsilon_{ox}}\sqrt{\frac{n_i\varepsilon_{si}}{2k_bT}}e^{\frac{q(V_g-\Delta\chi_{ms}-\phi_F)}{2k_bT}} \tag{109}$$

Since, $We^W=x\Rightarrow W=\text{Lambert}W(x)$, so (109) can be transformed using the Lambert$W$ function:

$$\frac{2\varepsilon_{si}t_{ox}}{\varepsilon_{ox}t_{si}}q_i=\text{Lambert}W\left[\frac{qt_{ox}}{\varepsilon_{ox}}\sqrt{\frac{n_i\varepsilon_{si}}{2k_bT}}e^{\frac{q(V_g-\Delta\chi_{ms}-\phi_F)}{2k_bT}}\right],$$

which will imply:

$$q_i=\frac{\varepsilon_{ox}t_{si}}{2\varepsilon_{si}t_{ox}}\text{Lambert}W\left[\frac{qt_{ox}}{\varepsilon_{ox}}\sqrt{\frac{n_i\varepsilon_{si}}{2k_bT}}e^{\frac{q(V_g-\Delta\chi_{ms}-\phi_F)}{2k_bT}}\right]. \tag{110}$$

The Lambert$W(x)$ function in current expression was first introduced by Ortiz-Conde *et al.* [66]. When the channel is lightly doped, i.e. $n=(n_i^2/N_{si})$ and to incorporate threshold voltage roll-off effect, ΔV_{th} is introduced in (110):

$$q_i=\frac{\varepsilon_{ox}t_{si}}{2\varepsilon_{si}t_{ox}}\text{Lambert}W\left[\frac{qt_{ox}}{\varepsilon_{ox}}\sqrt{\frac{n_i^2\varepsilon_{si}}{2k_bTN_{si}}}e^{\frac{q(V_g-\Delta\chi_{ms}+\Delta V_{th}-\phi_F)}{2k_bT}}\right]. \tag{111}$$

A compact I_{ds} model is obtained by combining the $I_{ds,SI}$ and $I_{ds,SUB}$ through interpolation function.

$$I_{ds}=\frac{I_{ds,SI}\times I_{ds,SUB}}{\left(I_{ds,SI}^m+I_{ds,SUB}^m\right)^{\frac{1}{m}}} \tag{112}$$

where $I_{ds,SUB} = \mu_n \left(\frac{2W}{L}\right)\left(\frac{\varepsilon_{ox}}{t_{ox}}\right)\left(\frac{k_bT}{q}\right)^2 e^{1.8} e^{\frac{V_g - V_{th}}{\eta V_T}} \left[1 + e^{\frac{-V_{ds}}{V_T}}\right]$ and $m = 1.9 - \sqrt{1.2V_{ds}}$ is a parameter that prevents the discontinuity in current characteristics at the transition from subthreshold to above-threshold region.

2) Papathanasiou et al. [23]:

This model is an improvement over the I_{ds} model given by Tsormpatzoglou *et al.* [22]. Papathanasiou *et al.* [23] provided only one equation for I_{ds} which is valid in all region of operation whereas in [22], two equations were combined through interpolation function. The detailed derivation of I_{ds} model is as follows.

In the subthreshold regime ($V_g < V_{th}$), q_i^2 term in (106) can be approximated as zero, i.e. ($q_i^2 \approx 0$) which implies: $q_i \rightarrow Exp\left[q\left(V_g - \Delta\chi_{ms} + \Delta V_{th} - \phi_F\right)/2k_bT\right]$. So, the expression (106) reduces to:

$$I_{ds,SI} = \mu_n \left(\frac{2W}{L}\right)\left(\frac{2\varepsilon_{si}}{t_{si}}\right)\left(\frac{2k_bT}{q}\right)^2 \left[\frac{q_{is}}{2r} - \frac{q_{id}}{2r}\right]$$
$$= \mu_n \left(\frac{2W}{L}\right)\left(\frac{4\varepsilon_{ox}}{t_{ox}}\right)\left(\frac{2k_bT}{q}\right)^2 \left[q_{is} - q_{id}\right]. \quad (113)$$

The $I_{ds,SUB}$ can be approximated as [22]:

$$I_{ds,SUB} = \mu_n \left(\frac{2W}{L}\right)\left(\frac{\varepsilon_{ox}}{t_{ox}}\right)\left(\frac{k_bT}{q}\right)^2 e^{0.8}\left[q_{is,SUB} - q_{id,SUB}\right], \quad (114)$$

where $q_{i,SUB} = Exp\left[q\left(V_g - V_{th} + \Delta V_{th} - \phi_F\right)/\eta k_bT\right]$ and $\eta = (SS/V_T)\ln 10$. On dividing the (114) by (113) will yield:

$$\frac{I_{ds,SUB}}{I_{ds,SI}} = \frac{e^{0.8}}{4} \frac{e^{\frac{q(V_{ge} - V_{th} - \phi_F)}{\eta k_bT}}}{e^{\frac{q(V_{ge} - \Delta\chi_{ms} - \phi_F)}{2k_bT}}}$$
$$= \frac{e^{0.8}}{4} \frac{e^{\frac{q(V_{ge} - V_{th} - \phi_F)}{\eta k_bT}}}{e^{\frac{q(V_{ge} - V_{th} - \phi_F + V_{th} - \Delta\chi_{ms})}{2k_bT}}}$$
$$= \frac{e^{0.8}}{4} \frac{e^{\frac{q(V_{ge} - V_{th} - \phi_F)}{\eta k_bT}} e^{\frac{q(V_{ge} - V_{th} - \phi_F)}{2k_bT}}}{e^{\frac{q(V_{th} - \Delta\chi_{ms})}{2k_bT}}}$$
$$= \frac{e^{\frac{q(V_{ge} - V_{th} - \phi_F)}{2\eta_{eff}k_bT}}}{\frac{4}{e^{0.8}} e^{\frac{q(V_{th} - \Delta\chi_{ms})}{2k_bT}}}, \quad (115)$$

where $V_{ge} = V_g + \Delta V_{th}$ and $\eta_{eff} = \frac{2-\eta}{\eta}$.

In the paper [23], (115) is expressed as:

$$\frac{I_{ds,SUB}}{I_{ds,SI}} = \frac{e^{\frac{q(V_{ge} - V_{th} - \phi_F)}{2\eta_{eff}k_bT}}}{\frac{4}{e^{0.8}} e^{\frac{q(V_{th} + \Delta\chi_{ms})}{1V}}} \quad (116)$$

In this model, only one equation has to be used for both the subthreshold and strong inversion regime. So, it is decided to investigate the possibility of altering the z parameter of Lambert$W(z)$ in q_i, to accommodate for the change in slope of the exponent, at the point where the DG MOSFET is entering the subthreshold mode of operation. Considering: $\frac{4}{e^{0.8}} e^{\frac{q(V_{th} + \Delta\chi_{ms})}{1V}} = A$ (from 116), the q_i from (110) is transformed into:

$$q_i = \text{Lambert}W\left[\frac{q t_{ox}}{\varepsilon_{ox}} \sqrt{\frac{n_i^2 \varepsilon_{si}}{2k_bTN_{si}}} \frac{e^{\frac{q(V_{ge} - \Delta\chi_{ms} - \phi_F)}{2k_bT}} e^{\frac{q(V_{ge} - V_{th} - \phi_F)}{2\eta_{eff}k_bT}}}{A + e^{\frac{q(V_{ge} - V_{th} - \phi_F)}{2\eta_{eff}k_bT}}}\right]$$

In addition, to model the I_{ds}, a flag $isSI$ is used, which is $= 1$ when the device is in strong inversion and $= 0$ when the device is in weak inversion. The $isSI$ function can be implemented by using "tanh" function [41−43], which is expressed as: $isSI = \frac{1}{2} + \frac{\tanh[5(V_g - \Delta V_{th})]}{2}$. Finally the I_{ds} model is expressed as:

$$I_{ds,SI} = \mu_n \left(\frac{2W}{L}\right)\left(\frac{2\varepsilon_{si}}{t_{si}}\right)\left(\frac{2k_bT}{q}\right)^2 \left[\left(\frac{q_{is}}{2r} - \frac{q_{id}}{2r}\right) + isSI \times r\left(\frac{q_{is}^2}{4r^2} - \frac{q_{id}^2}{4r^2}\right)\right]. \quad (117)$$

The complete I_{ds} model (118) is incorporated with various effects like surface roughness scattering, velocity saturation, series resistance between drain and source, and CLM (shown at the bottom of the page). where θ is the mobility attenuation factor due to surface roughness scattering, v_{sat} is the high-field electron drift-velocity saturation, R_{sd} is the equivalent resistance between the source and drain, and F_{CLM} is the CLM factor. For channel electric field of $E_y = 10^5$ Vcm^{-1} and higher, v_{sat} in the channel reaches a value about $v_{sat} = 10^7$ cms^{-1} [67]. The empirical relationship of F_{CLM} is:

$$F_{CLM} = 1 + \left(\frac{\lambda}{L}\right)^A \left(\frac{V_{ds,eff}}{V_{g,eff} - V_{th}}\right) \quad (119)$$

with $A = 1.2 - \sqrt{\lambda/L}$. In order to avoid a discontinuity at $V_g = V_{th}$ and $V_{ds} = V_g - V_{th}$, the smoothing functions: $V_{g,eff} = 2V_{th} + \left(V_g - 2V_{th}\right)\tanh\left(V_g/V_{th}\right)^2$ and $V_{ds,eff} = V_{ds}\tanh\left(1.5V_{ds}/V_{g,eff}\right)^2$ are introduced.

The I_{ds} models [22,23] are charge based compact model since the I_{ds} is expressed in terms of charge densities at source and drain ends. The short-channel models [20−23] have been integrated through Verilog-A code (given in Appendix A) in order to implement a DG MOSFET whose parameters are specified as: $L = 30$ nm, $W = 50$ nm, $t_{si} = 12$ nm, $t_{ox} = 1$ nm, $N_{si} = 10^{15}$ cm^{-3}, $N_{sd} = 10^{20}$ cm^{-3}, and $\mu_n = 500$ cm^2/Vs. The Lambert$W$ function has been coded using the algorithm given by Morris *et al.* [68]. Fig. 8 shows the I_{ds} characteristics observed in Spectre simulator for V_g sweep from 0 to 1.2 V at $V_{ds} = 1$ V. Fig. 8(b) ensures symmetry of the device when the

$$I_{ds} = \frac{\mu_n}{1 + \theta\left(V_g - V_{th}\right)\left(1 + \frac{\mu_n V_{ds}}{v_{sat}L}\right) + \frac{2WC_{ox}\mu_n}{L} R_{sd}\left(V_g - V_{th}\right)} \left(\frac{2W}{L}\right)\left(\frac{2\varepsilon_{si}}{t_{si}}\right)\left(\frac{2k_bT}{q}\right)^2 \left[\left(q_{is} - q_{id}\right) + isSI \times \frac{\varepsilon_{si}t_{ox}}{\varepsilon_{ox}t_{si}}\left(q_{is}^2 - q_{id}^2\right)\right] \times F_{CLM} \quad (118)$$

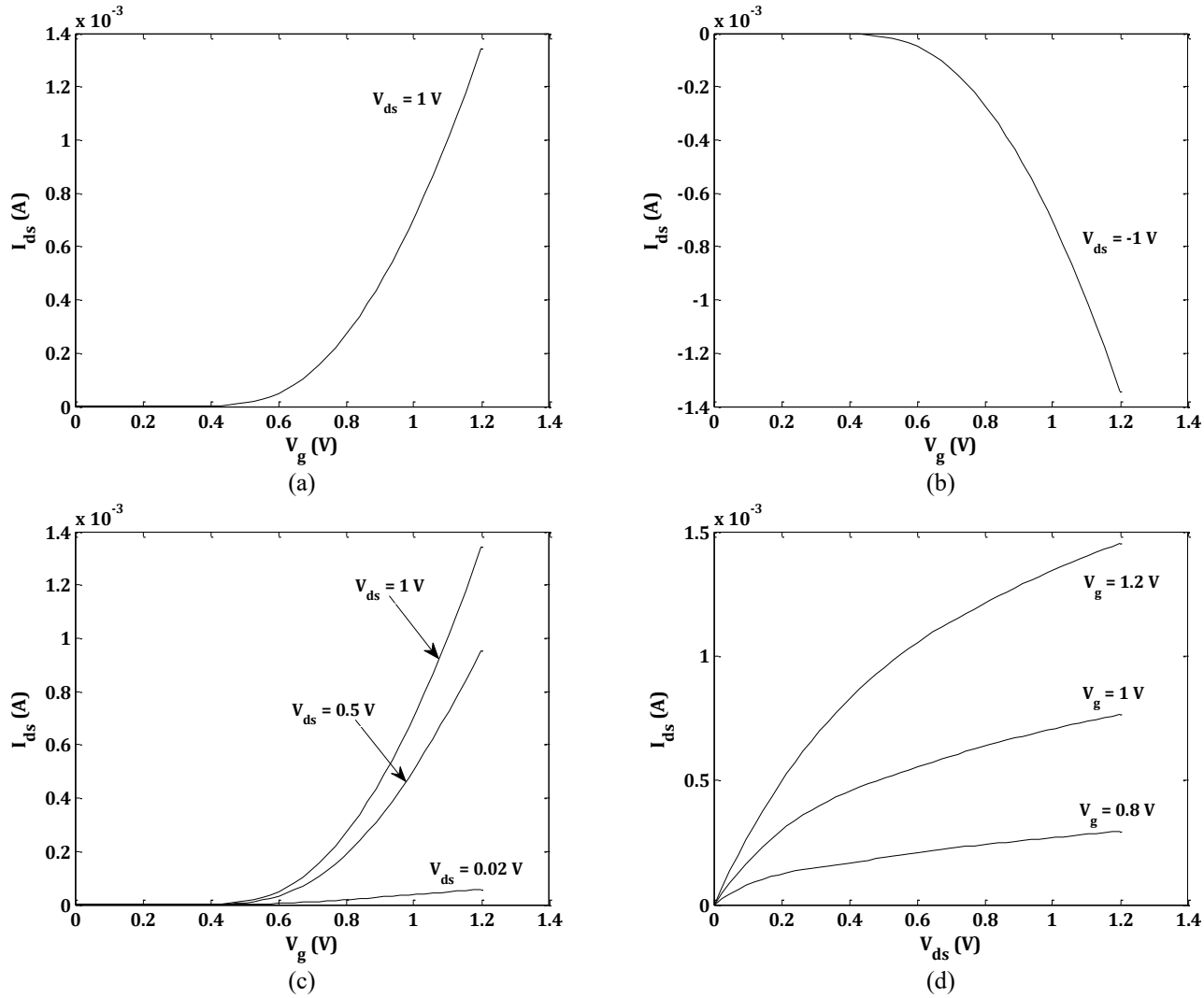

Fig. 8. Simulation results of short-channel DG MOSFET obtained in Spectre (a) transfer characteristics at V_{ds} =1V, (b) transfer characteristics at $V_{ds} = -1$V, (c) transfer characteristics for different values of V_{ds}, (d) output characteristics for different values of V_g.

polarity of V_{ds} is reversed. The transfer and output characteristics in Fig. 8 (c−d) are in close agreement with the simulation results in [23]. Fig. 9 shows the correlation between I_{ds} models (112) and (118); it is observed that the two different equations lead to similar results for the same DG MOSFET structure.

3) Taur et al. [24]:

This model is an improvement over the I_{ds} model [19] by considering the effect of lateral electric field on mobile charge density which was earlier ignored due to the assumption given by the GCA model. This model augments the GCA to produce finite output conductance in the saturation region. Addition to this, the conventional definition of pinch-off and CLM effects in the saturation region has been reinterpreted. Fig. 10 shows the comparison TCAD simulation results with the I_{ds} model [19] considering the parameters : $L = 100$ nm, $W = 1$ µm, $t_{si} = 4$ nm, $t_{ox} = 2$ nm, $\varepsilon_{si} = \varepsilon_{ox} \approx 11.8\varepsilon_0$, μ_n =200 cm^2/(Vs), $N_{SD} = 10^{21}$ cm^{-3}, and $V_0 = 0.33$ V. The TCAD simulation results [24] in Fig. 10 show that there is no pinch-off point in the channel as depicted by GCA model. The failure of the GCA model in bulk MOSFETs was previously also demonstrated in [69] through the TCAD simulation. The pinch-off point is interpreted as the condition in the channel at which there is a sign change in the vertical electric field (E_x) occurs or $E_x = 0$, which has also been suggested earlier in [70] (for the bulk MOSFETs only). The CLM in saturation region is interpreted as the movement of the point at which the oxide electric field becomes zero in the source side. The complete I_{ds} model equation is expressed as:

$$\frac{I_{ds}}{\mu_n W} y = \frac{4\varepsilon_{si}}{t_{si}} \left(\frac{2k_b T}{q}\right)^2 \left[\beta \tan\beta - \frac{\beta^2}{2} + r\beta^2 \tan^2\beta\right]\Big|_{\beta=\beta_d}^{\beta_s} - \frac{C_{ox}}{4}\left[\left|V_g - V_0 - V\right| - \left(V_g - V_0 - V\right)\right]^2 + \frac{\varepsilon_{si} t_{si}}{2}\left[\left(\frac{dV}{dy}\right)^2 - E_0^2\right], \quad (120)$$

where E_0 is the lateral electric field at the source can be calculated numerically from the relation:

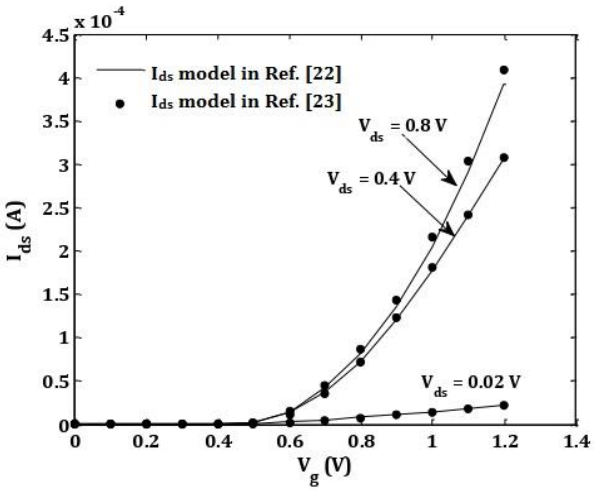

(a)

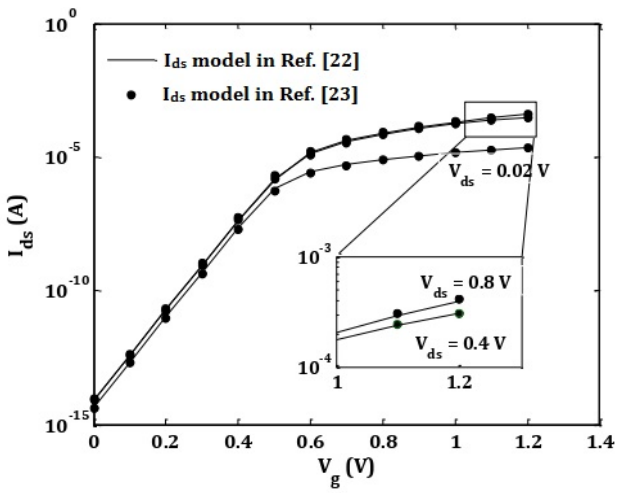

(b)

Fig. 9. Simulation results showing transfer characteristics of a short-channel DG MOSFET obtained from models (112) and (118) in (a) linear scale, (b) semi-logarithmic scale.

$$E_0 = \frac{I_{ds}}{2\mu_n W C_{ox}(V_g - V_0)} \tag{121}$$

The I_{ds} model (121) results are consistence with the TCAD simulation results.

IV. Conclusion

A comprehensive review based on the fundamental issues related to electrostatic potential, threshold voltage, and drain current formulations of analytic models for symmetric n-type DG MOSFETs for long as well as short channel have been presented in this paper. Equations for respective models have been analysed, and related derivations have been carried out for the further application of the models. Moreover, the correlation between the models carried out by various researchers has also been surveyed and discussed. This review provides an insight for understanding the mathematical models and also offers knowledge for modeling and designing the increasingly important DG MOSFETS. This work can be of interest to researchers working in these MOSFETs.

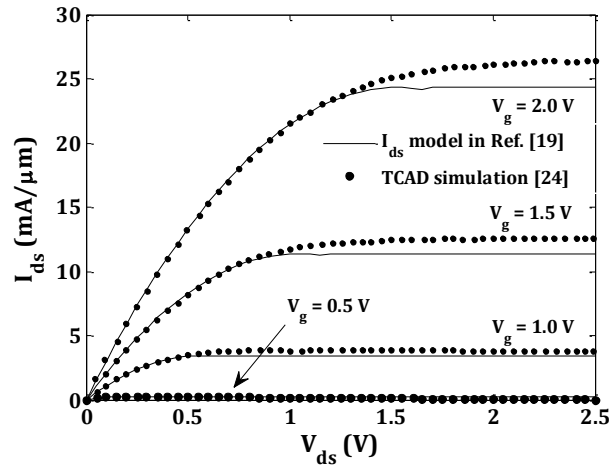

Fig. 10. Characteristics of a short-channel DG MOSFET obtained from model (93) in comparison with the TCAD simulation results [24].

Appendix

A. Verilog-A Implementation of Short-Channel DG MOSFET (n-Type)

```
// VerilogA for nDGMOS
`include "constants.vams"
`include "disciplines.vams"
module nDGMOS(Vgs,Vdd, Vss);
input Vgs;
inout Vdd, Vss;

// Technological Parameters
electrical Vgs, Vdd, Vss;
parameter real Eo=8.85e-12;
parameter real K=1.38e-23;
parameter real T=300;
parameter real q=1.6e-19;
parameter real tsi=12e-9;
parameter real tox=1e-9;
parameter real Nsi=1e21;
parameter real Nsd=1e26;
parameter real ni=1.45e16;
parameter real L=30e-9;
parameter real W=50e-9;
parameter real u=500e-4;
parameter real VT=0.0259;

// Model Parameters

real
Vg,Vd,Vs,Eox,Esi,lambda,Vfb,Vth,Vthlong,delVth,r
,fixed,power,n,nd,A,Vge,Vgeff,Vx,Vdeff,FCLM,num1
,
den1,qis,num2,den2,qid,isSI,x1,x2,SS;
```

```
// Threshold voltage calculation [Vth model(98)]:

analog function real threshold;
input l;
real
Eox,Esi,l,Vfb,Vbi,Vds,lambda,Qth,Q,den,k1,k2,k3;
begin
        Eox=3.9*Eo;
        Esi=11.68*Eo;

//Built-in potential:
        Vbi=VT*ln(Nsd*Nsi/pow(ni,2));
        Vds=0.02;

// Flat-band voltage:
        Vfb=-VT*ln(Nsi/ni);

// Natural channel length:
        lambda=sqrt(((Esi*tox*tsi)/(2*Eox))*(1+(E
ox*tsi)/(4*Esi*tox)-(Eox*tsi)/(16*Esi*tox)));

// The Qth (38):
        Qth=1e15*pow((1-
(5+Vds)*(lambda/(2*l))),2);

        Q=(Qth*Nsi)/(pow(ni,2)*tsi);
                        den=exp(l/lambda)-1;
                        k1=(exp(4*l/lambda)-
2*exp(2*l/lambda)+1)/pow(den,4);

        k2=(2*exp(l/(2*lambda))*(1+exp(l/lambda))
)/pow(den,2);
        k3=(2*exp(3*l/lambda)-
4*exp(2*l/lambda)+2*exp(l/lambda))/pow(den,4);

        threshold=Vfb+k1*VT*ln(Q)-k2*sqrt((Vbi-
VT*ln(Q))*(Vbi+Vds-VT*ln(Q)))-k3*(2*Vbi+Vds);
        end
endfunction

// Subthreshold slope calculation [20]:

analog function real subthreshold;
input l;
real Eox,Esi,l,lambda, alpha;
begin
Eox=3.9*Eo;
Esi=11.68*Eo;
lambda=sqrt(((Esi*tox*tsi)/(2*Eox))*(1+((Eox*tsi
)/(4*Esi*tox))-((Eox*tsi)/(16*Esi*tox))));
        alpha=L/(2*lambda);

        subthreshold=VT*ln(10)*((exp(4*alpha)-
1)/(exp(4*alpha)+2*exp(alpha)-2*exp(3*alpha)));
        end
endfunction

// lambertW function calculation [68]:

analog function real lambertw;
input x;
real
x,z,L1,L2,term1,term2,term3,term4,term5,term6,
term7,term8,term9,term10,term11;
begin
        if(x<8)
        begin
        z=x/exp(1);
        term1=(z*(z-1))/(1+z);
        term2=(z*pow((z-1),2))/(2*pow((1+z),3));
        term3=(pow((z-1),3)*(z-
2*pow(z,2)))/(6*pow((1+z),5));
        term4=(z*(6*pow(z,2)-8*z+1)*pow((z-
1),4))/(24*pow((1+z),7));
        term5=(z*(24*pow(z,3)-58*pow(z,2)+22*z-
1)*pow((z-1),5))/(120*pow((1+z),9));
        term6=(z*(120*pow(z,4)-
444*pow(z,3)+328*pow(z,2)-
52*z+1))/(720*pow((1+z),11));
        term7=(z*(720*pow(z,5)-
3708*pow(z,4)+4400*pow(z,3)-1452*pow(z,2)+114*z-
1))/(5040*pow((1+z),13));

lambertw=z-term1+term2-term3+term4-term5+term6-
term7;
end
        else
        begin
        L1=ln(x);
        L2=ln(ln(x));
        term8=(L2*(-2+L2))/(2*pow(L1,2));
        term9=(L2*(6-
9*L2+2*pow(L2,2)))/(6*pow(L1,3));
        term10=(L2*(-12+36*L2-
22*pow(L2,2)+3*pow(L2,3)))/(12*pow(L1,4));
        term11=(L2*(60-300*L2+350*pow(L2,2)-
125*pow(L2,3)+12*pow(L2,4)))/(60*pow(L1,5));

lambertw=L1-
L2+(L2/L1)+term8+term9+term10+term11;
        end
        end
endfunction

//Drain-current calculation [23]:
analog begin
Eox=3.9*Eo;
Esi=11.68*Eo;
Vg=V(Vgs);
Vd=V(Vdd);
Vs=V(Vss);
Vfb=-VT*ln(Nsi/ni);
lambda=sqrt(((Esi*tox*tsi)/(2*Eox))*(1+(Eox*tsi)
/(4*Esi*tox)-(Eox*tsi)/(16*Esi*tox)));
Vth=threshold(L);
Vthlong=threshold(100e-9);
delVth=Vth-Vthlong;
r=(Esi*tox)/(Eox*tsi);
fixed=((q*tox)/Eox)*sqrt((Esi*pow(ni,2))/(2*K*T*
Nsi));
power=1-sqrt(lambda/L);
SS=subthreshold(L);
n=SS/(VT*ln(10));
nd=n/(2-n);
A=(4/exp(0.8))*exp((Vth+Vfb)/1);
Vge=Vg+delVth;
Vgeff=2*Vth+(Vge-2*Vth)*tanh(pow((Vge/Vth),2));
Vx=abs(Vd-Vs);
```

```
Vdeff=Vx*tanh(pow((1.5*Vx/Vgeff),2));
FCLM=1+(pow((lambda/L),power)*(Vdeff/(Vgeff-
Vth)));
num1=exp((Vg+delVth-Vfb-
Vs)/(2*VT))*exp((Vg+delVth-Vth-Vs)/(2*nd*VT));
den1=A+exp((Vg+delVth-Vth-Vs)/(2*nd*VT));
x1=fixed*num1/den1;

//Normalized charge density q_is and q_id [23]:
qis=lambertw(x1);
num2=exp((Vg+delVth-Vfb-
Vd)/(2*VT))*exp((Vg+delVth-Vth-Vd)/(2*nd*VT));
den2=A+exp((Vg+delVth-Vth-Vd)/(2*nd*VT));
x2=fixed*num2/den2;
qid=lambertw(x2);

//The isSI:
isSI=(tanh(5*(Vg+delVth-Vth))/2)+0.5;

//The I_ds model (118):
I(Vdd,Vss)
<+((u*2*W/L)*(2*Esi/tsi)*pow((2*VT),2)*((qis/(2*
r))-(qid/(2*r))+isSI*r*(pow((qis/(2*r)),2)-
pow((qid/(2*r)),2))))*FCLM;
end
endmodule
```


ACKNOWLEDGMENT

The authors would like to thank Mr. Sheikh Wasmir Hussain, Research scholar from the Department of Electronics and Communication Engineering, National Institute of Technology Meghalaya, India for his help and useful suggestions.

REFERENCES

[1] J. Koomey, S. Berard, M. Sanchez, and H. Wong, "Implications of historical trends in the electrical efficiency of computing," *IEEE Ann. Hist. Comput.*, vol. 33, no. 3, pp. 46-54, Mar. 2011.

[2] H.R. Huff, "John Bardeen and transistor physics," in *Proc. AIP Conf.*, vol. 550, no. 3, pp. 3-29, Mar. 2001.

[3] W.C. Holton and R.K. Cavin, "A Perspective on CMOS technology trends," in *Proc. IEEE*, vol. 74, no. 12, pp. 1646-1668, Dec. 1986.

[4] D. Kahng, "A historical perspective on the development of MOS transistors and related devices," *IEEE Trans. Electron Devices*, vol. 23, no. 7, pp. 655-657, Jul. 1976.

[5] F. Wanlass and C. Sah, "Nanowatt logic using field-effect metal-oxide semiconductor triodes," in *Proc. IEEE Solid-State Circuits Conf.*, vol. 6, pp.32-33, Feb. 1963.

[6] D.J. Frank *et al*., "Device scaling limits of Si MOSFETs and their application dependencies," in *Proc. IEEE*, vol. 89, no. 3, pp. 259-288, Mar. 2001.

[7] N. Z. Haron and S. Hamdioui, "Why is CMOS scaling coming to an END?," in *Proc. 3rd Int. Design Test Workshop*, Dec. 2008, pp. 98–103.

[8] A. Asenov *et al.*, "Increase in the random dopant induced threshold fluctuations and lowering in sub-100 nm MOSFETs due to quantum effects: a 3-D density gradient simulation study," *IEEE Trans. Electron Devices*, vol. 48, no. 4, pp. 722-729, Apr. 2001.

[9] R.-H. Yan, A. Ourmazd, and K.F. Lee, "Scaling the Si MOSFET: from bulk to SOI to bulk," *IEEE Trans. Electron Devices*, vol. 39, no. 7, pp. 1704-1710, Jul. 1992.

[10] Q. Xie, J. Xu, and Y. Taur, "Review and critique of analytic models of MOSFET short-channel effects in subthreshold," *IEEE Trans. Electron Devices*, vol. 59, no. 6, Jun. 2012.

[11] I. Ferain, C.A. Colinge, and J.-P. Colinge, "Multigate transistors as the future of classical metal-oxide-semiconductor field-effect-transistor," *Nature*, vol. 479, no. 7373, pp. 310-316, Nov. 2011.

[12] T. Sekigawa and Y. Hayashi, "Calculated threshold-voltage characteristics of an XMOS transistor having an additional bottom gate," *Solid-State Electron.*, vol. 27, no. 8-9, pp. 827-828, Aug. 1984.

[13] H. Lu, "Compact modeling of double-gate MOSFETs," Ph.D dissertation, Univ. California, San-Diego, CA, 2006.

[14] F. Balestra *et al.*, "Double-gate silicon-on-insulator transistor with volume inversion," *IEEE Electron Device Lett.*, vol. 8, no. 9, pp. 410-412, Sep. 1987.

[15] Y. Taur, "An analytical solution to a double-gate MOSFET with undoped body," *IEEE Electron Device Lett.*, vol. 21, no. 5, pp. 245-247, May, 2000.

[16] H. Lu and Y. Taur, "An analytic potential model for symmetric and asymmetric DG MOSFETs," *IEEE Trans. Electron Devices*, vol. 53, no. 5, pp. 1161-1168, May 2006.

[17] C. Hong, J. Zhou, Q. Cheng, K. Zhu, J.B. Kio, and Y. Chen, "Unified continuous and discrete model for double-gate MOSFETs with spatially varying or pulsed doping profiles," *IEEE J. Electron Devices Soc*., vol. 5, no. 4, pp. 244−255, Jul. 2017.

[18] Q. Chen, E.M. Harrell and J.D. Meindl, "A physical short-channel threshold voltage model for undoped symmetric double-gate MOSFETs," *IEEE Trans. Electron Devices*, vol. 50, no. 7, pp. 1631-1637, Jul. 2003.

[19] Y. Taur, X. Liang, W. Wang, and H. Lu, "A continuous, analytic drain-current model for DG MOSFETs," *IEEE Electron Device Lett*., vol. 25, no. 2, pp. 107-109, Feb. 2004.

[20] A. Tsormpatzoglou *et al*., "Semi-analytical modeling of short-channel effects in Si and Ge symmetrical double-gate MOSFETs," *IEEE Trans. Electron Devices*, vol. 54, no. 8, pp. 1943-1952, Aug. 2007.

[21] A. Tsormpatzoglou *et al*., "Threshold voltage model for short-channel undoped symmetrical double-gate MOSFETs," *IEEE Trans. Electron Devices*, vol. 55, no. 9, pp. 2512-2516, Sep. 2008.

[22] A. Tsormpatzoglou *et al*., "Analytical modelling for the current-voltage characteristics of undoped or lightly-doped symmetric double-gate MOSFETs," *Microelectron. Eng*., vol. 87, no. 9, pp. 1764-1768, Nov. 2010.

[23] K. Papatahanasiou *et al*., "Symmetrical unified compact model for short-channel double-gate MOSFETs," *Solid-State Electron*., vol. 69, pp. 55-61, Mar. 2012.

[24] Y. Taur and H.-H. Lin, "Modeling of DG MOSFET $I-V$ characteristics in the saturation region," *IEEE Trans. Electron Devices*, vol. 65, no. 5, pp. 1714-1720, May 2018.

[25] B. Yu, H. Lu, M. Liu, and Y. Taur, "Explicit continuous models for double-gate and surrounding-gate MOSFETs," *IEEE Trans. Electron Devices*, vol. 53, no. 10, pp. 2715-2721, Oct. 2007.

[26] V.R. Murnal and C. Vijaya, "A quasi-ballistic drain current, charge and capacitance model with positional carrier scattering dependency valid for symmetric DG MOSFETs in nanoscale regime," *Nano Convergence*, vol. 6, no. 19, Jun. 2019.

[27] J.-M. Sallese, F. Krummenacher, F. Pregaldiny, C. Lallement, A. Roy, and C. Enz, "A design oriented charge-based current model for symmetric DG MOSFET and its correlation with the EKV formalism," *Solid-State Electron*., vol. 49, no. 3, pp. 485-489, Mar. 2005.

[28] V. Hariharan, J. Vasi, and V.R. Rao, "Drain current model including velocity saturation for symmetric double-gate MOSFETs," *IEEE Trans. Electron Devices*, vol. 55, no. 8, pp. 2173- 2180, Aug. 2008.

[29] L. Zhang, Y. Guan, W. Zhou, L. Chen, Y. Xu, and J. He, "A carrier-based analytic drain current model incorporating velocity saturation for undoped surrounding-gate MOSFETs," *Semicond. Sci. Technol*., vol. 24, no. 11, pp. 115003, Oct. 2009.

[30] Z. Chen *et al*., Surface-potential based drain current model for long channel junctionless double-gate MOSFETs," *IEEE Trans. Electron Devices,* vol. 59, no. 12, pp. 3292-3298, Dec. 2012.

[31] X. Jin, X. Liu, M. Wu, R. Chuai, and J.-H. Lee, and J.-H. Lee, "A unified analytical continuous current model applicable to accumulation mode (junctionless) and inversion mode MOSFETs with symmetric and

asymmetric double-gate structures," *Solid-State Electron*., vol. 79, pp. 206-209, Jan. 2013.

[32] V.K.S. Yadav and R.K. Baruah, "An analytic potential and threshold voltage model of short-channel symmetric double-gate MOSFET," in *Proc. IEEE Int. Symp. VLSI Design Test*, Jul. 2014.

[33] H.A.E. Hamid, J. R. Guitart, and B. Iniguez, "Two-dimensional analytical threshold voltage and subthreshold swing models of undoped symmetric double-gate MOSFETs," *IEEE Trans. Electron Devices*, vol. 54, no. 6, pp. 1402-1408, Jun. 2007.

[34] B. Ray and S. Mahapatra, "Modeling of channel potential and subthreshold slope of symmetric double-gate transistor," *IEEE Trans. Electron Devices*, vol. 56, no. 2, pp. 260-266, Feb. 2009.

[35] S.-H. Oh, D. Monroe, and J.M. Hergenrother, "Analytic description of short-channel effects in fully depleted double-gate and cylindrical surrounding-gate MOSFETs," *IEEE Electron Device Lett*., vol. 21, no. 9, pp. 445-447, Nov. 2000.

[36] F. Lime, B. Iniguez, and O. Moldovan, "A quasi-two-dimensional compact drain-current model for undoped symmetric double-gate MOSFETs including short-channel effects," *IEEE Trans. Electron Devices*, vol. 55, no. 6, pp. 1441-1448, Jun. 2008.

[37] H. Abebe *et al*., "Symmetric and asymmetric double gate MOSFET modelling," *J. Semicond. Technol. Sci*., vol. 9, no. 4, pp. 225-232, Dec. 2009.

[38] J. Prasad, A. Agarwal, P.C. Pradhan, and B.P. Swain, "Analytical modeling of surface potential for double-gate MOSFET," in *Advances in Communication, Devices and Networking. Lecture Notes in Electrical Engineering*, vol. 537. R. Bera, S. Sarkar, O. Singh, and H. Saikia, Eds. Singapore: Springer, 2019, pp. 55-62.

[39] X. Liang and Y. Taur, "A 2-D analytical solution for SCEs in DG MOSFETs," *IEEE Trans. Electron Devices*, vol. 51, no. 8, pp. 1385-1391, Aug. 2004.

[40] N. Pandey, H.-H. Lin, A. Nandi, and Y. Taur, "Modeling of short-channel effects in DG MOSFETs: Green's function method versus scale length model," *IEEE Trans. Electron Devices*, vol. 65, no. 8, pp. 3112-3119, Aug. 2018.

[41] A. Cerdeira, B. Iniguez, and M. Estrada, "Compact model for short channel symmetric doped double-gate MOSFETs," *Solid-State Electron*., vol. 52, no. 7, pp. 1064-1070, Jul. 2008.

[42] A. Cerdeira, O. Moldovan, B. Iniguez, and M. Estrada, "Modeling of potentials and threshold voltage for symmetric doped double-gate MOSFETs," *Solid-State Electron*., vol. 52, no. 5, pp. 830-837, May 2008.

[43] J. Alvarado *et al*., "Implementation of the symmetric double-gate MOSFET model in Verilog-A for circuit simulation," *Int. J. Numer. Model., Electron, Netw, Devices Fields*, vol. 23, no. 2, pp. 88-106, Mar/Apr. 2010.

[44] M. Cheralathan *et al*., "Compact drain-current model for reproducing transport advanced transport models in nanoscale double-gate MOSFETs," *Semicond. Sci. Technol*., vol. 26, no. 9, pp. 095015, Jul. 2011.

[45] M. Cheralathan *et al*., "Implementation of nanoscale double-gate CMOS circuits using compact advanced transport models," *Microelctronics J*., vol. 44, no. 2, pp. 80-85, Feb. 2013.

[46] A. Qrtiz-Conde, F.J. Garcia-Sanchez, J. Muci, S. Malobabic, and J.J. Liou., "A review of core compact models for undoped double-gate SOI MOSFETs," *IEEE Trans. Electron Devices*, vol. 54, no. 1, pp. 131-140, Jan. 2007.

[47] J. Song, B. Yu, Y. Yuan, and Y. Taur, "A review on compact modeling of multiple-gate MOSFETs," *IEEE Trans. Circuits Syst.-I: Reg. Papers*, vol. 54, no. 1, pp. 1858-1869, Jul. 2009.

[48] K.K. Young, "Short-channel effect in fully depleted SOI MOSFETs," *IEEE Trans. Electron Devices*, vol. 36, no. 2, pp. 399-402, Feb. 1989.

[49] Verilog-A language reference manual: analog extensions to Verilog HDL, version 1.0, Open Verilog International; 1996.

[50] H.C. Pao and C.T. Sah, "Effects of diffusion current on characteristics of metal-oxide (insulator)-semiconductor transistors," *Solid-State Electron*., vol. 9, no. 10, pp. 927-937, Oct. 1966.

[51] Y.Taur and T. Ning, *Fundamentals of VLSI Devices*. Cambridge, U.K.: Cambridge Univ. Press, 2009.

[52] J.R. Hauser and M.A. Littlejohn, "Approximations for accumulation and inversion space-charge layers in semiconductor," *Solid-State Electron.*, vol. 11, no. 7, pp. 667-674, Jul. 1968.

[53] R.U. Ahmed and P. Saha, "Modeling of threshold voltage and subthreshold current for p-channel symmetric double-gate MOSFET in nanoscale regime," in *Proc. IEEE Int. Symp. Nanoelectron. Information Syst.*, Dec. 2017, pp. 179-183.

[54] B.S. Grewal, *Higher Engineering Mathematics.* New Delhi, India: Khanna Publishers, 2012.

[55] R. Shankar, G. Kaushal, S. Maheshwaram, , S. Dasgupta, and S.K. Manhas, "A degradation model of double-gate and gate-all-around MOSFETs with interface trapped charges including effects of channel mobile charge carriers," *IEEE Trans. Device Material Reliab.*, vol. 14, no. 2, pp. 689−697, Jun. 2014.

[56] J. Zhou, "On compact model for double-surrounding-gate MOSFETs and the yield study of lithographic processes," Ph.D dissertation, Peking Univ., Beijing, China, 2016.

[57] J.R. Brews, "A charge-sheet model of the MOSFET," *Solid-State Electron.*, vol. 21, no. 2, pp. 345−355, Feb. 1978.

[58] A. Dasgupta, A. Agarwal S. Khandelwal, and Y.S. Chauhan, "Compact modeling of surface potential, charge, and current in nanoscale transistors under quasi-ballistic regime," *IEEE Trans. Electron Devices*, vol. 63, no. 11, pp. 4151-4159, Nov. 2016.

[59] M. Reyboz, O. Rozeau, and T. Poiroux, "Compact modeling of double gate MOSFET for IC design," in *Planar Double-Gate Transistor. From Technology to Circuit*. A. Amara and O. Rozeau, Eds. Dordrecht: Springer, 2009, pp. 55-88.

[60] D. M. Caughey and R. E. Thomas, "Carrier mobilities in silicon empirically related to doping and field," *Proc. IEEE*, vol. 55, no. 12, pp. 2192–2193, Dec. 1967.

[61] C. Lombardi, S. Manzini, A. Saporito, and M. Vanzi, "A physically based mobility model for numerical simulation of nonplanar devices," *IEEE Trans. Comput.-Aided Des.,* vol. 7, no. 11, pp. 1164-1171, Nov. 1988.

[62] N. Arora, *MOSFET Models for VLSI Circuit Simulation: Theory and Practice*. New York, USA: Springer-Verlag, 1993.

[63] R.K. Baruah and S. Mahapatra, "Justifying threshold voltage definition for undoped body transistors through''crossover point'' concept," *Physica B*, vol. 404, no. 8-11, pp. 1029-1032, May 2009.

[64] D. J. Frank, Y. Taur, and H.-S. P. Wong, "Generalized scale length for two-dimensional effects in MOSFETs," *IEEE Electron Device Lett*., vol. 19, no. 10, pp. 385–387, Oct. 1998.

[65] A. Nandi, N. Pandey, and S. Dasgupta, "Analytical modeling of DGMOSFET in subthreshold regime by green's function approach," *IEEE Trans. Electron Devices*, vol. 64, no. 8, pp. 3056–3062, Aug. 2017.

[66] A. Ortiz-Conde, F.J. Garcia-Sanchez, and M. Guzman, "Exact analytical solution of channel surface potential as an explicit function of gate voltage in undoped-body MOSFETs using the LambertW function and a threshold voltage therefrom," *Solid-State Electron.*, vol. 47, no. 11, pp. 2067-2074, Nov. 2003.

[67] S.-M. Kang and Y. Leblebici, *CMOS Digital Integrated Circuits Analysis and Design*. New York, USA: Mc-Graw Hill, 2003.

[68] H. Morris, E. Cumberbatch, H. Abebe, and V. Tyree, "Compact models for the I-V characteristics of double-gate and surround gate MOSFETs," in *Proc. IEEE UGIM Symp.*, Jun. 2006, pp. 119-123.

[69] X. Yang and D. K. Schroder, "Some semiconductor device physics considerations and clarifications," *IEEE Trans. Electron Devices*, vol. 59, no. 7, pp. 1993–1996, Jul. 2012.

[70] Y. Tsividis, *Operation and Modeling of the MOS Transistor*. New York, NY, USA: McGraw-Hill, 1999.

On the Implementation of Multi-bit Inexact Adder Cells and Application towards Image De-noising

Srikant Kumar Beura, Amol Arjun Jawale, Bishnulatpam Pushpa Devi, and Prabir Saha

***Abstract*—Inexact computing is an attractive concept for digital signal processing at the submicron regime. This paper proposes 2-bit inexact adder cell and further escalate to 4-bit, and 8-bit inexact adder and error metrics have been evaluated mathematically for such adder cells. The approximated design has been proposed through the simplification of the K-Maps, which leads to a substantial reduction in the propagation delay as well as energy consumption. The proposed design has been verified through the Cadence Spectre and performance parameters (such as delay, power consumption) have been evaluated through CMOS gpdk45 nm technology. Furthermore, the proposed design has been applied to image de-noising application where the performance of the images like Peak Signal to Noise Ratio (PSNR), Normalized Correlation Coefficient (NCC) and Structural Similarity Index (SSIM) has been analyzed through MATLAB, which offer the substantial improvement from its counterpart.**

***Index Terms*—Delay, error metrics,image de-noising, inexact adder.**

Original Research Paper
DOI: 10.7251/ ELS2024033B

I. Introduction

Inexact computing emerged as a promising theory to reduce the net energy consumption of integrated circuits(IC) with a certain amount of accuracy [1]–[2]. However, the stringent accuracy is not required for the applications like image processing, stochastic signal processing, digital modulation technique such as delta modulation, etc., where propagation delay, transistor count, and power consumptions are the premier concept to improve the overall efficiency of such system [3]–[4].

Generally, to realize the hardware architecture of the delta modulation circuitry, which is an important encoding technique in signal processing, requires the circuit component like delta adder/subtractors and multipliers [5]–[6]. However, stochastic computing, which is based on probability, involves a trade-off between accuracy and power, can also be realized through the multiplier and adder as a block. For the digital implementation of such circuitry researchers are utilizing OR gate instead of XOR gate to achieve the efficient circuitry as a result the accuracy has been negotiated [7]–[9].

Moreover, digital signal processors are widely used to process the image and video information. Hence, high speed low power circuits with utmost accuracy for such a processor is the premier concern for the researchers in the present era [10] - [11]. From the last decade, a versatile amount of work [12]- [19] have been reported so far to show the improvements for the performance metrics along-with the accuracy enhancement. A research group headed by Zhu proposed an error-tolerant adder (ETA) in 2010 [12], and in the same year, lower part OR adder (LOA) has been proposed by Mahdiani et al. [13]. Moreover, the above-mentioned adders [7]–[8] have been applied to the FFT processor and soft computing applications respectively. However, both the applications are the error tolerant circuits; thus, error matrices would not be affected so much, which are caused by the aforementioned adders. In 2013 Gupta et al. [14] has designed a low power digital signal processing methodology, where they have proposed five approximate adder cells (AMA). However, all the approximations [9] use a large number of transistors leading to increase the circuit complexity.

Meanwhile, the researcher has optimized the transistor count for the design of an inexact adder (AXA) [15] through pass transistor logic, which also has been derived from ten transistors (10T) precise adder [20]. Without affecting the logic (pass transistor), another three different adder cells have been proposed by Almurib et al. [16]through the alteration of basic gates(InXA).Due to the application of the pass transistor logic transistor count and power consumption has been reduced but does not attain the other premiere parameters like accuracy and voltage swing. Therefore, to recover this voltage swing issue, a pass transistor logic-based inexact adder has been proposed in the literature [17], but still, the accuracy has not been resolved so far. Dutt et al. have proposed four approximate full adders

Manuscript received 25 September 2019. Received in revised form 6 March 2020. Accepted for publication 27 March 2020.

Srikant Kumar Beura is with the Department of Electronics and Communication Engineering, National Institute of Technology Meghalaya, Shillong 793003, India (corresponding author: +91-364-2501294; fax: +91-364-2501113).

Amol Arjun Jawale is with the Department of Electronics and Communication Engineering, National Institute of Technology Meghalaya, Shillong 793003, India (corresponding author: +91-364-2501294; fax: +91-364-2501113).

Bishnulatpam Pushpa Devi is with the Department of Electronics and Communication Engineering, National Institute of Technology Meghalaya, Shillong 793003, India (corresponding author: +91-364-2501294; fax: +91-364-2501113).

Prabir Saha is with the Department of Electronics and Communication Engineering, National Institute of Technology Meghalaya, Shillong 793003, India (corresponding author: +91-364-2501294; fax: +91-364-2501113; e-mail: sahaprabir1@gmail.com).

(AFAs) [18], which reduces the carry propagation chain at the cost of minimal error, and further, they have implemented n-bit adder using the optimal AFA which is referred as ApproxADD. Single bit approximation leads to a poor trade-off between power dissipation and accuracy, thereby, researchers [19] has proposed three numbers of low power, less delay, and area-efficient inexact 2-bit adders, and also the design has been extended to 16-bit. However, power, area, and delay can also be reinvestigated for the betterment of the application prospect.

In this paper, the gate-level design of 2-bit and 4-bit inexact adders (InEMAs) has been proposed. Approximation of such adders has been made through the alteration of some bits followed by the K-map reduction of the precise adder expressions. Furthermore, gate-level optimization has been carried out for the reduction of the transistor count. Error metrics (error rate, mean error distance, normalized mean error distance), circuit matrices functions (power and delay) have been analyzed and compared with existing and implemented adders. The implemented design has been scaled to 8-bit adder for the practical application like image de-noising. With the adaptation of the implemented adder cells, peak signal to noise ratio (PSNR), Normalized Correlation Coefficient (NCC) and Structural Similarity Index (SSIM) has been improved significantly for such imaging application.

The manuscript is organized as follows: (i) Section II gives the brief design of 2-bit, 4-bit, and 8-bit inexact adder; (ii) Section III shows the analysis of error metrics, power, and delay and the comparison with existing approaches; (iii) Section IV demonstrates the application of inexact adders for image de-noising; followed by the conclusion (Section V).

II. Proposed Inexact Adder Architectures

Inexact adders can be designed in two methodologies based on the input length [21], which are inexact 1-bit adder and inexact multi-bit adder. The first methodology leads to less area, reduced power consumption, and small delay at the cost of diminution in accuracy. However, the second design methodology doesn't rely on an approximation of a single bit, which allows the researchers to approximate a portion of an n-bit adder. This results in a significantly low error as compared to the adders designed by the first methodology[19]. The sum output of such block (multi-bit) is calculated by targeting the carry speculation mechanism. This design is based on the idea that when two random inputs are added, it rarely generates a long carry chain. Thereby, multi-bit approximated adders are the usual choice in the present era for the researches.

II.1 2-Bit Exact Adder

The 2-bit exact adder cell is designed by cascading two full adders for generating the outputs [11]. This design takes 5 input combinations $(A1, A0, B1, B0, Cin)$ and generates 3 outputs i.e. $Cout1 Sum1$, and $Sum0$ which are given by eqn. 1, 2 and 3 respectively.

$$Sum0 = A0 \oplus B0 \oplus Cin \quad (1)$$

$$Sum1 = A1 \oplus B1 \oplus Cout0 \quad (2)$$

$$Cout1 = A1.B1 + (A1 \oplus B1)Cout0 \quad (3)$$

Where $Cout0$ is an intermediate output carry of the first full adder (taken from LSB side). To implement a full adder using static CMOS logic required 28 transistors, thus to implement 2-bit adder cell using same logic required 56 transistors. Due to the requirement of a large number of transistors, dynamic power consumption and node capacitances are increased, which leads to a cumulative increase in net energy consumption [10]. The output generated carry using the concatenation of two full adder cells requires 6 stages for output generation, which increases the propagation delay of the overall circuit.

II.2 2-Bit Inexact Adder

The proposed design (InEMA-1) has been shown in Fig. 1, which has been formulated through the 2-bit exact adder equations (1-3). The approximation has been made through the following steps:

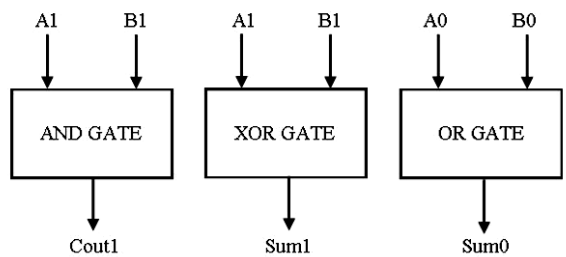

Fig. 1. Block diagram of the Proposed 2-Bit Inexact Adder (InEMA-1)

Step 1: In this Fig. 1 lower significant adder has been replaced by an OR gate. In this architecture (Fig. 1), $Cin$and $Cout$ have been ignored from the design, which offers the reduction of the carry chain from input to output. Therefore, due to the absence of Cin, the first full adder (observation from the LSB side) can be replaced by a half adder with only two inputs$(A0, B0)$. However, to implement the half adder XOR and AND gates are required to produce the Sum and Carry, respectively.

Step 2: Basically, in adders, XOR gates tend to contribute to high delay, area, and power [17,18]. Therefore, for approximating the half-adder, XOR gate of half adder is replaced with OR gate (both are having the equivalent outputs except for logic high inputs) as given by equation (4). Further, the requirement of the number of transistors for the circuit implementation is reduced (through the replacement of XOR gate with OR gate), which leads in the reduction of the dynamic power consumption and node capacitances of the overall circuit.

$$\mathrm{Sum0} = \mathrm{A0} + \mathrm{B0} \quad (4)$$

Step 3: Through the assumption, neither Cin nor$Cout$ is considered; thus, the truth table of a 2-bit adder with 5 inputs and 32 possible combinations can be reduced to 4 inputs and 16 possible combinations, which are shown in Fig. 2. In this Fig. (Fig. 2) the exact truth table for $Sum1$has been shown, which could be approximated through the interchanging of the bits marked with the help of arrow (Fig. 2). Through the approximation, the equation can be reduced to only an XOR gate, which has been given in eqn. 5.

$$\text{Sum1} = \text{A1} \oplus \text{B1} \tag{5}$$

	B1'B0'	B1'B0	B1B0	B1B0'
À1'A0'	0	0	1	1
A1'A0	0	1	0	1
A1A0	1	0	1	0
A1A0'	1	1	0	0

Fig. 2. K-map of Sum1 of 2-Bit Adder

Step 4: The carry out($Cout$) of the half adder is generated by AND gate. Using this concept, as shown in Fig. 1 only AND gate is used in the last stage (observation from LSB side) to generate $Cout1$, which will be used as a carry-in for the higher bit position of exact adder stages. Moreover, an AND gate for $Cout1$ generation gives us only 2 errors in the $Cout1$ of the proposed 2-bit inexact adder design, which has been shown in Table I. In this table (Table I) erroneous output has been noted (✖), and correct output has been indicated by (✓) for the 2-bit inexact adder.To implement the same using static CMOS technology requires only 24 transistors instead of 56.

Step 5: It is observed from the Fig.1 that XOR gate and AND gate have been generating $Sum1$and $Cout1$, respectively. By using Boolean algebra, the expression for $Cout1$and $Sum1$ can be altered, which is shown in eqn. 6 and 7. Now, $Sum1$ requires two NOR gates and one AND gate for the implementation of this expression and the output of the AND gate can be directly taken as $Cout1$. Therefore, Fig. 3(a) shows the reduced gate level diagram and Fig. 3(b) shows the transistor level diagram of the modified proposed 2-bit inexact adder (InEMA-1), where it requires only 20 transistors for the implementation rather than 24 transistors (Fig. 1).

$$Sum1 = \overline{\overline{(A1 + B1)} + (A1.B1)} \tag{6}$$

$$Cout1 = A1.B1 \tag{7}$$

II.3 4-Bit Inexact Adder

4-bit inexact adder (InEMA-2) design has been given in Fig. 4. In this figure (Fig. 4) A [3:0] and B [3:0] are the input functions, whereas Cout3 and Sum [3:0] are the required outputs. The design has been implemented through the cascade combination of two InEMA-1s. One extra AND gate is used in the MSB position to generate the carry out (as a carry-in) for the next stage (if required). In this design, the intermediate carry generation and propagation are also avoided. Therefore, the carry chain is avoided to reduce the carry propagation delay of the circuit. Furthermore, the number of transistors requirement for the implementation of the proposed InEMA-2 can be reduced significantly.

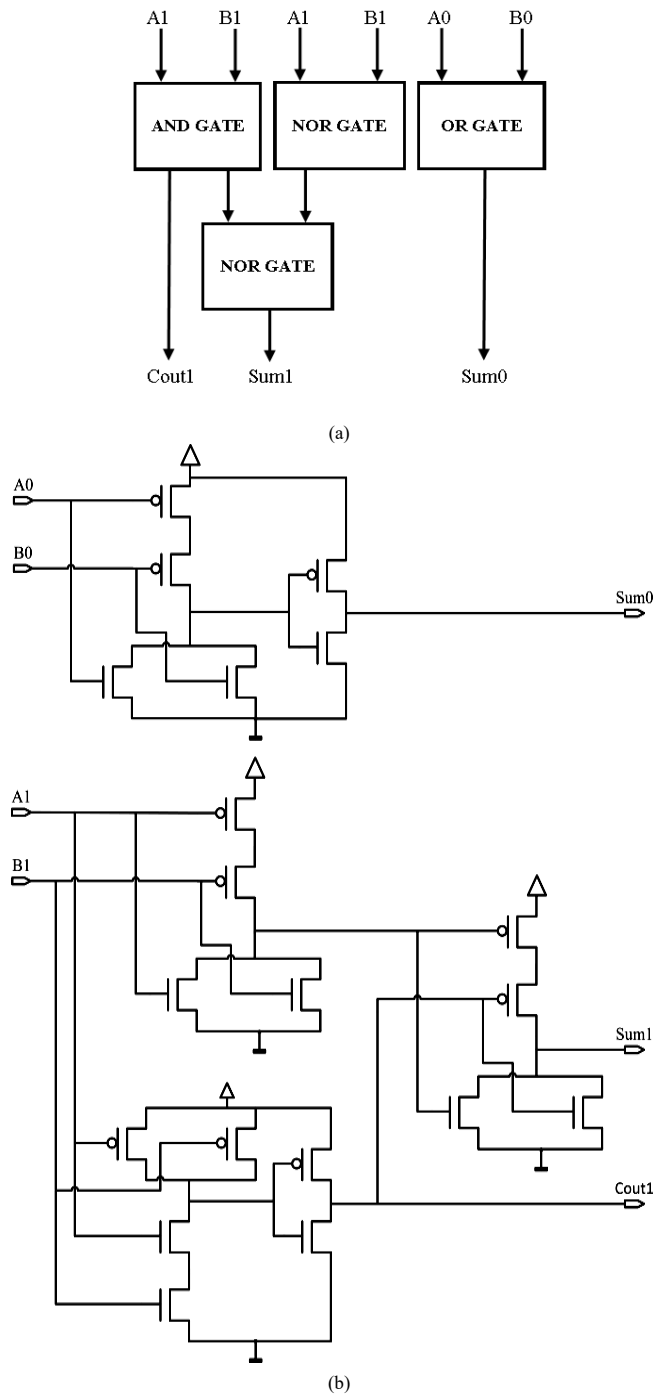

Fig. 3 (a) Block diagram of the modified proposed 2-bit inexact adder, (b) Transistor level diagram of the proposed 2-bit inexact adder,

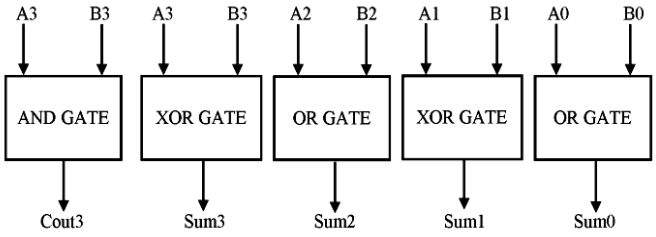

Fig.4 Block diagram of proposed 4-bit inexact adder

TABLE I: TRUTH TABLE OF PROPOSED INEXACT 2-BIT ADDER

Inputs					2-Bit Exact Adder Output For Cin=0			2-Bit Inexact Adder Output For Cin=0		
A1	***A0***	***B1***	***B0***	***Cin***	***Cout1***	***Sum1***	***Sum0***	***Cout1***	***Sum1***	***Sum0***
0	0	0	0	0	0	0	0	0 ✓	0 ✓	0 ✓
0	0	0	1	0	0	0	1	0 ✓	0 ✓	1 ✓
0	0	1	0	0	0	1	0	0 ✓	1 ✓	0 ✓
0	0	1	1	0	0	1	1	0 ✓	1 ✓	1 ✓
0	1	0	0	0	0	0	1	0 ✓	0 ✓	1 ✓
0	1	0	1	0	0	1	0	0 ✓	0 ×	1 ×
0	1	1	0	0	0	1	1	0 ✓	1 ✓	1 ✓
0	1	1	1	0	1	0	0	0 ×	1 ×	1 ×
1	0	0	0	0	0	1	0	0 ✓	1 ✓	0 ✓
1	0	0	1	0	0	1	1	0 ✓	1 ✓	1 ✓
1	0	1	0	0	1	0	0	1 ✓	0 ✓	0 ✓
1	0	1	1	0	1	0	1	1 ✓	0 ✓	1 ✓
1	1	0	0	0	0	1	1	0 ✓	1 ✓	1 ✓
1	1	0	1	0	1	0	0	0 ×	1 ×	1 ×
1	1	1	0	0	1	0	1	1 ✓	0 ✓	1 ✓
1	1	1	1	0	1	1	0	1 ✓	0 ×	1 ×

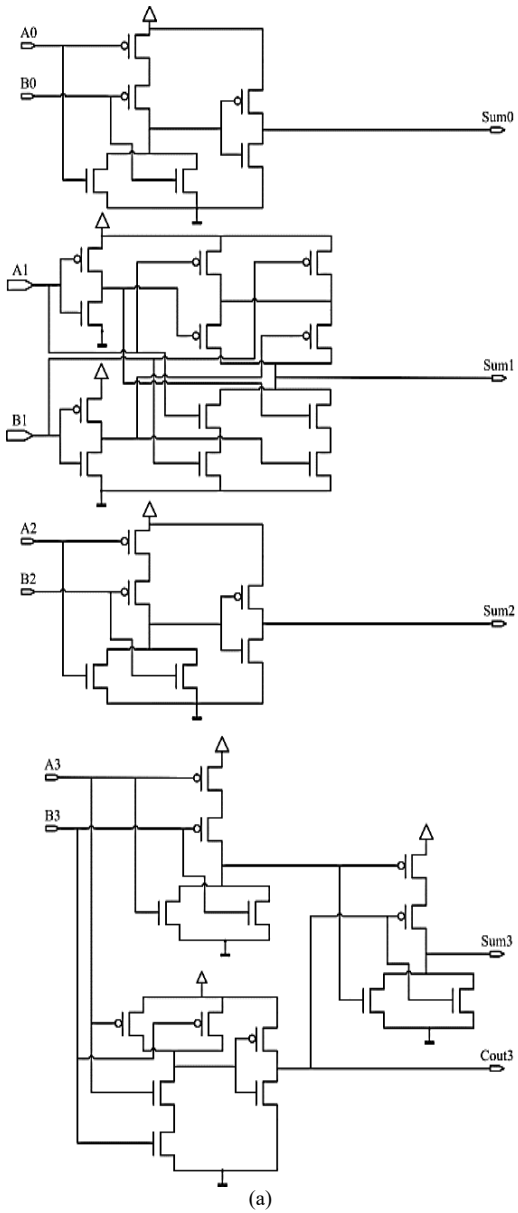

(a)

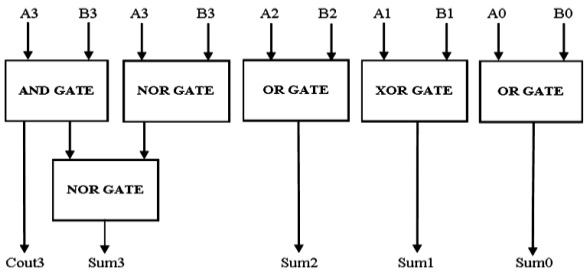

(b)

Fig. 5 (a) Transistor level diagram of the proposed 4-bit inexact adder, (b) Block diagram of modified proposed 4-bit inexact adder

Similar Boolean expressions (eqn. 6, 7) are also applicable for the proposed InEMA-2. As seen from the above diagram (Fig. 4), Cout3 and Sum3 are generated by AND gate and XOR gate, respectively. Furthermore, the transistor count can be reduced by a similar fashion like Fig. 3. Fig. 5(a) and Fig. 5(b) depict the resulting transistor level diagram and the block diagram of the modified InEMA-2, respectively.

II.3 8-Bit Inexact Adder

Fast adders like Carry Look Ahead Adders (CLAs) are mostly used in digital systems. However, CLAs require larger circuitry and dissipate more power as compared to ripple carry adders (RCA). Therefore, 8-bit inexact RCA (InEMA-3) has been proposed and shown in Fig. 6. In this Fig. 6, InEMA-2 adder cell has been put in the LSB side of the 8-bit inexact adder.

Inexact computing gives immense opportunity to introduce error for an error-resilient application. In binary representation, the weight of each bit position is increasing from right to left. So as to reduce the error distance (explained in section 3.1) InEMA-2 replaces four single bit precise full adders in the LSBs of the exact 8-bit RCA instead of MSBs. Due to the use of proposed inexact adders in 8-bit RCA, it is convincingly reducing transistor count and power dissipation. Precise 8-bit RCA requires 224 transistors (using static CMOS logic implementation), whereas the proposed InEMA-3 requires only 150 transistors using the same logic.

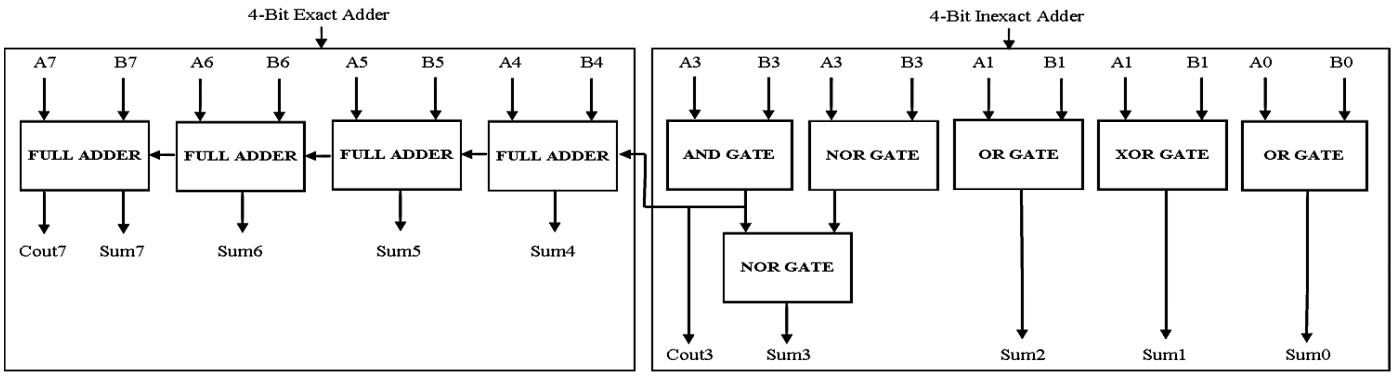

Fig. 6. Block Diagram of Proposed 8-Bit Inexact RCA using 4-Bit Inexact Adder

III. Result and Discussion

III.1 Error Analysis

Gate level design of the proposed adder as well as the reported adder so far [13]–[17], [19] has been coded with Matlab for the calculation of the error matrices. All the possible input combinations between 0 to $2^N - 1$, where N stands for the number of inputs have been considered for the variations, and the output has been observed. The output of the inexact adder has been compared with the output of the exact adder, and the error metrics have been examined. These error matrices can give us an idea about the accuracy of the proposed circuit. The following performance metrics for error analysis (as defined in [16]) have been evaluated for the comparison:

1. Error Distance (ED):

For these inexact designs, a metric has been used to evaluate the inexactness with respect to the exact result; the so-called error distance has been proposed in [23] as a figure of merit for inexact computing. For a given input, the *error distance* (ED)is defined as the arithmetic difference between the exact result (E) and the inexact result (I).

$$ED\ (E,I) = |\ E - I\ | = \left|\sum_i E[i] * 2^i - \sum_j I[j] * 2^j\right| \qquad (8)$$

Where *i* and *j* are the indices for the bits in E and I, respectively.

2. Error Rate (ER):

ER is characterized as the level of incorrect yields among all yields.

$$ER = \frac{Total\ Number\ of\ Erroneous\ Output}{Total\ Number\ of\ Outputs}\ X\ 100 \qquad (9)$$

3. Total Error Distance (TED):

It is the absolute sum of error distance.

$$TED\ = |\ \Sigma\ ED\ | \qquad (10)$$

4. Mean Error Distance (MED):

MED is the average for a set of outputs.

$$MED\ = \frac{Total\ Error\ Distance}{Total\ Number\ of\ Outputs} \qquad (11)$$

5. Normalized Mean Error Distance (NMED):

NMED is the normalized value of MED.

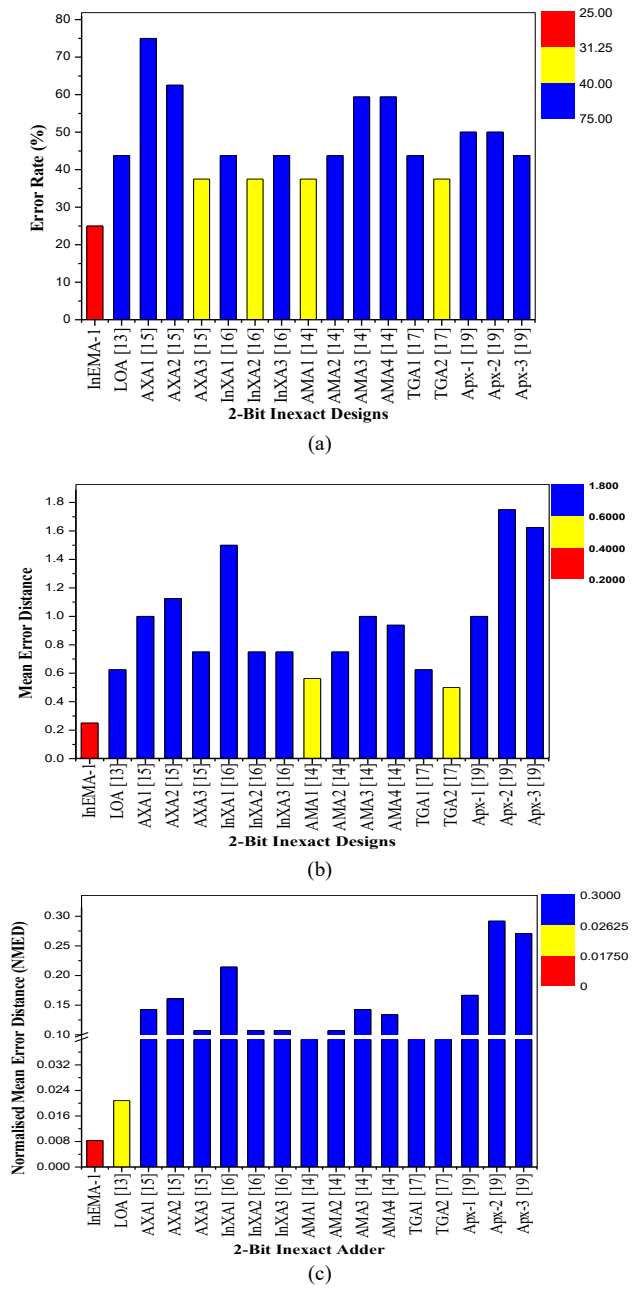

Fig. 7. (a) Error Rate, (b) MED, (c) NMED of proposed& existing inexact adders

$$NMED = \frac{MED}{S_{max}} \quad (12)$$

Smax: It is the maximum magnitude of the output value of the precise adder.

III.1.1 Error Analysis of 2-Bit Inexact Adder (InEMA-1)

In this context, the existing single bit inexact adders [13]–[17] are concatenated to make 2-bit inexact adder for the error analysis with the InEMA-1 adder cell. The error analysis results of the InEMA-1 adder cell with other inexact designs are provided in Fig. 7.

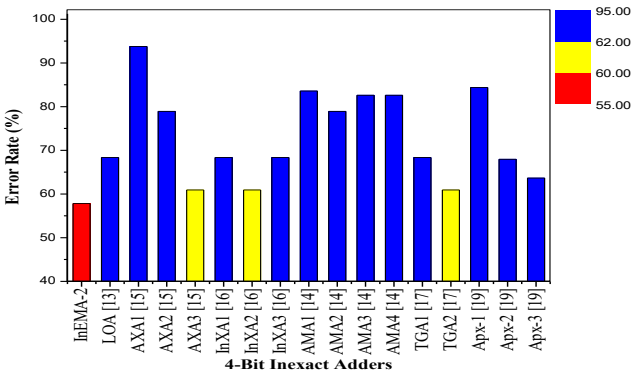

(a)

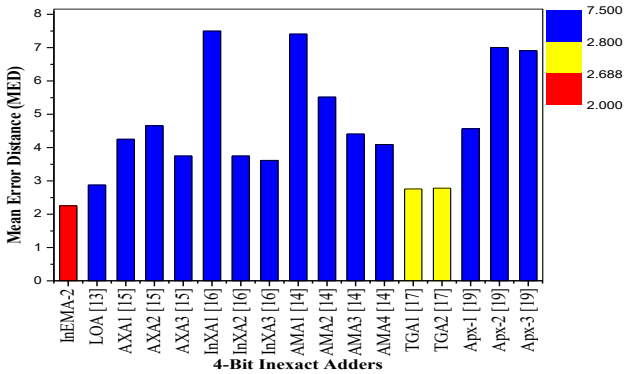

(b)

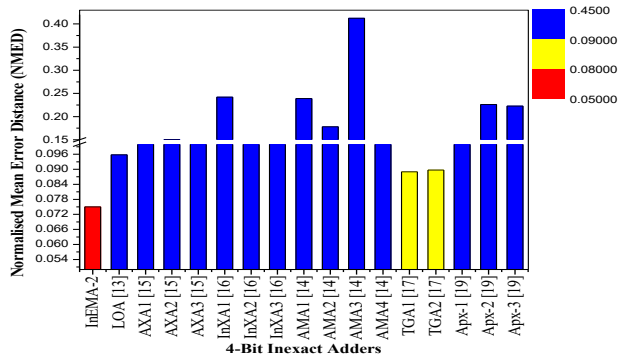

(c)

Fig. 8. (a) ER, (b) MED, (c) NMED of 4-Bit Proposed & Existing Inexact Adders

The error rate of adder cells has been clustered into several groups shown in Fig. 7(a). From the Fig. 7(a) it has been observed that error rate of the [14], [15], [16], [17] are falls in one category (marked in yellow in Fig. 7(a)) which has been considered for the comparison. The error rate which is shown in blue cluster (Fig. 7(a)) is not considered for comparison due to the higher error rate. The error rate of the proposed InEMA-1 (marked in red in Fig. 7(a)) has been reduced by ~12.5% compared with the best reported architectures [14], [15], [16], [17].

MED and NMED have been calculated for the existing and proposed InEMA-1 adder. As shown in Fig. 7 (b) MED of the proposed design (marked in red in Fig. 7(b)) have been reduced by 50%from the best-reported architectures[14], [17](marked in yellow in Fig. 7(b)) and NMED of the proposed InEMA-1 (marked in red in Fig. 7(c)) have been reduced by12.5% from the existing best design [13] (marked in yellow in Fig. 7(c)). The blue clusters [Fig. 7(b) and 7 (c)] have not considered for comparison due to the higher MED and NMED respectively.

III.1.2 Error Analysis of 4-Bit Inexact Adder (InEMA-2)

In 4-bit configuration, the error analysis has been performed between the proposed InEMA-2 adder and the existing inexact adders. Existing 1-bit inexact adders are concatenated to form a 4-bit inexact adder, and then error analysis is performed in MATLAB. Fig. 8 shows the analysis of error metrics between the proposed InEMA-2 adders and the cascaded 4-bit inexact designs.

From Fig. 8(a), it has been observed that error rate of [15], [16], [17] are falls in one category (marked in yellow in Fig. 8(a)), which has been considered for the comparison. The error rate of the proposed InEMA-2(marked in red in Fig. 8(a)) has been shown ~6.5% improvement as compared with the best reported architectures[15], [16], [17].

Similarly, Fig 8 (b, c) has been shown that the proposed InEMA-2 (marked in red in Fig. 8(b, c))have an appreciable reduction of MED and NMED over [17](marked in yellow in Fig. 8(b, c)) respectively. Like as Fig. 7 the blue clusters cells have not considered for comparison due to the higher error matrices.

III.1.3 Error Analysis of 8-Bit Inexact Adder (InEMA-3)

Four number of exact single bit Full Adders in the LSBs of the precise 8-bit RCA is being replaced by the proposed InEMA-2 adder cell to form InEMA-3 as discussed in section 2.4. Existing single bit inexact adders are being concatenated to form 4-bit inexact adder. Similarly, four precise single-bit full adders in the LSBs of the 8-bit exact RCA are replaced by the concatenated 4-bit inexact adders to form 8-bit inexact RCA. The simulation for the proposed 8-bit inexact RCA and existing 8-bit inexact RCAs are presented in this context. The results are shown in Fig. 9.

The error rate of adder cells has been grouped into three groups as shown in Fig. 9(a). From the Fig. 9(a) it has been observed that error rate of the [15], [16], [17] are falls in one category (marked in yellow in Fig. 9(a)) which has been considered for the comparison. The error rate of the proposed InEMA-3 (marked in red in Fig. 9(a)) has been improved by ~7.5% as compared with the best reported architectures [15], [16], [17].

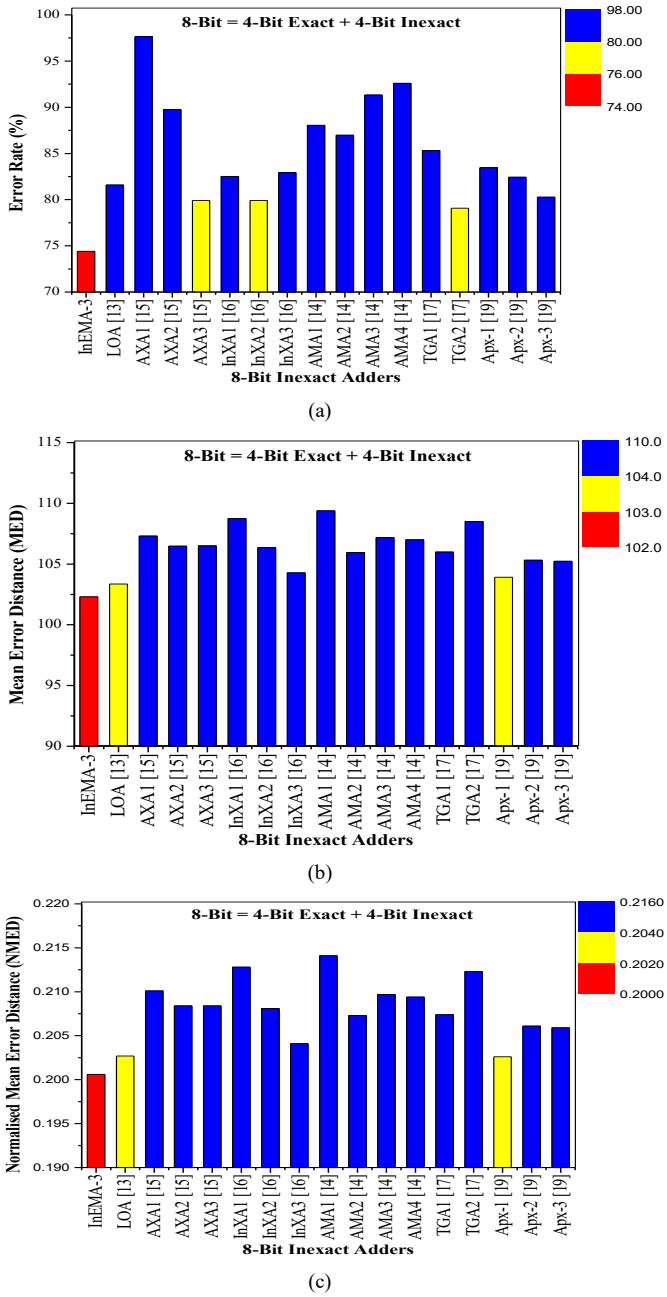

Fig. 9. (a) ER, (b) MED, (c) NMED of 8-Bit Proposed & Existing Inexact Adders

Similarly, from Fig. 9 (b,c) it has been observed that [13], [19] (marked in yellow in Fig. 9(b, c)) has least MED and NMED. Thereby, the comparison has been done with the proposed InEMA-3 (marked in red in Fig. 9 (b, c)) and observed the betterment from its counterpart.

III.2 Power, Delay and Power Delay Product (PDP) Calculation

Moreover, as a circuit design prospect, the proposed design has been implemented in Cadence. The designs have been taken from different references and the same has been implemented in the same environment for the fair comparison. The circuit parameters like power and delay are extracted in Cadence Spectre using gpdk45 nm technology. For the analysis of multi-bit approximation, we have to create exact models of the existing adder circuits. As discussed in section 3.1.3, the proposed InEMA-3 adder cell is utilized for the analysis of performance parameters and compared with its counterpart.

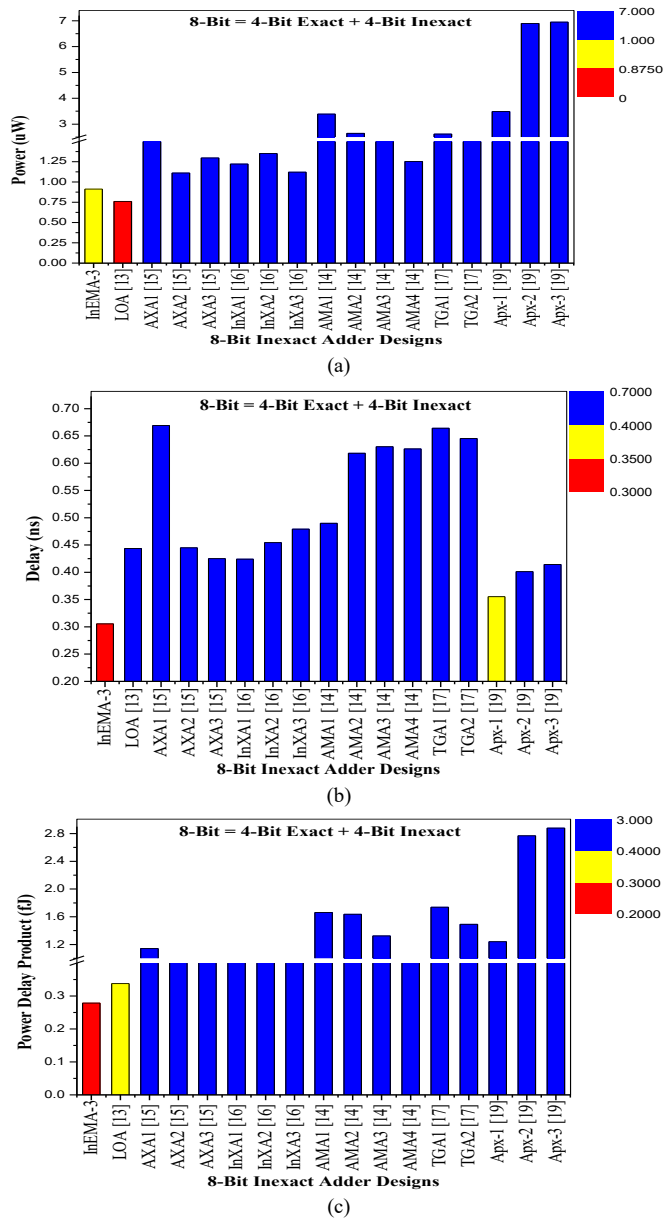

Fig. 10. (a) Power, (b) Delay, (c) PDP of 8-Bit Proposed & Existing Inexact Adders

Power consumption analysis of the proposed and the existing approximate adders has been shown in Fig. 10 (a). To this analysis it has been observed that the reported architecture in [13](marked in red in Fig. 10(a)) dissipate least average power of 760.6nW followed by the proposed InEMA-3 RCA(marked in yellow in Fig. 10 (a)), which consumes an average power of 912.5nW. However, the proposed InEMA-3 RCA (marked in red in Fig. 10(b)) consuming least propagation delay of 0.355ns than other reported work including [13]. It has been observed that

the proposed architecture has least propagation delay followed by[19] (marked in yellow in Fig. 10 (b)). Furthermore, Fig. 10(c) depicted that the proposed InEMA-3 RCA(marked in red in Fig. 10 (c)) has been shown the lowest PDP (0.279fJ) followed by [13] (0.339fJ) (marked in yellow in Fig. 10 (c)).

IV. Application of Inexact Adders in Image De-noising and Image Addition

The performance of the inexact adder cells can be evaluated through image processing applications like image de-noising, image compression, image addition, image sharpening, etc. Therefore, to check the improvement of the results, the researcher have reported in their research [14], [16]–[18]. Researchers in [16] has been added Lena and Tulip images to generate a new image, where, the inexact adder [14] has been applied. Moreover, image sharpening application has been performed in [17], where, multiplication operation has been carried out by carry save adder followed by RCA. The researchers of [14], [18] performed image compression and decompression with the help discrete cosine transformation (DCT) and inverse DCT respectively. The hardware realization of such (DCT and IDCT) requires adder. The researchers [12], [16] have replaced the reported inexact adder [12], [16] to check the effectiveness of the same. In this article, the analysis of image de-noising has been carried out in depth and image addition figure has been provided for comparison. To check the improvement of the proposed inexact multi-bit adder, the existing multi-bit inexact adder[19] has been considered for the comparison.

$$\frac{1}{16} \times \begin{bmatrix} 1 & 2 & 1 \\ 2 & 4 & 2 \\ 1 & 2 & 1 \end{bmatrix}$$

Fig. 11. 3x3 Kernel for weighted averaging filter

To verify the improvement of the proposed inexact adder cell, the image de-noising application has been used. In this task, a noisy image has been generated by adding salt and pepper noise with a density function of 0.03to the original 128 ×128 size Lena image. To remove the noise, a weighted averaging filter of 3×3 kernel (shown in Fig. 11) has been utilized, which has been convolved with the noisy image.

To perform the convolution operation adders and multipliers are required, which can be obtained through the proposed inexact adder and exact multiplier [24] respectively. The 16-bit precise adder in theconvolution operation has been replaced by the proposed InEMA-3 adder. InEMA-3 is an 8-bit adder, which has been extended to 16-bit; one 8-bit exact RCA has been added to the MSB side of the InEMA-3. Finally, the following parameters like peak signal to noise ratio (PSNR), normalized correlation coefficient (NCC), structural similarity index metric(SSIM): have been evaluated and compared with best-reported results reported so far [19].

IV.1 Peak Signal to Noise Ratio (PSNR)

The peak signal to noise ratio (PSNR),is used as a quality metric between two images and mathematical formula of the same is shown in eqn. 13, where R is the maximum fluctuation in the input image data type and mean square error (MSE) represents the cumulative squared error between the original image and the reconstructed image. This ratio is used as a quality measurement between the original and a reconstructed image. The image quality is directly proportional to the value of PSNR. Fig. 12 shows the results of the image de-noising application which have been carried out through existing [19] and proposed adders. The result offers a significant amount of improvement in PSNR, which has shown in Fig. 13.

$$PSNR = 10log_{10}(\frac{R^2}{MSE}) \quad (13)$$

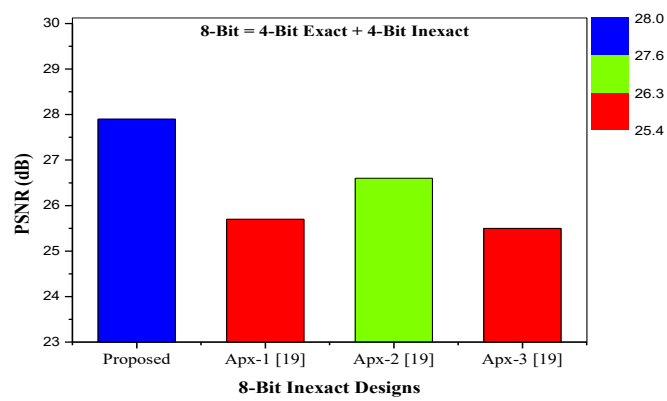

Fig. 13. PSNR values for the proposed and existing multi-bit adders

IV.2 Normalized Correlation Coefficient (NCC)

Normalized Correlation Coefficient (NCC) is also a quality metric, used to measure matching of images, where area-based spatial filtering technique for correlation has been utilized [25]. The mathematical formulation for the same is given in eqn. 14.

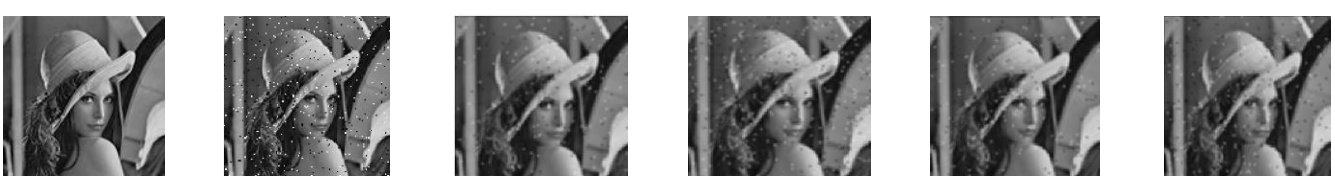

Original Image Noisy Image Proposed Apx-1[19] Apx-2 [19] Apx-3 [19]

Fig. 12. Image De-noising Results

where 'A' is the exact image, whereas 'B' is the distorted image, complement of A and B is the mean value of the exact and distorted images respectively.

The NCC values for the proposed and existing multi-bit adders are shown in Fig. 14.

$$NCC = \frac{\sum_m \sum_n (A_{mn}-\bar{A})(B_{mn}-\bar{B})}{\sqrt{(\sum_m \sum_n (A_{mn}-\bar{A})^2)(\sum_m \sum_n (B_{mn}-\bar{B})^2)}} \quad (14)$$

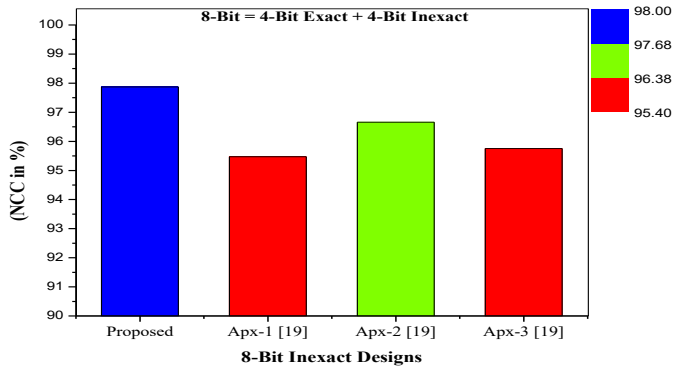

Fig. 14. NCC values for the proposed and existing multi-bit adders

IV.3 Structural Similarity Index Metric(SSIM)

The structural similarity between the two images is determined by the Structural Similarity Index Metric. The reference image should be a non-processed, distortion-free image. The processed image might have random noise, or Gaussian noise, or salt and pepper noise. The SSIM index is preferred over mean squared error (MSE) and PSNR error due to less complex nature. The PSNR and MSE are an absolute error based approach, whereas the structural similarity index is a perception-based approach. The name itself clears that the approach is a structural based approach in which each pixel has a dependency on nearby pixels. The result of SSIM lies between -1 and 1, if both the images are nearly the same, then the SSIM will be near about 1, and if the image difference is larger, SSIM might be less than 0. The 0 value indicates that there is no structural similarity between the two images.

The SSIM is given by eqn. 15, represented in terms of the mean value of the original (μ_x) and distorted signal (μ_y), and the standard deviation of the original (σ_x) and distorted signal (σ_y), and the simulated result has been given in Fig. 15.

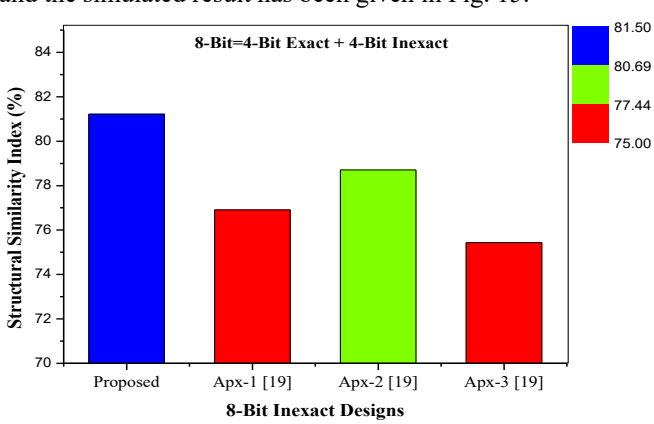

Fig. 15. SSIM values for the proposed and existing multi-bit adders

$$SSIM(x,y) = \frac{(2\mu_x\mu_y + c_1)(2\sigma_{xy} + c_2)}{(\mu_x^2 + \mu_y^2 + c_1)(\sigma_x^2 + \sigma_y^2 + c_2)} \quad (15)$$

IV.4 Image Addition

In this task, Apple and Lena images are considered for the image addition. Both the images are of 128x128 sizes. The addition operation performed here is pixel by pixel, where each of the pixels contains a decimal value in between 0 to 255. This decimal value is converted to 8-bit binary and given to the exact and inexact 8-bit RCA for addition. The summation result is again converted back to decimal. The exact addition and inexact addition result has been provided in Fig. 16.

Fig. 16. Image Addition Results

V. Conclusions

In this manuscript, multi-bit adders viz. 2-bit and 4-bit approximation technique has been demonstrated. Moreover, the 4-bit inexact adder has been utilized in higher dimension adder (8-bit inexact) to express the advantages of such reported approach. Error metrics and circuit performance parameters have been calculated for further applications. Furthermore, in application prospect, the reported adder has been utilized in image de-noising application and examines the improvement from its counterpart. It would be a welcome approach for the researcher, to check betterment of the proposed adder cells in discrete signal processing applications.

References

[1] J. Han and M. Orshansky, "Approximate computing: An emerging paradigm for energy-efficient design," in *2013 18TH IEEE EUROPEAN TEST SYMPOSIUM (ETS)*, Avignon, France, 2013, pp. 1–6, doi: 10.1109/ETS.2013.6569370.

[2] K. Roy and A. Raghunathan, "Approximate Computing: An Energy-Efficient Computing Technique for Error Resilient Applications," in *2015 IEEE Computer Society Annual Symposium on VLSI*, 2015, pp. 473–475, doi: 10.1109/ISVLSI.2015.130.

[3] S. Mittal, "A Survey of Techniques for Approximate Computing," *ACM Comput Surv*, vol. 48, no. 4, pp. 62:1–62:33, Mar. 2016, doi: 10.1145/2893356.

[4] V. K. Chippa, S. Venkataramani, S. T. Chakradhar, K. Roy, and A. Raghunathan, "Approximate computing: An integrated hardware approach," in *2013 Asilomar Conference on Signals, Systems and Computers*, 2013, pp. 111–117, doi: 10.1109/ACSSC.2013.6810241.

[5] N. Kouvaras, "Operations on delta-modulated signals and their application in the realization of digital filters," *Radio Electron. Eng.*, vol. 48, no. 9, pp. 431–438, Sep. 1978, doi: 10.1049/ree.1978.0062.

[6] S. H. Nawab, A. V. Oppenheim, A. P. Chandrakasan, J. M. Winograd, and J. T. Ludwig, "Approximate Signal Processing," p. 24, 1997.

[7] D. Zrilic and N. Pjevalica, "Stochastic signal processing using delta-sigma modulation," in *Proceedings of the 5th Biannual World Automation Congress*, 2002, vol. 14, pp. 653–658, doi: 10.1109/WAC.2002.1049509.

[8] W. J. Poppelbaum, C. Afuso, and J. W. Esch, "Stochastic computing elements and systems," in *Proceedings of the November 14-16, 1967, fall joint computer conference on - AFIPS '67 (Fall)*, Anaheim, California, 1967, p. 635, doi: 10.1145/1465611.1465696.

[9] B. R. Gaines, "Stochastic Computing Systems," in *Advances in Information Systems Science: Volume 2*, J. T. Tou, Ed. Boston, MA: Springer US, 1969, pp. 37–172.

[10] V. Gupta, D. Mohapatra, S. P. Park, A. Raghunathan, and K. Roy, "IMPACT: IMPrecise adders for low-power approximate computing," in *IEEE/ACM International Symposium on Low Power Electronics and Design*, Fukuoka, Japan, 2011, pp. 409–414, doi: 10.1109/ISLPED.2011.5993675.

[11] Y. Kim, Y. Zhang, and P. Li, "Energy Efficient Approximate Arithmetic for Error Resilient Neuromorphic Computing," *IEEE Trans. Very Large Scale Integr. VLSI Syst.*, vol. 23, no. 11, pp. 2733–2737, Nov. 2015, doi: 10.1109/TVLSI.2014.2365458.

[12] Ning Zhu, Wang Ling Goh, Weija Zhang, Kiat Seng Yeo, and Zhi Hui Kong, "Design of Low-Power High-Speed Truncation-Error-Tolerant Adder and Its Application in Digital Signal Processing," *IEEE Trans. Very Large Scale Integr. VLSI Syst.*, vol. 18, no. 8, pp. 1225–1229, Aug. 2010, doi: 10.1109/TVLSI.2009.2020591.

[13] H. R. Mahdiani, A. Ahmadi, S. M. Fakhraie, and C. Lucas, "Bio-Inspired Imprecise Computational Blocks for Efficient VLSI Implementation of Soft-Computing Applications," *IEEE Trans. Circuits Syst. Regul. Pap.*, vol. 57, no. 4, pp. 850–862, Apr. 2010, doi: 10.1109/TCSI.2009.2027626.

[14] V. Gupta, D. Mohapatra, A. Raghunathan, and K. Roy, "Low-Power Digital Signal Processing Using Approximate Adders," *IEEE Trans. Comput.-Aided Des. Integr. Circuits Syst.*, vol. 32, no. 1, pp. 124–137, Jan. 2013, doi: 10.1109/TCAD.2012.2217962.

[15] Z. Yang, A. Jain, J. Liang, J. Han, and F. Lombardi, "Approximate XOR/XNOR-based adders for inexact computing," in *2013 13th IEEE International Conference on Nanotechnology (IEEE-NANO 2013)*, Beijing, China, 2013, pp. 690–693, doi: 10.1109/NANO.2013.6720793

[16] H. A. F. Almurib, T. N. Kumar, and F. Lombardi, "Inexact Designs for Approximate Low Power Addition by Cell Replacement," in *Proceedings of the 2016 Design, Automation & Test in Europe Conference & Exhibition (DATE)*, 2016, pp. 660–665, doi: 10.3850/9783981537079_0042.

[17] Z. Yang, J. Han, and F. Lombardi, "Transmission gate-based approximate adders for inexact computing," in *Proceedings of the 2015 IEEE/ACM International Symposium on Nanoscale Architectures (NANOARCH´15)*, Boston, MA, USA, 2015, pp. 145–150, doi: 10.1109/NANOARCH.2015.7180603.

[18] S. Dutt, S. Nandi, and G. Trivedi, "Analysis and Design of Adders for Approximate Computing," *ACM Trans Embed Comput Syst*, vol. 17, no. 2, pp. 40:1–40:28, Dec. 2017, doi: 10.1145/3131274.

[19] S. Tajasob, M. Rezaalipour, and M. Dehyadegari, "Designing energy-efficient imprecise adders with multi-bit approximation," *Microelectron. J.*, vol. 89, pp. 41–55, Jul. 2019, doi: 10.1016/j.mejo.2019.04.002.

[20] J.-F. Lin, Y.-T. Hwang, M.-H. Sheu, and C.-C. Ho, "A Novel High-Speed and Energy Efficient 10-Transistor Full Adder Design," *IEEE Trans. Circuits Syst. Regul. Pap.*, vol. 54, no. 5, pp. 1050–1059, May 2007, doi: 10.1109/TCSI.2007.895509.

[21] Y. Wu, Y. Li, X. Ge, Y. Gao, and W. Qian, "An Efficient Method for Calculating the Error Statistics of Block-Based Approximate Adders," *IEEE Trans. Comput.*, vol. 68, no. 1, pp. 21–38, Jan. 2019, doi: 10.1109/TC.2018.2859960.

[22] S. Venkatachalam and S. Ko, "Design of Power and Area Efficient Approximate Multipliers," *IEEE Trans. Very Large Scale Integr. VLSI Syst.*, vol. 25, no. 5, pp. 1782–1786, May 2017, doi: 10.1109/TVLSI.2016.2643639.

[23] J. Liang, J. Han, and F. Lombardi, "New Metrics for the Reliability of Approximate and Probabilistic Adders," *IEEE Trans. Comput.*, vol. 62, no. 9, pp. 1760–1771, Sep. 2013, doi: 10.1109/TC.2012.146.

[24] A. Habibi and P. A. Wintz, "Fast Multipliers," *IEEE Trans. Comput.*, vol. C–19, no. 2, pp. 153–157, Feb. 1970, doi: 10.1109/T-C.1970.222881.

[25] B. Zitová and J. Flusser, "Image registration methods: a survey," *Image Vis. Comput.*, vol. 21, no. 11, pp. 977–1000, Oct. 2003, doi: 10.1016/S0262-8856(03)00137-9.

Characteristics of $Zn_{1-x}Al_xO$ NR/ITO Composite Films Oriented Application for Optoelectronic Devices

Nguyen Dinh Lam

***Abstract*— The Zn1-xAlxO nanorod (NR) were grown on ITO substrates by a hydrothermal process. The influences of the Al doping concentration on the surface morphology, structural, optical, and electrical characteristics of the $Zn_{1-x}Al_xO$ NR/ITO composite film were investigated in detail. The results indicated that characteristics of the $Zn_{1-x}Al_xO$ NR/ITO composite film were strongly influenced by the Al doping concentration. Furthermore, the lowest vertical resistance of the $Zn_{1-x}Al_xO$ NR can be obtained when x = 0.01 and it strongly reduces when the concentration of UV light illumination increases. This reduction follows an exponential decay with a decay rate of 4.35. This result shows good photoconductivity response of the $Zn_{1-x}Al_xO$ NR/ITO composite film and its ability to apply for optoelectronic devices material.**

***Index Terms*— $Zn_{1-x}Al_xO$ NR/ITO composite film, Al doping, Optoelectronic devices.**

Original Research Paper
DOI: 10.7251/ELS2024043L

I. Introduction

ZINC oxide (ZnO) is a II-VI semiconductor with attractive characteristics such as a large exciton binding energy of 60 meV and a wide direct bandgap of 3.37 eV [1]-[3]. In application for optoelectronic devices or photocatalytic materials, ZnO material is usually fabricated under one dimension (1D) nanostructures array [4]-[9]. By applying ZnO 1D nanostructure, the performances of solar cell and light emitting diode devices were significantly enhanced compared to that using ZnO film [10]-[11]. This enhancement in the characteristics of these devices was explained due to a higher electrical conductibility and larger effective surface area. Furthermore, optical, structural, and electrical characteristics of the ZnO 1D nanostructures can be also controlled and improved by doping with some kind of materials such as silver, copper, gallium, cerium, yttrium, and etc [12]-[21]. The red-shift in the absorption band of the ZnO nanostructure corresponding to improving the absorption of the photocatalysts was achieved by silver doping [13]-[14]. Besides that, the cerium doped ZnO nanostructure decreased band gap energy from 3.37 eV to 3.18eV, decreased size of nanorods, and increased the green emission peak in photoluminescence spectra [15]-[16]. In addition, Al doped ZnO nanostructures was also enhanced free charge carriers resulting in increasing electrical property [22]-[23]. However, the influences of Al doping concentration on the characteristics of $Zn_{1-x}Al_xO$ nanostructure fabricated under film are still needed further investigation in detail for optoelectronic devices applications.

In this work, wurtzite type $Zn_{1-x}Al_xO$ NR structures were grown on ITO substrates by hydrothermal method (called the $Zn_{1-x}Al_xO$ NR/ITO composite film). Influences of the Al doping concentration on surface morphology, structural, and optical characteristics of the $Zn_{1-x}Al_xO$ NR/ITO composite film were investigated. Furthermore, electrical property of the $Zn_{1-x}Al_xO$ NR/ITO composite film was also evaluated to find out optimized conditions for application in optoelectronic devices fabrication.

II. Experimental Details

The Zn1-xAlxO NR/ITO composite film were fabricated as the following processes. The first step, ITO substrates were immersed in HCl solution for 10 min to remove organic contamination and then cleaned by methanol, and deionized water in sequence. The second step, 0.1 M solution of zinc acetate dehydrate ($Zn(CH_3COO)_2.2H_2O$) was spin coated on the ITO substrates. After the coating process, the zinc acetate dehydrate coated layer on ITO substrates were dried at 150 ^oC for 20 minutes in an oven to evaporate the solvent and remove organic residuals and then annealed at 500 ^oC for 1 h in air environment to create a ZnO seed layer on ITO substrates. The final step, $Zn_{1-x}Al_xO$ NR structures were grown by hydrothermal process with x varied from 0 to 0.03. In this process, ITO substrates with coated ZnO seed layer and 100 mL solution of 20 mM zinc nitrate ($Zn(NO_3)_2.6H_2O$), 5 mM $C_6H_{12}N_4$ and $Al(NO_3)_3.9H_2O$ with various molar concentrations of Al^{3+} (0%, 1%, 2%, and 3% in comparison with molar concentration of Zn^{2+}) were transferred together into Teflon-lined stainless steel autoclave and then baked at 80 ^oC for 2 hours. The growth time, growth temperature, zinc nitrate concentration, and volume of solution were kept as constants. The obtained the $Zn_{1-x}Al_xO$ NR/ITO composite films after growth processes were ultrasonically

Manuscript received 23 December 2019. Received in revised form 1 March 2020. Accepted for publication 4 April 2020.

Nguyen Dinh Lam is with the Faculty of Engineering Physiscs and Nanotechnology, VNU-University of Engineering and Technology, Vietnam National University, Hanoi, Vietnam (phone: +84-902-233-144; email: lamnd2005@gmail.com)

This research is funded b Vietnam National University, Hanoi (VNU) under project number QG.19.20.

cleaned in ethanol and distilled water for 30 min, followed with drying treatment at 100 °C for 1 hours in air environment.

X-ray diffraction patterns of the $Zn_{1-x}Al_xO$ NR/ITO composite film were chartered by an X-Ray Diffractometer (XRD) D5000 with CuKα radiation (λ = 1.5406 Å) at room temperature. The surface morphology of the composite film was observed using a Scanning Electron Microscope (SEM). The optical characteristic of the composite films was studied using an UV–VIS-NIR spectrophotometer in the wavelength range of 300-800 nm at room temperature. The electrical property of the composite films was measured using home-setup system using a Keithley 2000 multimeter and an UV lamp (Hg lamp with a UV bandpass filter).

III. Results And Discussions

SEM images of the $Zn_{1-x}Al_xO$ NR/ITO composite films at various of the Al doping concentrations were shown in Fig. 1.The images show that, $Zn_{1-x}Al_xO$ NRs were of uniform size and have a tendency to become miss oriented perpendicular to the surface of the ITO substrate when the Al doping concentration increases. Furthermore, the diameter, length, and density of the $Zn_{1-x}Al_xO$ nanorod were strongly depended on the Al doping concentrations. The $Zn_{1-x}Al_xO$ NR density dependence was extracted and depicted in Fig.2. This result indicated that, density of the $Zn_{1-x}Al_xO$ nanorod decreases with an increasing of the Al doping concentrations and this reduction follows an exponential function with the decay rate about 0.8. The miss oriented and reduction in $Zn_{1-x}Al_xO$ NR density as increasing of the Al doping concentrations could be attributed to the replacement of bigger Al atoms to Zn position in the crystal lattice.

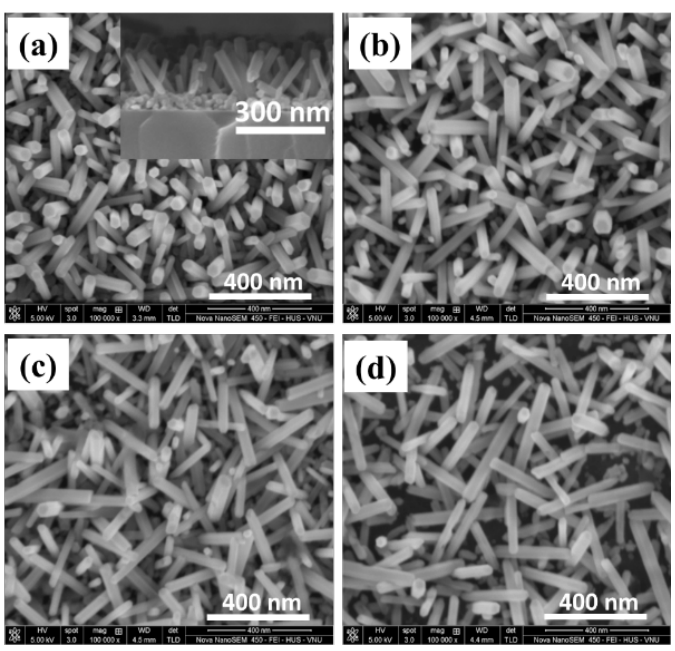

Fig. 1. FE-SEM images of the $Zn_{1-x}Al_xO$ NR/ITO composite films

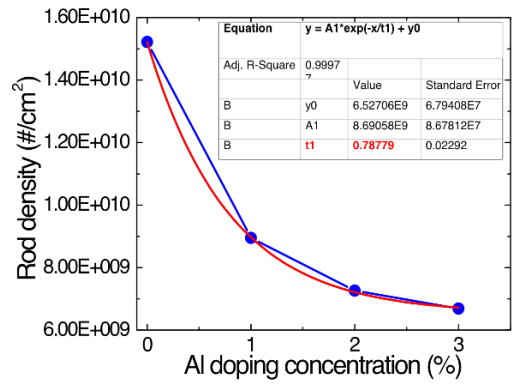

Fig. 2. $Zn_{1-x}Al_xO$ NR density versus the Al doping concentration

The crystal structures of Zn_{1-x}AlxO NR/ITO composite films were characterized by X-ray Diffractometer as shown in Fig.3. All the peaks shown in X-ray diffraction patterns (XRD) were sharp and narrow peaks and closely matched to that of hexagonal wurtzite ZnO structure. Diffraction peaks related to other impurity phases were not observed in the XRD patterns. Furthermore, a small variation of interplaner spacing (dhkl) of Al doped-ZnO from that of ZnO was also observed which implies that aluminum incorporates into ZnO crystal lattice. This means that doping would induce distorted crystal lattice manifested by the displacement of lattice indices. Moreover, the study of the (002) peak intensity also indicated that the ZnO nanorod/ITO structure (x = 0; 0.01) has a preferential orientation along the c-axis. However, when the Al doping concentration increases, this orientation strongly reduces. This is entirely satisfaction with the SEM result as shown in Fig.1. Furthermore, based on the Scherrer's formula of [26], the crystallite size was calculated where d is the crystallite size, λ is the X-ray wavelength (1.54Å), β is the full width at half maximum (FWHM), and θ is the diffraction angle.

$$d = \frac{0.9\lambda}{\beta\, cost} \tag{1}$$

The calculation data indicates that the average grain size was slightly smaller as well as increasing of the Al-doping amount that might be attributed to the substitution of bigger Al atoms at Zn site in the lattice of ZnO [24]-[25].

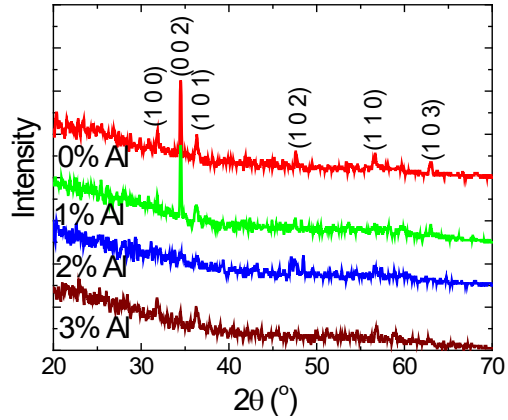

Fig. 3. XRD patterns of the Zn1-xAlxO NR/ITO composite films

According to the diffraction peaks corresponding to planes (1 0 0), (0 0 2), and (1 0 1) the lattice constants were calculated, the results were summarized in table 1.

TABLE I. THE DIMENSIONS OF $Zn_{1-X}AL_xO$ NR STRUCTURE

Sample	FWHM	D(nm)	a(nm)	c(nm)
0% Al	0.488	17.013	0.325	0.523
1% Al	0.368	27.736	0.325	0.520
2% Al	0.410	20.251	0.324	0.521
3% Al	0.443	18.747	0.324	0.520

The influence of the Al doping concentration on the optical characteristics was shown in Fig. 4. The optical transmittance of the $Zn_{1-x}Al_xO$ NR/ITO composite films was slightly depended on the Al doping concentration (Fig. 4.(a)). This can be explained based on the changing of length, density, and orientation of $Zn_{1-x}Al_xO$ NR. However, the optical transmittance of the $Zn_{1-x}Al_xO$ NR/ITO composite films with variation in Al doping concentrations was still higher 95% in visible region with the highest obtained average transmittance of 1% Al doping concentration as shown in Fig. 4.(b). For estimating the band gap energy (Eg) of the $Zn_{1-x}Al_xO$ NR/ITO composite film, the first derivative of the optical transmittance spectra versus wavelength were calculated and presented in Fig. 4.(c). The bandgap energies that correspond to the peaks for all of the structures were extracted and depicted in Fig. 4.(d). The result indicates that the bandgap energy can be slightly enlarged as the higher Al doping concentration. The blue shift of the absorption edge might be attributed to an increase of carrier doping concentration. The doping increases the carrier concentration, when the Zn ions are replaced by Al ions, which may shift the Fermi level leading to widening of bandgap and increase in transmission which called Burstein–Moss effect [27]-[30].

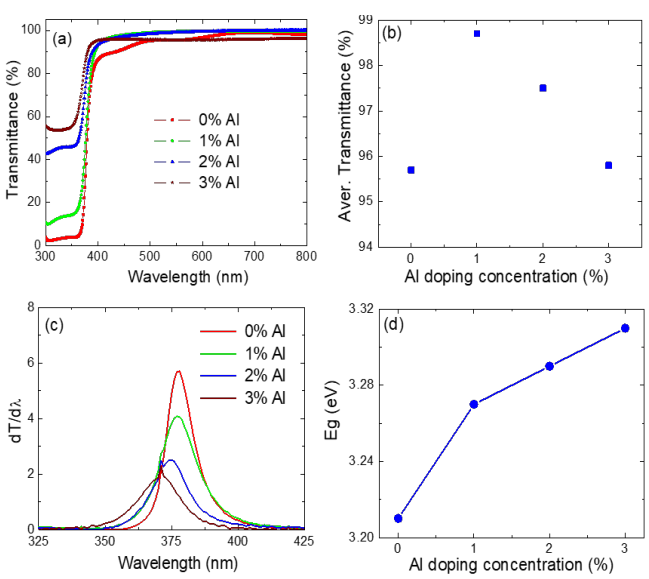

Fig. 4. Optical characteristics of the Zn1-xAlxO NR/ITO composite films

For the electrical property investigation, ITO layer was an electrode. Another electrode was made by silver paste. The I-V characteristics of the $Zn_{1-x}Al_xO$ NR/ITO composite film as shown in Fig. 5 were measured under dark and illuminated by UV lamp. The ohmic and quasi-liner behavior were observed in both of dark and under illumination conditions (Fig. 5.(a, c)). At a given voltage, the current was strongly influenced by the concentration of Al dopant. The highest current was obtained when the Al doping concentration was 1% that resulting in the lowest resistance as shown in Fig. 5.(b). This variation in electrical characteristic of the $Zn_{1-x}Al_xO$ NR/ITO composite film could be attributed to the dependence of NR length, density, and orientation on the Al doping concentration [31]-[33]. The I-V characteristics of the $Zn_{0.99}Al_{0.01}O$ NR/ITO composite film under UV light illumination were measured to find out the photon response of $Zn_{1-x}Al_xO$ NR as shown in Fig. 5.(c). The result indicated that $Zn_{1-x}Al_xO$ NR showed the good photon response when the UV light concentration changes from 0 to 30 mW/cm2. The related resistances were also extracted from Fig. 5.(c) and replotted in Fig. 5.(d). This indicated that the resistance of the $Zn_{1-x}Al_xO$ NR reduces when the UV light concentration increases and following an exponential decay with a decay rate of 4.35. These results indicated that the $Zn_{0.99}Al_{0.01}O$ NR shows good photoconductivity response and its ability to apply for optoelectronic devices material.

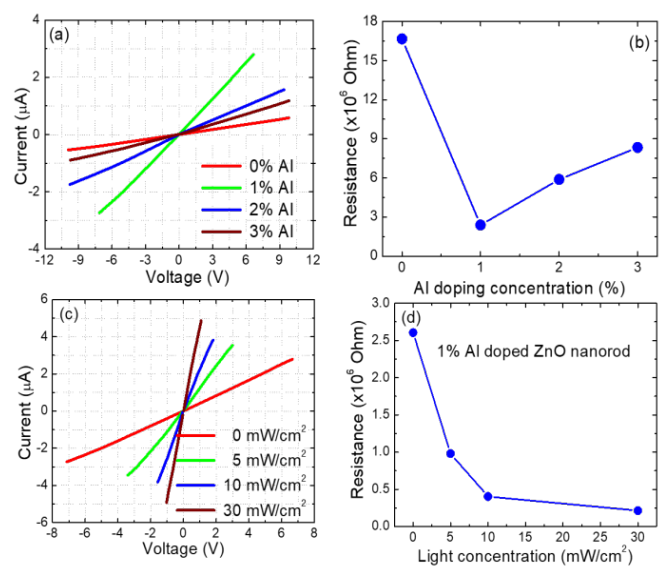

Fig. 5. Electrical characteristics of the Zn1-xAlxO NR/ITO composite films

Based on the NR density as shown in Fig. 2 and electrical characteristics as shown in Fig. 5(b) of the $Zn_{1-x}Al_xO$ samples, the average value of electrical resistance and resistivity of an individual $Zn_{1-x}Al_xO$ NR could be calculated and summarized in Tab. II.

TABLE II. THE AVERAGE VALUE OF ELECTRICAL RESISTANCE AND RESISTIVITY OF AN INDIVIDUAL $Zn_{1-X}AL_xO$ NR

	0% Al	*1% Al*	*2% Al*	*3% Al*
Resistance ($x10^{17}\Omega$)	2.54	0.21	0.43	0.56
Resistivity (Ω.m)	4.25	0.35	0.72	0.92

IV. Conclusion

The influences of the Al doping concentration on the surface morphology, structural, optical, and electrical characteristics of the $Zn_{1-x}Al_xO$ NR/ITO composite films were investigated in detail. When the Al doping concentration increases, the density and orientation along the c-axis of the $Zn_{1-x}Al_xO$ NR were decreased, the bandgap energy was slightly enlarged due to the Burstein–Moss effect. All the $Zn_{1-x}Al_xO$ NR/ITO composite film showed a higher 95% in optical transmittance and the highest of 98.6% was obtained by 1% Al doping concentration. However, the best electrical behavior can be observed by the 1% Al doping concentration. This sample also showed good photoconductivity response and its ability to apply for optoelectronic devices material.

References

[1] Raoufi, D., and Raoufi, T.: "The effect of heat treatment on the physical properties of sol–gel derived ZnO thin films", *Appl Surf Sci*, 2009, 255, pp. 5812–5817

[2] Choppali, U., Kougianos, E., Mohanty, S.P., and Gorman, B.P.: "Polymeric precursor derived nanocrystalline ZnO thin films using EDTA as chelating agent", *Sol. Energy Mater Sol. Cells*, 2010, 94, pp. 2351–2357

[3] Klingshirn, C.: "*ZnO: Material, Physics and Applications*", Chemphyschem., 2007, 8, (6), pp. 782-803

[4] Aravapalli, V., Suresh, M., Jeevanandam, J., Venkatesh, S. K., Gousia, D. P., Balaji, D., and Murthy, N. B.: "Copper-Doped Zinc Oxide Nanoparticles for the Fabrication of white LEDs", *Protection of Metals and Physical Chemistry of Surfaces*, 2019, 55, (3), pp. 481–486

[5] Siddharth, C., Annapoorni, S., and Malik, R.: "Evolution and growth mechanism of hexagonal ZnO nanorods and their LPG sensing response at low operating temperature", *Sensors and Actuators A*, 2019, 293, pp. 207–214

[6] Xing, W., Ran, Y., Ziqiang, J., Tingting, G., Fengni, H., Wei, W., Zifeng, X., and Li, D.: "Cirtopic white LED with a 490 nm emission peak based on He-Zn annealed ZnO nanorods/polymer blend p-n heterojunction", *J. of All. and Comp.*, 2019, 780, pp. 306-311

[7] Mohd, S. A., Hamad A. A., Mahmood, M. S., Zeenat, A., and Sartaj, T.: "Catalytic induced morpholical transformation of porous ZnO to ZnO nanorods by Sn(IV) and their effect on photocatalytic reduction of methylene blue and DFT calculations", *Spectrochimica Acta Part A: Molecular and Biomolecular Spectroscopy*, 2019, 220, pp. 117101

[8] An, K., Kim, J., Afsar. U. M., Rhee, S., Kim, H., Kang, K. T., Young, W. H., and Lee, C.: "Germinant ZnO nanorods as a charge-selective layer in organic solar cells", *Journal of Materials Science and Technology, 2019*, https://doi.org/10.1016/j.jmst.2019.07.027

[9] Dash, P., Manna, A., Mishra, N.C., and Shikha, V.: "Synthesis and characterization of aligned ZnO nanorods for visible light photocatalysis", Physica E: *Low-dimensional Systems and Nanostructures*, 2019, 107, pp. 38-46

[10] Geunchul, P., Soo, M. H., Seung, M. L., Jun, H. C., Keun, M. S., Hyun, Y. K., Hyun-Suk, K., Sung-Jin, E., Seung-Boo, J., Jun, H. L., and Jinho, J.: "Hydrothermally Grown In-doped ZnO Nanorods on p-GaN Films for Color-tunable Heterojunction Light-emitting-diodes", *Scientific Reports*, 2015, 5:10410

[11] Joel, J., Sehoon, C., Patrick, R. B., Jayce, J. C., Paul, H. R., Moungi, G. B., Silvija, G., and Vladimir B.: "ZnO nanowire arrays for enhanced photocurrent in PbS quantum dot solar cells", *Adv. Mater.*, 2013, 25, pp. 2790–2796

[12] Kösemen, A.: "Electrochemical growth of Y doped ZnO nanorods for use in inverted type organic solar cells as electron transport layer", *Mater. Res. Express*, 2019, 6, pp. 095024

[13] Abdus, S., Syed, M. S., and Hazrat, H.: "Band gap tuning and applications of ZnO nanorods in hybrid solar cell: Agdoped verses Nd-doped ZnO nanorods", *Materials Science in Semiconductor Processing*, 2019, 93, pp. 215–225

[14] Hsu, M.H., and Chang, C. J.: "Ag-doped ZnO nanorods coated metal wire meshes as hierarchical photocatalysts with high visible-light driven photoactivity and photostability", *J Hazard Mater.*, 2014, 278, pp. 444-53

[15] Aisah, N., Gustiono, D., Fauzia, V., Sugihartono, I., and Nuryadi, R.: "Synthesis and Enhanced Photocatalytic Activity of Ce-Doped Zinc Oxide Nanorods by Hydrothermal Method*", IOP Conf. Series: Materials Science and Engineering*, 2017, 172, pp. 012037

[16] Sinha, N., Geet, R., Sonia, B., Sanjay, G., Binay, K.: "Synthesis and enhanced properties of cerium doped ZnO nanorods", *Ceramics International, 2014*, 40, (8:A), pp. 12337-12342

[17] Agarwal, D. C., Singh, U. B., Srashti, G., Rahul, S., Kulriya, P. K., Fouran, S., Tripathi, A., Jitendra, S., Joshi U. S., and Avasthi, D. K.: "Enhanced room temperature ferromagnetism and green photoluminescence in Cu doped ZnO thin film synthesised by neutral beam sputtering", *Scientific Reports*, 2019, 9, 6675

[18] Zhou, H., Yang, L., Pengbin, G., Corey, R. G., Zehao, S., Hao, W., and Guojia, F.: "Ga-doped ZnO nanorod scaffold for high-performance, hole-transport-layer-free, self-powered CH3NH3PbI3 perovskite photodetectors", *Solar Energy Materials and Solar Cells*, 2019, 193, pp. 246-252

[19] Goktas, A.: "High-quality solution-based Co and Cu co-doped ZnO nanocrystalline thin films: Comparison of the effects of air and argon annealing environments", *Journal of Alloys and Compounds*, 2018, 735, pp. 2038–2045

[20] Al-Ghamdi, A. A., Al-Hartomy, O. A., El Okr, M., Nawar, A. M., El-Gazzar, S., El-Tantawy, F., and Yakuphanoglu, F.: "Semiconducting properties of Al doped ZnO thin films", *Spectrochimica Acta Part A: Molecular and Biomolecular Spectroscopy*, 2014, 131, pp. 512–517

[21] Tumbul, A., Aslan, F., Demirozu, S., Goktas, A., Kılıç, A., Durgun, M., anf Zarbali, M. Z.: "Solution processed boron doped ZnO thin films: Influence of different boron complexes", *Materials Research Express*, 2018, 6, 035903

[22] Christian, M. P. and Hisao, Y.: "Enhanced Charge Transport in Al-doped ZnO Nanotubes Designed via Simultaneous Etching and Al Doping of H2O-Oxidized ZnO Nanorods for Solar Cell Applications", J. Mater. Chem. C, 2019, DOI: 10.1039/C9TC00401G

[23] Khalid, N.R., Hammad, A., Tahir, M.B., Rafique, M., Iqbal, T., Nabi, G., and Hussain, M.K.: "Enhanced photocatalytic activity of Al and Fe co-doped ZnO nanorods for methylene blue degradation", *Ceramics International*, 2019, https://doi.org/10.1016/j.ceramint.2019.07.132

[24] Yasemin, C., Müjdat, C., and Saliha, I.: "Microstructural, optical and electrical studies on sol gel derived ZnO and ZnO:Al films", *Current Applied Physics*, 2012, 12, pp. 963-968

[25] Jianzi, L., Jian, X., Qingbo, X., and Gang, F.: "Preparation and characterization of Al doped ZnO thin films by sol–gel process*", Journal of Alloys and Compounds*, 2012, 542, pp. 151–156

[26] Mingsong, W., Ka, E. L., Sung, H. H., Eui, J. K., Sunwook, K., Jin, S. C., Eun, W. S., and Chinho, P.: "Optical and photoluminescent properties of sol-gel Al-doped ZnO thin films", *Materials Letters*, 2007, 61, pp. 1118–1121

[27] Shan, F.K., and Yu, Y.S.: "Band gap energy of pure and Al-doped ZnO thin films", *Journal of the European Ceramic Society*, 2004, 24, pp. 1869–1872

[28] Aslan, F., Tumbul, A., Göktaş, A., Budakoğlu, R., and Mutlu, İ. H.: "Growth of ZnO nanorod arrays by one-step sol–gel process", *Journal of Sol-Gel Science and Technology*, 2016, 80, (2), pp. 389–395

[29] Shrisha, B. V., Bhat, S., Kushavah, D., and Gopalakrishna, N.K.: "Hydrothermal growth and characterization of Al-doped ZnO nanorods", *Materials Today: Proceedings*, 2016, 3, (6), pp. 1693–1701

[30] Goktas, A.: "Role of simultaneous substitution of Cu2+ and Mn2+ in ZnS thin films: Defects-induced enhanced room temperature ferromagnetism and photoluminescence", *Physica E: Low-Dimensional Systems and Nanostructures*, 2020, 117, pp. 113828

[31] Gencer, H., Goktas, A., Gunes, M., Mutlu, H. I., and Atalay, S.: "Electrical transport and magnetoresistance properties of $La_{0.67}Ca_{0.33}MnO_3$ film coated on pyrex glass substrate", *Inter. Jour. of Mod. Phys. B*, 2008, 22, (05), pp. 497–506

[32] Gu, X. Q., Zhu, L. P., Cao, L., Ye, Z. Z., He, H. P., and Chu, P. K.: "Optical and electrical properties of ZnO:Al thin films synthesized by low-pressure pulsed laser deposition", *Materials Science in Semiconductor Processing*, 2011, 14 (1), pp. 48–51

[33] Goktas, A., Aslan, F., Yeşilata, B., and Boz, İ.: "Physical properties of solution processable n-type Fe and Al co-doped ZnO nanostructured thin films: Role of Al doping levels and annealing", *Materials Science in Semiconductor Processing*, 2018, 75, pp. 221–233

A Novel Dual Output Schmitt Trigger Using Second Generation Current Controlled Conveyor

Avireni Srinivasulu, Syed Zahiruddin, and Musala Sarada

***Abstract*—Schmitt trigger is designed using the single second generation Current Controlled Conveyor. The proposed configuration utilizes single CCCII and only two externally connected resistors and is able to produce dual output square wave signal. The topology has the benefit of having a simple circuit, offering a large bandwidth and improved slew rate. PSPICE simulator using OrCad 16.3 version, 0.35 µm CMOS technology is used to verify the design, hysteresis is determined and compared with the existing methods available in the literature. The proposed configuration is tested using the experimental setup involving CFOA (AD844AN) and OTA (LM13700). The results have been found satisfactory in both simulation and experimental aspect. Montecarlo analysis and worstcase analysis are determined to prove the circuit efficiency in terms of critical parameters such as resistance with a tolerance of 5%. The hysteresis is also determined, that can reduce the effect of noise, able to produce exact square wave at the output. Schmitt trigger circuits find the applications in the field of Bio medical applications, analog signal processing, communication systems, waveform generators, pulse width modulators, multivibrators, flip-flops and in many other amplifier circuits. The basic application of Schmitt trigger is a square wave generator. The proposed topology is the best suited for monolithic IC fabrication.**

***Index Terms*— CCCII, CFOA, current conveyor, hysteresis, OTA, Schmitt trigger.**

Original Research Paper
DOI: 10.7251/ ELS2024047S

I. Introduction

SCHMITT and Square waveform generators with controllable frequency are widely used circuits in the fields of bio medical applications, instrumentation and measurement [1]-[2]. These serve as interfaces for signal processing, as they offer better electromagnetic interference immunity, lower sensitivity, and has simpler structures compared to harmonic oscillators based on a linear positive feedback structure. Due to these advantages, many relaxation oscillators have been published recently [3]-[11]. The configuration of relaxation oscillator habitually consists of a Schmitt trigger and an integrator in a closed loop. Designers employed various active elements to realize these blocks [5], [8], [9], [12], [13]. Initially operational amplifiers were used, followed by operational transconductance amplifiers (OTAs), second generation current conveyors (CCIIs), differential difference current conveyors (DDCCs), current differencing transconductance amplifiers (CDTAs), differential voltage current conveyor (DVCC), current feedback operational amplifiers (CFOAs) etc., were used to realize waveform generators [12]-[30].

The manuscript presents a novel dual output Schmitt trigger with single current controlled conveyor, with only two resistances and without any capacitance. This makes the circuit attractive for integrated circuit implementation. High-impedance voltage input is used to get accurate, linear, and wideband control of oscillation frequency. High impedance is realized due to the impact of intrinsic resistance that is controlled by the dc bias current. The topology has CCCII as active element which offers the advantages of wider bandwidth, high slew rate, better accuracy and high dynamic range with low supply voltage as compared to the conventional operational amplifiers and other configurations available in the literature.

II. Current Conveyor

A. Current Mode Circuits

For the past few decades, analog designers have trusted current-mode circuits as an essential part of analog circuits. Smith and Sedra had invented the first generation current conveyor (CCI), employing bipolar junction transistors [1], [2], [7]. It has been preferred over the conventional operational amplifiers that were used to realize many applications, but CCI has the limitation of low input impedance. The modified CCI, called as second generation current conveyor (CCII) was introduced by the same duo in 1970. It has high input impedance and preferred in realizing many applications such as oscillators, filters, instrumentation amplifiers and many more. Instead, CCII faces the limitation

Manuscript received 8 January 2020. Received in revised form 22 March 2020 and 28 April 2020. Accepted for publication 13 May 2020.

Avireni Srinivasulu, *Senior Member, IEEE*, was with Vignan's Foundation for Science, Technology and Research (Deemed to be University), Guntur-522213, Andhra Pradesh (State) India. He is now with the Department of Electronics and Communication Engineering, JECRC University, Jaipur-303905, Rajasthan, INDIA. (e-mail: avireni@jecrcu.edu.in (or) avireni@bitmesra.ac.in).

Syed Zahiruddin is with the Department of Electronics and Communication Engineering, Vignan's Foundation for Science, Technology and Research (Deemed to be University), Guntur-522213, Andhra Pradesh (State), INDIA (e-mail: zaheer.usk@gmail.com).

Musala Sarada is with the Department of Electronics and Communication Engineering, Vignan's Foundation for Science, Technology and Research (Deemed to be University), Guntur-522213, Andhra Pradesh (State), INDIA (e-mail: sarada.marasu@gmail.com).

of lack of electronic tunability. CCCII, a series of CCII, is a three terminal device with two input ports X and Y and output port Z and has the intrinsic resistance at input port X which is current controlled. Thus, it has introduced the concept of Current Controlled Conveyor (CCCII) [4], [6], [9].

B. Second Generation Current Controlled Conveyor (CCCII)

Originally, CCCII is the current mode active structural element and possess mixed translinear loop that has considerable amount of intrinsic resistance (R_B) at the input node X. It is varied by tuning the external bias current (I_B).

The ideal characteristics of CCCII, involving the intrinsic resistance (R_B) is portrayed in the below matrix.

$$\begin{bmatrix} I_Y \\ V_X \\ I_Z \end{bmatrix} = \begin{bmatrix} 0 & 0 & 0 \\ 1 & R_B & 0 \\ 0 & \pm 1 & 0 \end{bmatrix} \begin{bmatrix} V_Y \\ I_X \\ V_Z \end{bmatrix} \tag{1}$$

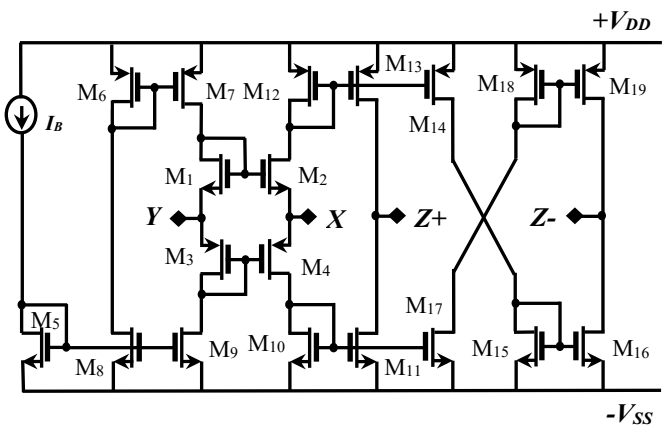

Fig. 1. Internal composition of CCCII±

CCCII is a three port device, two input terminals X and Y along with an output terminal Z. The device is characterized by $I_Y = 0$, $V_X = V_Y + R_B.I_X$ and $I_Z = \pm I_X$, shown in the matrix form in (1). From (1), if the direction of current at input port X and output port Z are same, it is called a positive current conveyor (CCCII+). If the direction of current is opposite to each other then it is a negative current conveyor (CCCII-) [1], [2]. The device has an infinite input impedance at terminal Y and Z, whereas, the input terminal X has intrinsic resistance R_B which is altered by the external bias current I_B, given as:

$$R_B = \frac{1}{g_{m2} + g_{m4}} \tag{2}$$

where g_{mi} is the transconductance of the MOS transistor, presuming that both the transistors are matched, $g_{m2} = g_{m4}$, then:

$$R_B = \frac{1}{\sqrt{8\mu C_{OX}\left(\frac{W}{L}\right) \quad I_B}} \tag{3}$$

where μ signifies the surface mobility, C_{OX} denote the oxide capacitance, W and L are the channel width and length of the MOS transistors (M_2 and M_4) respectively. The schematic of CCCII is realized with MOS transistors, and shown in Fig. 2. The circuit is composed of translinear loop implying that transistors M_1 to M_4, DC biased by using the current mirrors M_6-M_7 and M_8-M_9. The input current I_X is duplicated to produce I_Z using the current mirrors M_{10}-M_{11} and M_{12}-M_{13}. The current is reflected using additional current mirrors M_{14}-M_{19}.

Several applications are presented by applying bias current to the CCCII [20]-[34]. Fig. 1 shows the symbol of CCCII.

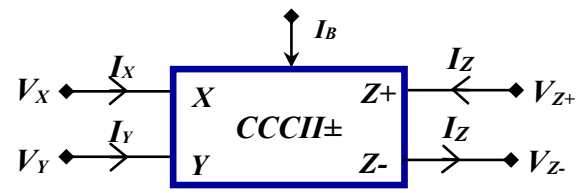

Fig. 2. Symbol of CCCII

III. Schmitt Trigger Using CCCII

Fig. 3 shows the proposed Schmitt trigger and waveform generator involving CCCII as an active device.

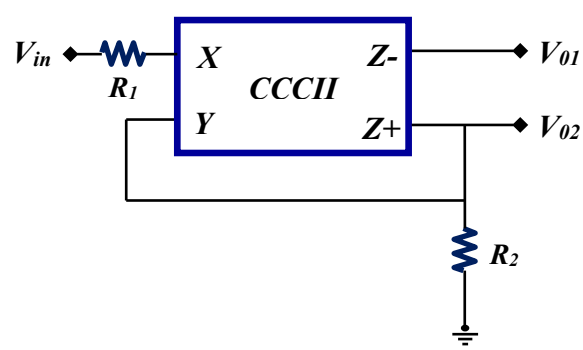

Fig. 3. Proposed dual output Schmitt trigger using CCCII

The configuration shown in Fig. 3 basically act as a comparator with positive feedback. The loop gain βV_{02}, (where $\beta = R_2/[R_2+R_B]$ is the feedback gain) is fed as input to the port Y. The input voltage, sinusoidal signal is applied to input port X. The input voltage V_{in} triggers the output V_{02} whenever it exceeds certain voltage levels called upper threshold voltage (V_{UT}) and lower threshold voltage (V_{LT}). As long as V_{in} is less than V_{UT} the output remains at $+V_{sat}$ at output V_{02}. When V_{in} just exceeds V_{UT}, the output regeneratively switches to $-V_{sat}$ and remain at this level as long as V_{in} is greater than V_{UT}. For $V_{02} = -V_{sat}$, the feedback gain will be $-\beta V_{02}$, when the input voltage V_{in} becomes lesser than V_{LT}, causes V_{02} to switch from $-V_{sat}$ *to* $+V_{sat}$. The difference between these two voltages is the hysteresis width V_H.

Using nodal analysis and current-voltage characteristics of CCCII as specified in (1), the expression for the output

voltage can be solved as given below:

The input current at terminal X is:

$$I_{in} = \frac{V_{in} - V_X}{R_1} \tag{4}$$

The input current at terminal Y is:

$$I_Y = \frac{V_{02} - V_Y}{R_2} \tag{5}$$

Solving the above equations using (1), the expression for V_{UT} and V_{LT} are derived as below:

The upper threshold voltage is expressed as:

$$V_{UT} = \frac{R_2}{R_1 + R_2 + R_B}\left(+V_{sat}\right) \tag{6}$$

The lower threshold voltage is expressed as:

$$V_{LT} = \frac{R_2}{R_1 + R_2 + R_B}\left(-V_{sat}\right) \tag{7}$$

Using additional current mirror configuration, square wave output with 180º is obtained at output terminal V_{01}. The hysteresis voltage shifts in between $+V_{sat}$ and $-V_{sat}$ and graphically shown in Fig. 4. Hysteresis is indicative of noise effect and delay appearing in the output signal. As value is lowered, the better would be the performance of the device [6]-[9].

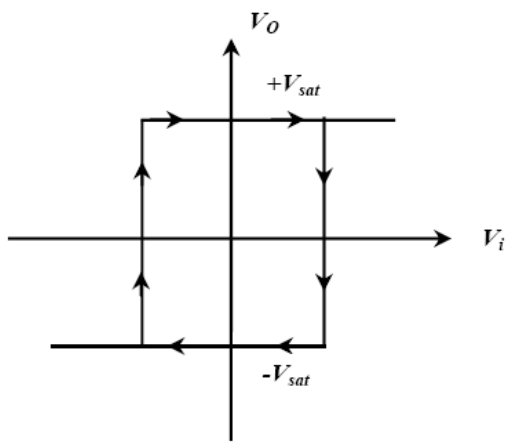

Fig. 4. Hysteresis phenomenon for the proposed circuit Fig. 3

Non-Ideal Analysis

Taking into consideration of non-idealities of the CCCII, the basic equation (1) can be expressed as:

$$\begin{bmatrix} I_Y \\ V_X \\ I_Z \end{bmatrix} = \begin{bmatrix} 0 & 0 & 0 \\ \alpha & R_B & 0 \\ 0 & \beta & 0 \end{bmatrix} \begin{bmatrix} V_Y \\ I_X \\ V_Z \end{bmatrix} \tag{8}$$

where α = 1-ε, |ε| << 1 represents the tracking error of voltage and β =1-δ, |δ| << 1 is the tracking error of current.

Using the small signal analysis, the voltage transfer gain α and current transfer gain β are expressed as:

$$\alpha = \frac{V_X}{V_Y} = \frac{(g_{m2} + g_{m4})r_{02} \parallel r_{04}}{1 + (g_{m2} + g_{m4})r_{02} \parallel r_{04}} \tag{9}$$

$$\beta = \frac{I_Z}{I_X} = \frac{g_{m9}g_{m2}g_{m13} + g_{m4}g_{m12}g_{m11}}{g_{m9}g_{m12}(g_{m4} + g_{m12})} \tag{10}$$

The ideal value of α is unity and for balanced operation in the above equation, g_{m13}=g_{m12} and g_{m11}=g_{m19}, if these conditions are applied then β is also unity.

Including the non-idealities the representation for the output voltage is expressed as:

$$V_{02} = \frac{\beta R_2 V_{in}}{R_1 + R_B + \alpha\beta R_2} \tag{11}$$

Further, the threshold voltage expressions are represented by

The upper threshold voltage is expressed by:

$$V_{UT} = \frac{\beta R_2}{R_1 + \alpha\beta R_2 + R_B}\left(+V_{sat}\right) \tag{12}$$

The lower threshold voltage by:

$$V_{LT} = \frac{\beta R_2}{R_1 + \alpha\beta R_2 + R_B}\left(-V_{sat}\right) \tag{13}$$

From the above equations it is clear that the presence of non-idealities does not effect the performance of the design and the effect of non-ideal gains can be ignored. It can be easily verified that equations (12) and (13) reduce to equations (6) and (7) as expected, for ideal CCCII± when $\alpha = 1$ and $\beta = 1$.

IV. Simulation Results

The proposed Schmitt trigger in Fig. 3 has been simulated using PSPICE simulator. The internal schematic of CCCII was realized as specified in Fig. 2 by using 0.35 µm CMOS technology. The voltages $\pm V_{CC}$ = 2 V and the value of dc biased current is I_B = 50 µA (R_B = 260Ω) along with R_1 = 1 kΩ and R_2 =10 kΩ are applied. The input signal frequency is 2 kHz and signal voltage 5 $V_{p\text{-}p}$. The distinctive output waveforms at the output terminals V_{01} and V_{02} are illustrated in Fig. 5 and Fig. 6. The theoretical and simulated output voltages are matched depending on the upper and lower threshold voltages as derived previously. The frequency spectrum for the output voltage is shown in Fig. 7, it determines the range of frequency and above that the device works effectively.

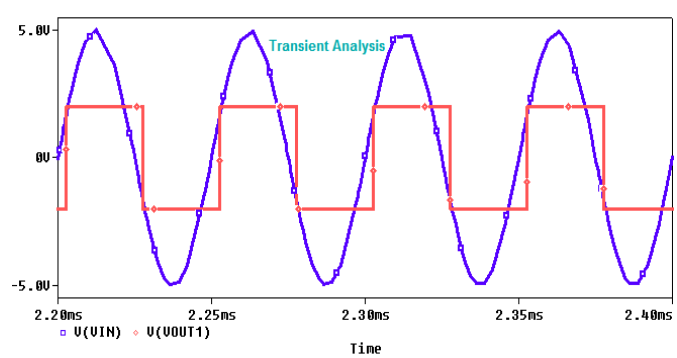

Fig. 5. The output waveform for the proposed Schmitt trigger at terminal V_{01}

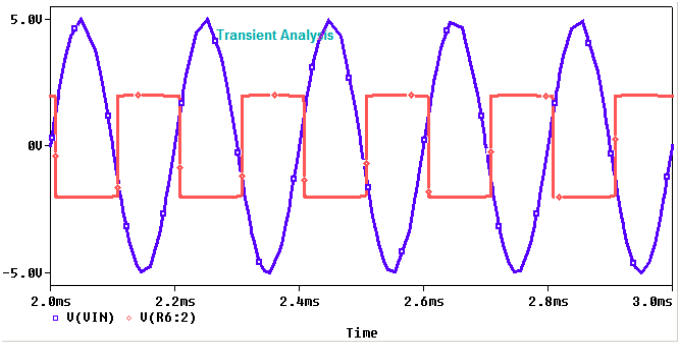

Fig. 6. The output waveform for the proposed Schmitt trigger at terminal V_{02}

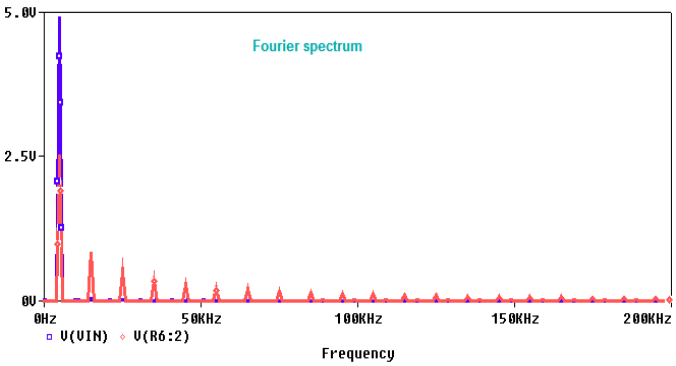

Fig. 7. Frequency spectrum of proposed Schmitt trigger

Montecarlo simulation is a technique used to measure uncertainty in the output signal. It is a technique that produces distributions of possible outcome values. The variable considered is resistance with a tolerance of 5% and run over for 50 iterations. Fig. 8 is the graph representing Montecarlo results for the proposed configuration. The mean value and standard deviation are 2.0017 and 0.000042 respectively which are quite low and suitable for better performance of the circuit. Fig. 9 represents the worst-case analysis for the proposed configuration. This analysis is used to identify the most critical components which will affect the circuit performance. It is accomplished by setting all the resistance values to their peak tolerance limits which gives the indication of the worst case results. For the proposed configuration the graph in Fig. 9 represents the least variation of output voltage with respect to the 5% variation in the tolerance of the resistance of Schmitt trigger circuit.

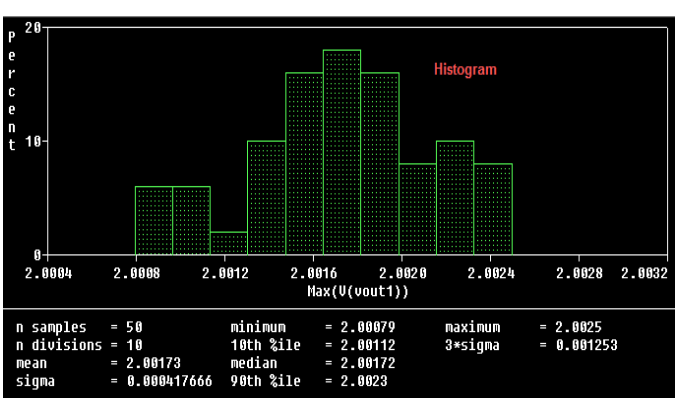

Fig. 8. Histogram for the output signal-1 of the proposed Schmitt trigger

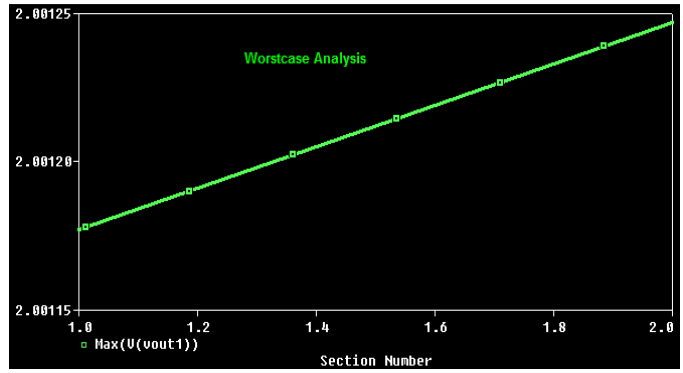

Fig. 9. Worst-case Analysis for the output signal V01 of the proposed Schmitt trigger

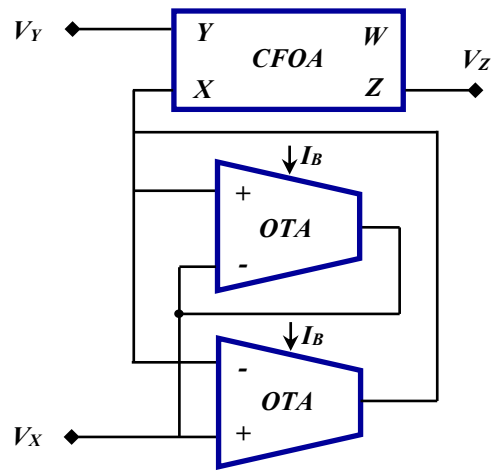

Fig. 10. Prototype of CCCII using CFOA and OTA

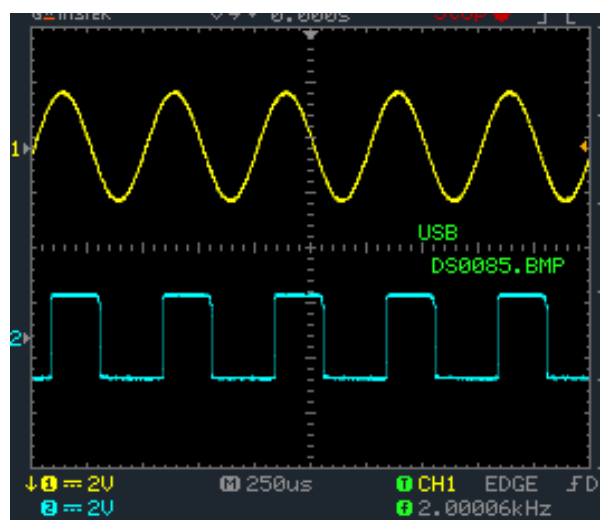

Fig.11. Experimental results of the proposed Schmitt trigger at V_{01} of Fig. 3 on oscilloscope (Scale X-axis 250 µs/div and Y-axis 2 V/div)

V. Experimental Results

CCCII prototype is implemented using the structure shown in Fig. 10 [21]. The hardware implementation of the proposed design is done on laboratory bread board with commercially available current feedback operational amplifiers (CFOA), IC

AD844AN [33] and operational transconductance amplifiers (OTA), IC LM31700 [34]. The resultant output waveforms are included in Fig. 11 and Fig. 12. The output result shown in Fig. 11 is represented by V_{01}, where as for the output indicated in Fig. 12 is by V_{02} for the specifications of R_1=1kΩ, R_2 =10 kΩ, I_B=100 μA and input signal frequency of 2 kHz with $2V_{p-p}$. The experimental results determine that the proposed Schmitt trigger is best suited to perform the hysteresis operation and is represented graphically in Fig. 13.

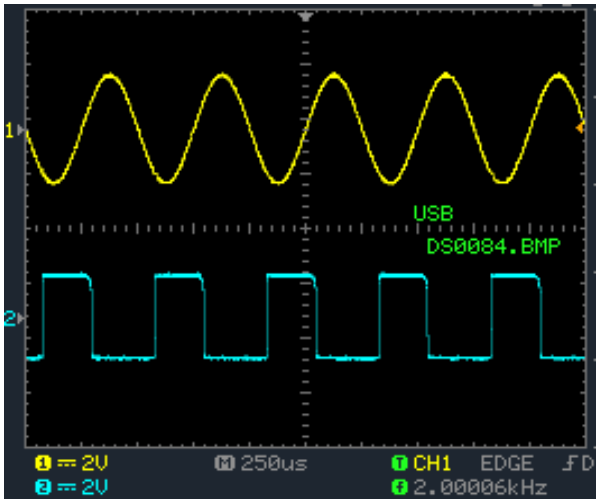

Fig.12. Experimental results of the proposed Schmitt trigger at V_{02} of Fig. 3. on oscilloscope (Scale X-axis 250 μs/div and Y-axis 2 V/div)

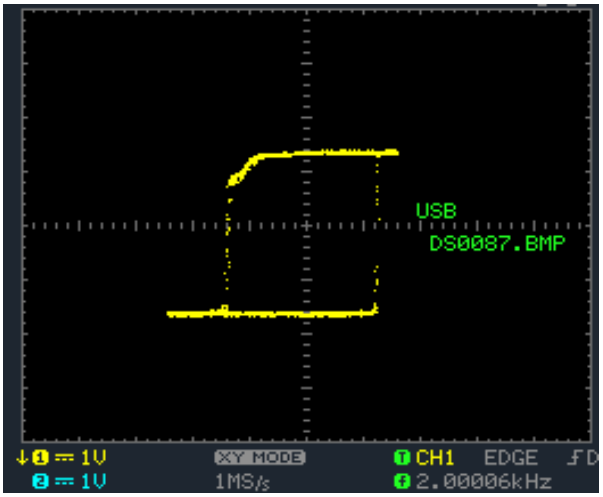

Fig. 13. Hysteresis phenomenon for the proposed Schmitt trigger.

The design involving dual output Schmitt trigger is mainly focussed on utilizing lesser number of active elements and passive components. Many topologies are available in the literature on Schmitt triggers and some of the topologies of our interest are listed in the comparison Table I. The configurations of [4] and [5] utilizes more number of active elements whereas, the circuits of [4], [5], [13] and [20] have more number of passive components involved in realization. The common drawback is that number of active and passive elements occupies more area and thereby large power consumption. Usually, these types of topologies are less preferred for IC fabrication. The structure of [22] has the advantage of having a single active device with no resistors. It suffers from certain drawback by having 28 MOS Transistors for its realization and able to produce single output. Whereas, the proposed configuration finds the advantage of utilizing single CCCII along with only two resistors for realization and is able to produce dual outputs. It can be applied as waveform generator, pulse width modulator, multivibrators e.t.c. It can also be utilized in realizing many electronic circuits. It is also well suited for IC fabrication.

VI. Conclusion

In this manuscript, a current mode dual output Schmitt trigger topology using CCCII is presented. The circuit has only two resistors and a CCCII as an active element, which is more advantageous for IC fabrication. Simulation results verifying theoretical analysis are included along with frequency spectrum. Montecarlo analysis and worst-case analysis are determined. Hardware results of the proposed design are obtained which are in similarity with the software results. The comparative analysis of the proposed topology is made with the existing methods. The reported topology has simple structure that requires less active and passive components, thereby, less area and offers low power dissipation than the other similar technologies.

References

[1] A. Sedra and K. C. Smith, "A second-generation current conveyor and its applications," *IEEE Trans. Circuit Theory*, vol.CT-17, no.1, pp. 132-134, Feb. 1970.

[2] A. S. Sedra, G. W. Roberts, and F. Gohh, "The current conveyor: History, progress and new results," *Proc. Inst. Elect. Eng. Part G*, vol. 137, no. 2, pp. 78–87, Apr. 1990.

Table I. State of Art Comparison of Proposed Dual Output Schmitt Trigger

Reference	Active Element	Number of Active Elements	Number of Passive Elements	Number of Resistors	Single/ Dual output
[4] Jiri Misurec *et.al*	CCII	2	4	4	Single
[5] A. Srinivasulu	CCII	2	4	4	Single
[13] S. Minaei *et.al*	DVCC	1	2	2	Single
[14] Y. K. Lo *et.al*	OTRA	1	1	1	Single
[20] M. Faseehuddin *et.al*	DOCCCII, Inverter	1, 1	2	2	Single
[22] A. Kumar *et. al*	DXCCTA	1	0	0	Single
Proposed Circuit of Fig. 3	CCCII	1	2	2	Dual

[3] D. Pal, A. Srinivasulu, B. B. Pal, A. Demosthenous, and B. N. Das, "Current conveyor- based square/triangular waveform generators with improved linearity," *IEEE Tran. Instr. and Measurements*, vol. 58, no.7, pp.2174-2180, 2009. DOI: 10.1109/TIM. 2008.2006729.

[4] Jiri Misurec and Jaroslav Koton, "Schmitt Trigger with controllable hysteresis using current conveyors," *International Journal of Advanced Technology in Engineering and Sciences*, vol.50, no.7, pp.184-192, 2012. DOI: 10.11601/ijates.v1i1.9.

[5] A. Srinivasulu, "A novel current conveyor based Schmitt trigger and its application as a relaxation oscillator", *International Journal of Circuit Theory and Applications*, vol. 39, no. 6, pp. 679-686, Jun 2011. DOI:10.1002/cta.669.

[6] Syed Zahiruddin and A. Srinivasulu "A Simple Schmitt Trigger Using Second Generation Current Controlled Conveyor", *Journal of Advanced Research in Dynamical and Control Systems*, vol. 11, Issue. 07-SI, pp. 41-48, 2019.

[7] K.C. Smith and A. Sedra, ―The current conveyor –A new circuit buiiding block, *Proc. IEEE*, vol. 56, no. 8, pp.1368-1369, Aug. 1968.

[8] A. Bhargav, A. Srinivasulu and D. Pal, "An Operational Transconductance Amplifiers Based Sinusoidal Oscillator Using CNTFETs, in proc.of the 23rd IEEE International Conference on Applied Electronics (IEEE ICAE-2018), Pilsen, Czech Republic, 11 Sept - 13 Sept, 2018, Pages-6. DOI: 10.23919/AE.2018.8501428.

[9] Martin Drinovsky, Jiri Hospodka, "Triangular/Square waveform generator using area efficient hysteresis comparator," *Radioengineering,* Vol. 25, No.2, pp.332-337, 2016. DOI: 10.13164/re.2016.0332.

[10] V. Vijay and A. Srinivasulu, "A novel square wave generator using Second Generation Differential Current Conveyor," *Arabian Journal for Science and Engineering*, vol. 42, no. 12, pp. 4983-4990, 2017, DOI: 10.1007/s13369-017-2539-6. ISSN: 2193-567X.

[11] A. Srinivasulu and D. Pal, "CCII+ Based Dual Square-Cum-Triangular Waveform Generator", *in proc. of* IEEE International Conference on Electronics, Computers and Artificial Intelligence (IEEE ECAI 2017), Targoviste, Romania, 29 June - 01 July, 2017, pp. 6. DOI:10.1109/ECAI.2017.8166422.

[12] Yu-Kang Lo, Hung-Chun Chien and Huang-Jen Chiu, "Current input OTRA Schmitt trigger with dual hysteresis modes," *International Journal of Circuit Theory and Applications*, pp. 739-746, 2010. DOI: 10.1002/cta.584.

[13] S. Minaei, E. Yuce, "A simple Schmitt trigger circuit with grounded passive elements and its application to square/triangular wave generator," *Circuits Systems Signal Process.*, vol. 31, pp. 877-888, 2012. DOI: 10.1007/300034-011-9373-4.

[14] Y.K. Lo, H.C. Chien, H.J. Chiu, "Current input OTRA Schmitt trigger with dual hysteresis modes," *International Journal of Circuit Theory and Applications*, vol. 38, pp. 739-746, 2009. DOI: 10.1002/cta.584.

[15] H.C Chien, "Voltage-controlled dual slope operation square/triangular wave generator and its application as a dual mode operation pulse width modulator employing differential voltage current conveyors," *Journal of Microelectronics*, vol.43, Issue 12, pp. 962–974, 2012. DOI:10.1016/j.mejo.2012.08.005.

[16] R. Sotner, J. Jerabek, N. Herencsar, A. Lahiri, J. Petrzela, K. Vrba, "Practical aspects of operation of simple triangular and square wave generator employing diamond transistor voltage controllable amplifiers," *in proc. of* 36th International Conference on Telecommunications and Signal Processing (TSP 2013), Rome, Italy, 2–4 July 2013, pp. 431–435.

[17] M. L. Lavanya, A. Srinivasulu and V. V. Reddy, "ZC-CDTA based integrator circuit using single passive component", Lecture Notes in Electrical Engineering, vol. 476, pp. 179-187, 2018. DOI: 10.1007/978-981-10-8234-4_16.

[18] Avireni Srinivasulu, "Current conveyor based relaxation oscillator with tunable grounded resistor/capacitor", *International Journal of Design, Analysis and Tools for Circuits and Systems* (Hong-Kong), vol. 3, no. 2, pp. 1-7, Nov 2012.

[19] M. Siripruchyanun, K. Payakkakul, P. Pipatthitikorn and P. Satthaphol, " A current-mode Square/Triangular wave generator based on multiple output VDTAs," *Science Direct Procedia Computer Science* 86, pp. 152-155, Thailand, 2016. DOI: 10.1016/j.procs.2016.05.040.

[20] M. Faseehuddin, J. Sampe, S. Islam, "Schmitt trigger based on dual output current controlled current conveyor in 16 nm CMOS technology for digital applications," *in. Proc. of* International Conference on Semiconductor Electronics (IEEE-ICSE 2016), pp. 82-85, Malaysia, 2016. DOI: 10.1109/SMELEC.2016.7573596.

[21] C. Chanapromma, N. Maneetien and M. Siripruchyanum, "A practical implementation of the CC-CFA based on commercially available ICs and its applications," *in. Proc. of* Int. Conf. On Electrical Engineering /Electronics, Computer, Telecommunications and Information Technology (ECTI-CON 2009), Pattaya, Chonburi, 6-9 May, 2009, pp. 564-567.

[22] A. Kumar and B. Chaturvedi, "Novel electronically controlled current-mode Schmitt trigger based on single active element," International Journal of Electronics and Communications, vol. 82, pp. 160–166, 2017. DOI:10.1016/j.aeue.2017.08.007.

[23] R. Sotner, J. Jerabek, N. Herencsar, A. Lahiri, J. Petrzela and K. Vrba, "Practical Aspects of Operation of Simple Triangular and Square Wave Generator Employing Diamond Transistor and Controllable Amplifiers", *in. Proc. of* 36th International Conference on Telecommunications and Signal Processing, Rome, Italy, Jul. 2-4, pp. 431-435, 2013.

[24] D. Marcellis, C. Di Carlo, G. Ferri and V. Stornelli, "A CCII-based wide frequency range square waveform generator," *International Journal of Circuit Theory and Applications*, vol. 41, iss. 1, pp. 1-13, 2013.

[25] H. C. Chien, "Voltage-controlled dual slope operation square/triangular wave generator and its application as a dual mode operation pulse width modulator employing differential voltage current conveyors," *Microelectronics Journal,* vol. 43, iss. 12, pp. 962-974, 2012.

[26] H. Kim, H. J. Kim and W. S. Chung, "Pulsewidth modulation circuits using CMOS OTAs," *IEEE Trans. Circuits and Syst. I*, vol. 54, no. 9, pp. 1869-1878, 2007.

[27] W.S. Chung, H. Kim, H.W. Cha, and H.J. Kim, "Triangular/square wave generator with independently controllable frequency and amplitude*," IEEE Trans. Instrum. Meas.,* vol. 54, no. 1, pp. 105–109, 2005.

[28] Y. K. Lo and H. C. Chien, "Switch-Controllable OTRA-Based Square/Triangular Waveform Generator," *IEEE Transactions on Circuits and Systems-II*: Express briefs, vol. 54, no. 12, pp. 1110-1114, 2007.

[29] M. Siripruchyanun, P. Satthaphol and K. Payakkakul, "A Simple Fully Controllable Schmitt Trigger with Electronic method using VDTA", *Applied Mechanics and Materials*, vol. 781, pp. 180-183, DOI: 10.4028/www.scientific.net/AMM.781.180, 2015.

[30] V. Vijay and A. Srinivasulu, "A low power waveform generator using DCCII with grounded capacitor", *International Journal of Public Sector Performance Management*, vol. 5, issue. 2, pp. 134-145, 2019, DOI: 10.1504/IJPSPM.2019.099084.

[31] M. T. Abuelmatti and M. A. Al-Absi, "A current conveyor-based relaxation oscillator as a versatile electronic interface for capacitive and resistive sensors," *Int. J. Electron*., vol. 92, no. 8, pp. 473-477, DOI: 10.1080/08827510451001694798, 2005.

[32] M. Drinovsky, J. Hospokda, "Triangular/Square waveform generator using area efficient hysteresis comparator," *Radioengineering*, vol. 25, no.2, pp.332-337, DOI: 10.13164/re.2016.0332, 2016.

[33] AD844, *Current Feedback Op-Amp Data Sheet*, Analog Devices Inc., Norwood, MA, 1990.

[34] LM13600, Dual Operational Transconductance Amplifiers Data Sheet, National Semiconductor, 1995.

Preparation of Papers for Electronics (September 2011)

First A. Author, Second B. Author, and Third C. Author

***Abstract*—These instructions give you guidelines for preparing papers for ELECTRONICS journal. Use this document as a template if you are using Microsoft *Word* 6.0 or later. Otherwise, use this document as an instruction set. The electronic file of your paper will be formatted further. Define all symbols used in the abstract. Do not cite references in the abstract. Do not delete the blank line immediately above the abstract; it sets the footnote at the bottom of this column.**

***Index Terms*—About four key words or phrases in alphabetical order, separated by commas.**

Paper Classification
DOI: 10.7251/ELSxxxxxxxx

I. Introduction

THIS document is a template for Microsoft *Word* versions 6.0 or later.

When you open the file, select "Page Layout" from the "View" menu in the menu bar (View | Page Layout), which allows you to see the footnotes. Then, type over sections of file or cut and paste from another document and use markup styles. The pull-down style menu is at the left of the Formatting Toolbar at the top of your *Word* window (for example, the style at this point in the document is "Text"). Highlight a section that you want to designate with a certain style, then select the appropriate name on the style menu. The style will adjust your fonts and line spacing. **Do not change the font sizes or line spacing to squeeze more text into a limited number of pages.** Use italics for emphasis; do not underline. The length of the manuscript is limited to the maximum of 15 pages.

To insert images in *Word,* position the cursor at the insertion point and either use Insert | Picture | From File or copy the image to the Windows clipboard and then Edit | Paste Special | Picture (with "float over text" unchecked).

We will do the final formatting of your paper.

Manuscript received 15 September 2011 (write the date when you have first sent the manuscript for review). Received in revised form 20 October 2011 (write the date when you have sent the manuscript in its revised form if revisions required for your paper after review).

(Place here any sponsor and financial support acknowledgments).

F. A. Author is with the Faculty of Electrical Engineering, University of Banja Luka, Banja Luka, Bosnia and Herzegovina (corresponding author to provide phone: +387-51-222-333; fax: +387-51-111-222; e-mail: author@et-fbl.net).

S. B. Author was with Faculty of Technical Sciences, University of Novi Sad, Novi Sad, Serbia. He is now with the Institute "Mihailo Pupin", Belgrade, Serbia (e-mail: author@pupin.rs).

T. C. Author is with the School of Electrical Engineering, University of Belgrade, Belgrade, Serbia, on leave from the Faculty of Electronic Engineering, University of Niš, Niš, Serbia (e-mail: author@elfak.ni.ac.rs).

II. Procedure for Paper Submission

A. Review Stage

The manuscripts are to be submitted using the Electronics Journal online submission system – accessible from Journal's homepage. Prepare it in two-column format as shown in this template. Place all figures and tables at the end of the paper (after the references) on separate page(s). Figures and tables must have the same caption names as referenced in the text. Only PDF format of the manuscript is allowed at the review stage. Please, check if all fonts are embedded and subset and that the quality of diagrams, illustrations, and graphics is satisfactory. Failing to provide above listed requirements is a valid reason for rejection.

B. Final Stage

When you submit your final version (after your paper has been accepted), prepare it in two-column format, including figures and tables in accordance with this template. Pack all of your files (manuscript source file in *Word*, figures, and manuscript PDF form) within one archive file (you may use any of the available file compression tools: *WinZip*, *WinRAR*, *7-Zip*, etc.). Do not forget to provide the manuscript converted in PDF format that will be used as a reference for final formatting of your paper. Figures should be named as referenced in the manuscript (e.g. *fig1.eps*, *fig2.tif*, etc.)

C. Figures and Tables

Format and save your graphic images using a suitable graphics processing program and adjusts the resolution settings. We accept images in the following formats: PS, EPS, TIFF, GIF, and PNG. Additionally, it is allowed to use images generated by using one of the following software tools: Microsoft Word, Microsoft PowerPoint, or Microsoft Excel. The resolution of a RGB color file should be 400 dpi. Please note that JPG and other lossy-compressed image formats are not allowed. Use available software tools to convert these images to appropriate format.

Image quality is very important to how yours graphics will reproduce. Even though we can accept graphics in many formats, we cannot improve your graphics if they are poor quality when we receive them. If your graphic looks low in

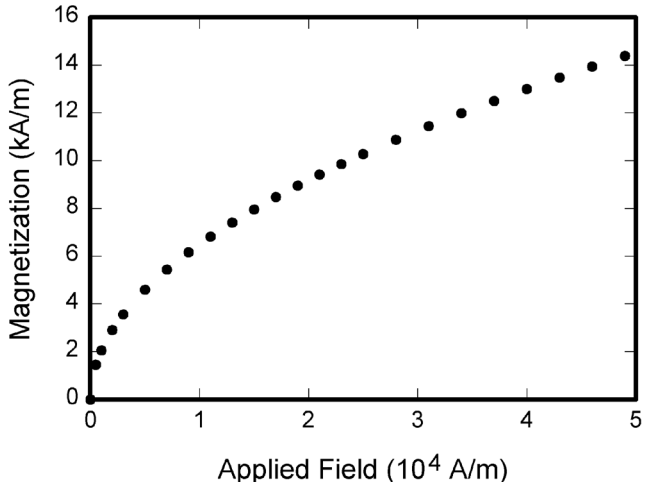

Fig. 1. Magnetization as a function of applied field. Note that "Fig." is abbreviated. There is a period after the figure number, followed by two spaces. It is good practice to explain the significance of the figure in the caption.

quality on your printer or monitor, please keep in mind that cannot improve the quality after submission.

If you are importing your graphics into this Word template, please use the following steps:

Under the option EDIT select PASTE SPECIAL. A dialog box will open, select paste picture, then click OK. Your figure should now be in the Word Document.

If you are preparing images in TIFF, EPS, or PS format, note the following. High-contrast line figures and tables should be prepared with 600 dpi resolution and saved with no compression, 1 bit per pixel (monochrome).

Photographs and grayscale figures should be prepared with 300 dpi resolution and saved with no compression, 8 bits per pixel (grayscale).

Most charts graphs and tables are one column wide (3 1/2 inches or 21 picas) or two-column width (7 1/16 inches, 43 picas wide). We recommend that you avoid sizing figures less than one column wide, as extreme enlargements may distort your images and result in poor reproduction. Therefore, it is better if the image is slightly larger, as a minor reduction in size should not have an adverse affect the quality of the image.

III. Math

If you are using *Word,* use either the Microsoft Equation Editor or the *MathType* add-on (http://www.mathtype.com) for equations in your paper (Insert | Object | Create New | Microsoft Equation *or* MathType Equation). "Float over text" should *not* be selected.

IV. Units

Use either SI (MKS) or CGS as primary units. (SI units are strongly encouraged.) English units may be used as secondary units (in parentheses). **This applies to papers in data storage.** For example, write "15 Gb/cm^2 (100 Gb/in^2)." An exception is when English units are used as identifiers in trade, such as "3½-in disk drive." Avoid combining SI and CGS units, such as current in amperes and magnetic field in oersteds. This often leads to confusion because equations do not balance dimensionally. If you must use mixed units, clearly state the units for each quantity in an equation.

The SI unit for magnetic field strength H is A/m. However, if you wish to use units of T, either refer to magnetic flux density B or magnetic field strength symbolized as $\mu_0 H$. Use the center dot to separate compound units, e.g., "A·m^2."

TABLE I
Units for Magnetic Properties

Symbol	Quantity	Conversion from Gaussian and CGS EMU to SI [a]
Φ	magnetic flux	1 Mx $\rightarrow 10^{-8}$ Wb = 10^{-8} V·s
B	magnetic flux density, magnetic induction	1 G $\rightarrow 10^{-4}$ T = 10^{-4} Wb/m^2
H	magnetic field strength	1 Oe $\rightarrow 10^3/(4\pi)$ A/m
m	magnetic moment	1 erg/G = 1 emu $\rightarrow 10^{-3}$ A·m^2 = 10^{-3} J/T
M	magnetization	1 erg/(G·cm^3) = 1 emu/cm^3 $\rightarrow 10^3$ A/m
$4\pi M$	magnetization	1 G $\rightarrow 10^3/(4\pi)$ A/m
σ	specific magnetization	1 erg/(G·g) = 1 emu/g $\rightarrow$ 1 A·m^2/kg
j	magnetic dipole moment	1 erg/G = 1 emu $\rightarrow 4\pi \times 10^{-10}$ Wb·m
J	magnetic polarization	1 erg/(G·cm^3) = 1 emu/cm^3 $\rightarrow 4\pi \times 10^{-4}$ T
χ, κ	susceptibility	1 $\rightarrow 4\pi$
χ_ρ	mass susceptibility	1 cm^3/g $\rightarrow 4\pi \times 10^{-3}$ m^3/kg
μ	permeability	1 $\rightarrow 4\pi \times 10^{-7}$ H/m = $4\pi \times 10^{-7}$ Wb/(A·m)
μ_r	relative permeability	$\mu \rightarrow \mu_r$
w, W	energy density	1 erg/cm^3 $\rightarrow 10^{-1}$ J/m^3
N, D	demagnetizing factor	1 $\rightarrow 1/(4\pi)$

Vertical lines are optional in tables. Statements that serve as captions for the entire table do not need footnote letters.

[a]Gaussian units are the same as cgs emu for magnetostatics; Mx = maxwell, G = gauss, Oe = oersted; Wb = weber, V = volt, s = second, T = tesla, m = meter, A = ampere, J = joule, kg = kilogram, H = henry.

V. Helpful Hints

A. Figures and Tables

Because we will do the final formatting of your paper, you do not need to position figures and tables at the top and bottom of each column. In fact, all figures, figure captions, and tables can be at the end of the paper. Large figures and tables may span both columns. Place figure captions below the figures; place table titles above the tables. If your figure has two parts, include the labels "(a)" and "(b)" as part of the artwork. Please verify that the figures and tables you mention in the text actually exist. **Please do not include captions as part of the figures. Do not put captions in "text boxes" linked to the figures. Do not put borders around the outside of your figures.** Use the abbreviation "Fig." even at the beginning of a sentence. Do not abbreviate "Table." Tables are numbered with Roman numerals.

Color printing of figures is not available Do not use color unless it is necessary for the proper interpretation of your figures.

Figure axis labels are often a source of confusion. Use words rather than symbols. As an example, write the quantity "Magnetization," or "Magnetization *M*," not just "*M*." Put units in parentheses. Do not label axes only with units. As in Fig. 1, for example, write "Magnetization (A/m)" or "Magnetization ($A \cdot m^{-1}$)," not just "A/m." Do not label axes with a ratio of quantities and units. For example, write "Temperature (K)," not "Temperature/K."

Multipliers can be especially confusing. Write "Magnetization (kA/m)" or "Magnetization (10^3 A/m)." Do not write "Magnetization (A/m) x 1000" because the reader would not know whether the top axis label in Fig. 1 meant 16000 A/m or 0.016 A/m. Figure labels should be legible, approximately 8 to 12 point type.

B. References

Number citations consecutively in square brackets [1]. The sentence punctuation follows the brackets [2]. Multiple references [2], [3] are each numbered with separate brackets [1]–[3]. When citing a section in a book, please give the relevant page numbers [2]. In sentences, refer simply to the reference number, as in [3]. Do not use "Ref. [3]" or "reference [3]" except at the beginning of a sentence: "Reference [3] shows ... ." Please do not use automatic endnotes in *Word*, rather, type the reference list at the end of the paper using the "References" style.

Number footnotes separately in superscripts (Insert | Footnote).[1] Place the actual footnote at the bottom of the column in which it is cited; do not put footnotes in the reference list (endnotes). Use letters for table footnotes (see Table I).

Please note that the references at the end of this document are in the preferred referencing style. Give all authors' names; do not use "*et al*." unless there are six authors or more. Use a space after authors' initials. Papers that have not been published should be cited as "unpublished" [4]. Papers that have been accepted for publication, but not yet specified for an issue should be cited as "to be published" [5]. Papers that have been submitted for publication should be cited as "submitted for publication" [6]. Please give affiliations and addresses for private communications [7].

Capitalize only the first word in a paper title, except for proper nouns and element symbols. For papers published in translation journals, please give the English citation first, followed by the original foreign-language citation [8]. All references **must be** written in Roman alphabet.

C. Abbreviations and Acronyms

Define abbreviations and acronyms the first time they are used in the text, even after they have already been defined in the abstract. Abbreviations such as IEEE, SI, ac, and dc do not have to be defined. Abbreviations that incorporate periods should not have spaces: write "C.N.R.S.," not "C. N. R. S." Do not use abbreviations in the title unless they are unavoidable (for example, "IEEE" in the title of this article).

D. Equations

Number equations consecutively with equation numbers in parentheses flush with the right margin, as in (1). First use the equation editor to create the equation. Then select the "Equation" markup style. Press the tab key and write the equation number in parentheses. To make your equations more compact, you may use the solidus (/), the exp function, or appropriate exponents. Use parentheses to avoid ambiguities in denominators. Punctuate equations when they are part of a sentence, as in

$$\int_0^{r_2} F(r,\varphi)\, d\varphi = [\sigma r_2 / (2\mu_0)] \cdot \int_0^{\infty} \exp(-\lambda\,|z_j - z_i|)\, \lambda^{-1} J_1(\lambda r_2)\, J_0(\lambda r_i)\, d\lambda \,. \tag{1}$$

Be sure that the symbols in your equation have been defined before the equation appears or immediately following. Italicize symbols (*T* might refer to temperature, but T is the unit tesla). Refer to "(1)," not "Eq. (1)" or "equation (1)," except at the beginning of a sentence: "Equation (1) is ... ."

E. Other Recommendations

Use one space after periods and colons. Hyphenate complex modifiers: "zero-field-cooled magnetization." Avoid dangling participles, such as, "Using (1), the potential was calculated." [It is not clear who or what used (1).] Write instead, "The potential was calculated by using (1)," or "Using (1), we calculated the potential."

Use a zero before decimal points: "0.25," not ".25." Use "cm^3," not "cc." Indicate sample dimensions as "0.1 cm x 0.2 cm," not "0.1 x 0.2 cm^2." The abbreviation for "seconds" is "s," not "sec." Do not mix complete spellings and abbreviations of units: use "Wb/m^2" or "webers per square meter," not "webers/m^2." When expressing a range of values, write "7 to 9" or "7-9," not "7~9."

A parenthetical statement at the end of a sentence is punctuated outside of the closing parenthesis (like this). (A parenthetical sentence is punctuated within the parentheses.) In American English, periods and commas are within quotation marks, like "this period." Other punctuation is "outside"! Avoid contractions; for example, write "do not" instead of "don't." The serial comma is preferred: "A, B, and C" instead of "A, B and C."

If you wish, you may write in the first person singular or plural and use the active voice ("I observed that ..." or "We observed that ..." instead of "It was observed that ..."). Remember to check spelling. If your native language is not English, please get a native English-speaking colleague to carefully proofread your paper.

[1] It is recommended that footnotes be avoided (except for the unnumbered footnote with the receipt date and authors' affiliations on the first page). Instead, try to integrate the footnote information into the text.

VI. Some Common Mistakes

The word "data" is plural, not singular. The subscript for the permeability of vacuum μ_0 is zero, not a lowercase letter "o." The term for residual magnetization is "remanence"; the adjective is "remanent"; do not write "remnance" or "remnant." Use the word "micrometer" instead of "micron." A graph within a graph is an "inset," not an "insert." The word "alternatively" is preferred to the word "alternately" (unless you really mean something that alternates). Use the word "whereas" instead of "while" (unless you are referring to simultaneous events). Do not use the word "essentially" to mean "approximately" or "effectively." Do not use the word "issue" as a euphemism for "problem." When compositions are not specified, separate chemical symbols by en-dashes; for example, "NiMn" indicates the intermetallic compound $Ni_{0.5}Mn_{0.5}$ whereas "Ni–Mn" indicates an alloy of some composition Ni_xMn_{1-x}.

Be aware of the different meanings of the homophones "affect" (usually a verb) and "effect" (usually a noun), "complement" and "compliment," "discreet" and "discrete," "principal" (e.g., "principal investigator") and "principle" (e.g., "principle of measurement"). Do not confuse "imply" and "infer."

Prefixes such as "non," "sub," "micro," "multi," and "ultra" are not independent words; they should be joined to the words they modify, usually without a hyphen. There is no period after the "et" in the Latin abbreviation "*et al.*" (it is also italicized). The abbreviation "i.e.," means "that is," and the abbreviation "e.g.," means "for example" (these abbreviations are not italicized).

An excellent style manual and source of information for science writers is [9].

VII. Editorial Policy

Each manuscript submitted is subjected to the following review procedure:

- It is reviewed by the editor for general suitability for this publication
- If it is judged suitable, two reviewers are selected and a single-blinded review process takes place
- Based on the recommendations of the reviewers, the editor then decides whether the particular paper should be accepted as is, revised or rejected.

Do not submit a paper you have submitted or published elsewhere. Do not publish "preliminary" data or results. The submitting author is responsible for obtaining agreement of all coauthors and any consent required from sponsors before submitting a paper. It is the obligation of the authors to cite relevant prior work.

Every paper submitted to "Electronics" journal are single-blind reviewed. For conference-related papers, the decision to accept or reject a paper is made by the conference editors and publications committee; the recommendations of the referees are advisory only. Undecipherable English is a valid reason for rejection.

VIII. Publication Principles

The contents of "Electronics" are peer-reviewed and archival. The "Electronics" publishes scholarly articles of archival value as well as tutorial expositions and critical reviews of classical subjects and topics of current interest.

Authors should consider the following points:

1) Technical papers submitted for publication must advance the state of knowledge and must cite relevant prior work.
2) The length of a submitted paper should be commensurate with the importance, or appropriate to the complexity, of the work. For example, an obvious extension of previously published work might not be appropriate for publication or might be adequately treated in just a few pages.
3) Authors must convince both peer reviewers and the editors of the scientific and technical merit of a paper; the standards of proof are higher when extraordinary or unexpected results are reported.
4) Because replication is required for scientific progress, papers submitted for publication must provide sufficient information to allow readers to perform similar experiments or calculations and use the reported results. Although not everything need be disclosed, a paper must contain new, useable, and fully described information. For example, a specimen's chemical composition need not be reported if the main purpose of a paper is to introduce a new measurement technique. Authors should expect to be challenged by reviewers if the results are not supported by adequate data and critical details.
5) Papers that describe ongoing work or announce the latest technical achievement, which are suitable for presentation at a professional conference, may not be appropriate for publication in "Electronics".

IX. Conclusion

A conclusion section is not required. Although a conclusion may review the main points of the paper, do not replicate the abstract as the conclusion. A conclusion might elaborate on the importance of the work or suggest applications and extensions.

Appendix

Appendixes, if needed, appear before the acknowledgment.

Acknowledgment

The preferred spelling of the word "acknowledgment" in American English is without an "e" after the "g." Use the singular heading even if you have many acknowledgments. Avoid expressions such as "One of us (S.B.A.) would like to thank ... ." Instead, write "F. A. Author thanks ... ." **Sponsor and financial support acknowledgments are placed in the unnumbered footnote on the first page, not here.**

References

[1] G. O. Young, "Synthetic structure of industrial plastics (Book style with paper title and editor)," in *Plastics*, 2nd ed. vol. 3, J. Peters, Ed. New York: McGraw-Hill, 1964, pp. 15–64.

[2] W.-K. Chen, *Linear Networks and Systems* (Book style). Belmont, CA: Wadsworth, 1993, pp. 123–135.

[3] H. Poor, *An Introduction to Signal Detection and Estimation*. New York: Springer-Verlag, 1985, ch. 4.

[4] B. Smith, "An approach to graphs of linear forms (Unpublished work style)," unpublished.

[5] E. H. Miller, "A note on reflector arrays (Periodical style—Accepted for publication)," *IEEE Trans. Antennas Propagat.*, to be published.

[6] J. Wang, "Fundamentals of erbium-doped fiber amplifiers arrays (Periodical style—Submitted for publication)," *IEEE J. Quantum Electron.*, submitted for publication.

[7] C. J. Kaufman, Rocky Mountain Research Lab., Boulder, CO, private communication, May 1995.

[8] Y. Yorozu, M. Hirano, K. Oka, and Y. Tagawa, "Electron spectroscopy studies on magneto-optical media and plastic substrate interfaces (Translation Journals style)," *IEEE Transl. J. Magn.Jpn.*, vol. 2, Aug. 1987, pp. 740–741 [*Dig. 9th Annu. Conf. Magnetics* Japan, 1982, p. 301].

[9] M. Young, *The Techincal Writers Handbook.* Mill Valley, CA: University Science, 1989.

[10] J. U. Duncombe, "Infrared navigation—Part I: An assessment of feasibility (Periodical style)," *IEEE Trans. Electron Devices*, vol. ED-11, pp. 34–39, Jan. 1959.

[11] S. Chen, B. Mulgrew, and P. M. Grant, "A clustering technique for digital communications channel equalization using radial basis function networks," *IEEE Trans. Neural Networks*, vol. 4, pp. 570–578, Jul. 1993.

[12] R. W. Lucky, "Automatic equalization for digital communication," *Bell Syst. Tech. J.*, vol. 44, no. 4, pp. 547–588, Apr. 1965.

[13] S. P. Bingulac, "On the compatibility of adaptive controllers (Published Conference Proceedings style)," in *Proc. 4th Annu. Allerton Conf. Circuits and Systems Theory*, New York, 1994, pp. 8–16.

[14] G. R. Faulhaber, "Design of service systems with priority reservation," in *Conf. Rec. 1995 IEEE Int. Conf. Communications,* pp. 3–8.

[15] W. D. Doyle, "Magnetization reversal in films with biaxial anisotropy," in *1987 Proc. INTERMAG Conf.*, pp. 2.2-1–2.2-6.

[16] G. W. Juette and L. E. Zeffanella, "Radio noise currents n short sections on bundle conductors (Presented Conference Paper style)," presented at the IEEE Summer power Meeting, Dallas, TX, Jun. 22–27, 1990, Paper 90 SM 690-0 PWRS.

[17] J. G. Kreifeldt, "An analysis of surface-detected EMG as an amplitude-modulated noise," presented at the 1989 Int. Conf. Medicine and Biological Engineering, Chicago, IL.

[18] J. Williams, "Narrow-band analyzer (Thesis or Dissertation style)," Ph.D. dissertation, Dept. Elect. Eng., Harvard Univ., Cambridge, MA, 1993.

[19] N. Kawasaki, "Parametric study of thermal and chemical nonequilibrium nozzle flow," M.S. thesis, Dept. Electron. Eng., Osaka Univ., Osaka, Japan, 1993.

[20] J. P. Wilkinson, "Nonlinear resonant circuit devices (Patent style)," U.S. Patent 3 624 12, July 16, 1990.

[21] IEEE Criteria for Class IE Electric Systems (Standards style), IEEE Standard 308, 1969.

[22] Letter Symbols for Quantities, ANSI Standard Y10.5-1968.

[23] R. E. Haskell and C. T. Case, "Transient signal propagation in lossless isotropic plasmas (Report style)," USAF Cambridge Res. Lab., Cambridge, MA Rep. ARCRL-66-234 (II), 1994, vol. 2.

[24] E. E. Reber, R. L. Michell, and C. J. Carter, "Oxygen absorption in the Earth's atmosphere," Aerospace Corp., Los Angeles, CA, Tech. Rep. TR-0200 (420-46)-3, Nov. 1988.

[25] (Handbook style) *Transmission Systems for Communications,* 3rd ed., Western Electric Co., Winston-Salem, NC, 1985, pp. 44–60.

[26] *Motorola Semiconductor Data Manual,* Motorola Semiconductor Products Inc., Phoenix, AZ, 1989.

[27] (Basic Book/Monograph Online Sources) J. K. Author. (year, month, day). *Title* (edition) [Type of medium]. Volume (issue). Available: http://www.(URL)

[28] J. Jones. (1991, May 10). Networks (2nd ed.) [Online]. Available: http://www.atm.com

[29] (Journal Online Sources style) K. Author. (year, month). Title. *Journal* [Type of medium]. Volume(issue), paging if given. Available: http://www.(URL)

[30] R. J. Vidmar. (1992, August). On the use of atmospheric plasmas as electromagnetic reflectors. *IEEE Trans. Plasma Sci.* [Online]. *21(3).* pp. 876–880. Available: http://www.halcyon.com/pub/journals/21ps03-vidmar

Information for Authors

Editorial objectives

In the journal ”Electronics”, the scientific papers from different fields of electronics and electrical engineering in the broadest sense are published. Main topics are electronics, automatics, telecommunications, computer techniques, power engineering, nuclear and medical electronics, analysis and synthesis of electronic circuits and systems, new technologies and materials in electronics etc. The main emphasis of papers should be on methods and new techniques, or the application of existing techniques in a novel way.

The reviewing process

Each manuscript submitted is subjected to the following review procedures:

- It is reviewed by the editor for general suitability for this publication;
- If it is judged suitable, two reviewers are selected and a double-blind review process takes place;
- Based on the recommendations of the reviewers, the editor then decides whether the particular paper should be accepted as it is, revised or rejected.

Submissions Process

The manuscripts are to be submitted using the Electronics Journal online submission system – accessible from Journal’s homepage.

Manuscripts have to be prepared in accordance with the instructions given in the template for paper preparation that can be found on the journal’s web page (www.els-journal.etf.unibl.org).

Authors should note that proofs are not supplied prior to publication and ensure that the paper submitted is complete and in its final form.

Copyright

Articles submitted to the journal should be original contributions and should not be under consideration for any other publication at the same time. Authors submitting articles for publication warrant that the work is not an infringement of any existing copyright and will indemnify the publisher against any breach of such warranty. For ease of dissemination and to ensure proper policing of use, papers and contributions become the legal copyright of the publisher unless otherwise agreed.

ELECTRONICS, VOL. 24, NO. 1, JUNE 2020

ISSN 1450-5843
UDK 621.38